UNIVERSITY OF CALIFORNIA,
IRVINE

Investigations of Micropyramid Design and Materials for Thermal Radiation Control

submitted in partial satisfaction of the qualifying examination
for the degree of

DOCTOR OF PHILOSOPHY

in Mechanical and Aerospace Engineering

by

Jonathan Sullivan

Dissertation Committee:
Professor Jaeho Lee, Chair
Professor Ordal Boyraz
Professor Ramin Bostanabad

2023

Dedication

To Staff Sergeant Erik W. Jacobson
The brother who always believed in me –
May your belief in me and others
Live on in these words

Table of Contents

List of Figures

List of Tables

Acknowledgements

I would like to sincerely thank my Ph.D advisor – and my committee chair – Professor Jaeho Lee. What started with an email after an undergraduate class offering an undergraduate opportunity to do research has led to years of learning, growth, and experiences I could have only dreamed of prior. I am the researcher, learner, presenter, and professional I am today because of his guidance and belief in me. I am thankful to Professor Ozdal Boyraz for his guidance, feedback, and support through our multiple collaborations over the years. I am grateful to Professor Ramin Bostanabad for not only being part of the defense committee, but the recommendations and guidance given that have led to my machine learning work to be where it is today. I also would like to thank Professor Manuel-Gamero Castano and Professor Camilo Velez Cuervo for their participation in my qualifying exam committee and the high-quality comments, feedback, and guidance I received through the process from them. I would like to also thank Professor Yun Wang for his feedback as a part of my master's thesis and his leadership throughout my undergraduate project experience.

I cannot express how thankful I am to all my colleagues, mentors, and leaders at NASA JPL, GRC, and other facilities. First and foremost, I would like to thank the US Government and NASA as an institution as NASA's fellowship support has helped make my dreams a reality and my research achievable. I will never forget my summer internship under the guidance of David Neff, and subsequent years under Fivos Drymiotis. The joy and passion that both men exude is an inspiration, and I will be forever grateful for those years at JPL. I would like to also extend my thanks to Dr. Sabah Bux and Dr. Jean-Pierre Fluerial for their project leadership and support at JPL. I also cannot thank enough Dr. Arman Mirhashemi, my technical advisor for the NASA fellowship at NASA GRC. Your experience, supervision, feedback, and leadership were indispensable in my journey, and I will miss our monthly catchups. I also am sincerely grateful for the GRC-LTE leadership including Dr. Vikram Shyam, Erza McNichols, and Mark Celestina. I would also like to thank Paht Juangphanich, Brooke Weborg, and Daniel Sutliffe for their technical feedback and recommendations. I am also grateful for the many other friends I met along the way, but one person in particular – Kai Chapman – reminded me why I love engineering so much and how much fun it can be to help others learn.

To the lab mates I started with as an undergrad and had the pleasure of working with over the last 5 to 7 years – Ziqi Yu, Laia Ferrer, Shiva Farzinazar, Xiao Nie, Zongqing Ren, Quang Fam, Kimia Montazeri, Youngjun Suh – I thank you for all the hours gifted to helping me, the advice you have given, the meals we have shared, and the times we have shared together. I wish nothing but the best for every single one of you and I know that my experience wouldn't have been as fulfilling as it was without you guys being there along the way. To those who will be continuing the work – Paul, Charles, Jungyun, Jiajian, Jiahui – I wish you all the best and look forward to seeing where you go. I would also like to extend a special thanks to Wahid and Alberto Escobar – both the definition of excellent collaborators.

To my friends who have been with me over the years, I will be forever grateful for your companionship. Sean and Daniel need to know nothing other than how much I appreciate them – I'm sure they know the rest. To Adam, John, and many others, I thank you

for your companionship and all the times we have spent together. Without it I don't know where I would be.

Finally, and certainly not least – I cannot express how much I am thankful for my family. To my mom, dad, brothers, sisters, and far too many others to list – you have been there for me my entire life, you have always supported me, and I am the person I am today because of all of you. One person in particular who will not be able to read this note, my brother, Erik, was taken too soon by a disease which too many forget. I will never forget his belief in me, and I am grateful to know that he no longer is burdened with the pain he struggled with. Finally, to my wife – Tania – know that I will forever love you. You have been my rock in unsteady waters, my guide in the dark, and the one that keeps me whole. To your belief in me, to your never-ending love for me, and to your unquenchable support, I will be forever and eternally thankful and I would be lost with you.

Vita

Education

Ph.D., Mechanical & Aerospace Engineering 2023
University of California Irvine, Irvine, CA
Advisor: Professor Jaeho Lee

M.S, Mechanical and Aerospace Engineering 2020
University of California Irvine, Irvine, CA

B.S, Aerospace Engineering, B.S Mechanical Engineering 2017
University of California Irvine, Irvine, CA

Research Experience

Graduate Research Appointment, HIER Lab
2017 - Present
University of California, Irvine – Advisor: Professor Jaeho Lee

- Lead the design and implementation of surrogate and reverse machine learning models to replace optical simulations for use in large scale thermal radiation control optimization
- Designed supervised machine learning models using Deep Learning (DL) methods including Deep Neural Networks (DNNs), Convolutional Neural Networks (CNNs), and Recurrent Neural Networks (RNNs)
- Performed extensive studies of the optical properties of micro/nanotextures (e.g., surface relief gratings, microsphere polymer composites, phase-change coatings, and nanotextured silicon) using Finite-Difference Time-Domain (FDTD) and Rigorous Coupled Wave Analysis (RCWA)
- Fabricated and characterized optical and thermal properties of micro and nanotextured silicon wafers, and fabricated nano/microtextured wafers with metal/phase change material coatings
- Highly experienced in thermal modelling for nano to macroscale systems using COMSOL, ANSYS, and analytical modelling approaches

Gradate Research Fellow 2019 – 2022
NASA Glenn Research Center

- Lead the development of an aggregate neural network package to optimize thermal/optical properties in a multi-functional heat exchanger
- Developed novel surrogate machine learning models that are not bound by material classification, capable of extrapolating solutions for a material input

Graduate Intern, Graduate Student Employee
2018 – 2020
NASA/Cal-Tech Jet Propulsion Laboratory (Sections 3462, 3464)

- Successfully built and operated a 3ω-method experimental thermal measurement setup for

novel thermoelectric material measurement
- Developed, modelled, simulated, and optimized a high-temperature Harman-method measurement apparatus for high temperature (~ 1200 K) thermoelectric sample characterization using ANSYS and Solidworks

Undergraduate Research Assistant 2016 - 2017

University of California, Irvine – Advisor: Professor Jaeho Lee

- Completed nanowire measurement sensitivity analysis using steady-state and transient response thermal models in ANSYS and COMSOL
- Ran 3ω measurements to characterize the thermal properties of thin-film samples and assisted in the implementation and running of nanowire thermal metrology utilizing a 5-probe nanobridge method

Awards and Honors

NASA Graduate Fellow (NASA Glenn Research Center) 2019

- 3-year Ph.D. funding, one of 19 fellowships awarded in 2019

NSF Honorable Mention (GRFP) 2019

Peer-Reviewed Journal Publications

- **Sullivan, J.**, Mirhashemi, A. & Lee, J. Deep learning-based analysis of microstructured materials for thermal radiation control. *Sci Rep* 12**,** 9785 (2022). doi: 10.1038/s41598-022-13832-8
- **Sullivan, J.**, Yu, Z. & Lee, J. Nanometer-Thick Nickel Coatings on Silicon Micropyramids for Infrared Absorption. *ACS Appl. Nano Mater.* 5, 4**,** 4615-4622 (2022). doi: 10.1021/acsanm.2c00541
- **Sullivan, J.,** Yu, Z. & Lee, J. Optical Analysis and Optimization of Micropyramid Texture for Thermal Radiation Control. *Nanoscale and Microscale Thermophysical Engineering,* 137-152 (2021). doi: 10.1080/15567265.2021.1958960
- Khan, M., **Sullivan, J**. Lee, J. & Boyraz, O. High Sensitivity Long-Wave Infrared Detector Design Based on Integrated Plasmonic Absorber and VO2 Nanobeam. *IEE Journal of Quantum Electronics*, 57, 4. 1- 11 (2021). doi: 10.1109/JQE.2021.3080287.
- Escobar, E., Zanganeh, S. **Sullivan, J**. Li, L., Dautta, M., Lee, J & Tseng, P. Fluidic Inflitrative Assembly of 3D Hydrogel and Heterogenous Composition and Function. *Advanced Functional Materials*, 31, 33 (2021). doi: 10.1002/adfm.202103288
- Nie, X., Yoo, Y., Hewakkuruppu, H., **Sullivan, J.** Krishna, A. & Lee, J. Cool White Polymer Coatings based on Glass Bubbles for Buildings. Sci Rep 10, 6661 (2020). doi: 10.1038/s41598-020-63027-2

Conference Publications

- **Sullivan, J**., Krishna, A & Lee, J. "Porous Nickel as a Selective Emitter for Surface Cooling in Various environments". IEEE iTherm Conference Paper (2018)
- **Sullivan, J.**, Argemi, L., Yu, Z. & Lee, J. "Wafer-Scale Hierarchically Textured Silicon for

Surface Cooling**",** IEEE iTherm Conference Paper (2019)

- Argemi, L. **Sullivan, J.** & Lee, J. "Effects of Silicide Inclusion Shape on Thermal Transport of Silicon-based Nanowires and Nanocomposites for Thermoelectric Applications". IEEE iTherm Conference Paper (2019)
- Khan, W., Sadri-Moshkenani, P., Islam M., Boyraz O., **Sullivan, J**., Yu, Z. & Lee, J. Selective and Efficient Infrared Detection by Plasmonically Heated vanadium dioxide nanowire. SPIE Nanoscience + Engineering, (2020).

Technical Skills

- **Material Characterization:** UV-Vis/FTIR spectroscopy, IR thermography, XRD, 3ω method, SEM, EDS, XPS, 4 probe resistance measurements, electrical thermometry, Harman method
- **Material Synthesis:** Wet and dry etching, e-beam evaporator, e-beam deposition, polymer composite fabrication, RF sputtering
- **Design/Analysis:** FDTD, ANSYS, RCWA, COMSOL, Solidworks (*certification: C-G42NX657UY*), AutoCAD, EAGLE, Fluent, Microsoft Suite
- **Coding Languages:** MATLAB, Python

Leadership, Involvement, and Volunteer Experience

Volunteer Tutor 2020 - 2021

MyThirdPlace – Math and English Tutor

- Tutored multiple underprivileged students in high school/middle school level geometry, algebra, and writing/English

Physics and Math – Personal Tutor 2014 – Current

- Instructed middle-school, high-school, and college students on topics including engineering course work, algebra/calculus, physics, chemistry, English/writing, and others.

Student Mentor and Peer-advisor, Engineers Mentoring the Future 2015 – 2017

- Mentored underclass men and provided teaching

Engineering Student Council 2013 – 2017

- Instrumental in the planning and the implementation of the "Engitech" Career Fairs in 2015, 2016, which involved 40-50 corporate vendors, performed role as a photographer

Volunteer, "FEMINEERS"

2016 - 2017

- Volunteered at an elementary school's program designed to inspire young girls to engage in STEM and Engineering

Professional Memberships

- Pi Tau Sigma (Mechanical Engineering Honors Society)
- Sigma Gamma Tau (Aerospace Engineering Honors Society)
- Tau Beta Pi (Engineering Honors Society)

References

Jaeho Lee, Assistant Professor
Department of Mechanical and Aerospace Engineering
University of California, Irvine

Arman Mirhashemi, Research Aerospace Engineer
NASA Glenn Research Center (GRC)
Cleveland, OH

Fivos Drymiotis, Senior Technologist (3462)
NASA Jet Propulsion Laboratory (JPL)
Pasadena, California

Abstract of the Dissertation

Investigations of Micropyramid Design and Materials for Thermal Radiation Control

By

Jonathan Sullivan

Doctor of Philosophy in Mechanical and Aerospace Engineering

University of California, Irvine 2023

Professor Jaeho Lee, Chair

The ability to engineer how light interacts with a surface is at the core of the development of materials that can passively and selectively control thermal radiation for thermal management solutions. Recent years have seen significant developments in the design of microstructured materials and metamaterial surfaces that are engineered to control matter-light interactions. This doctoral research focuses on the design and optimization of one such microstructure – micropyramids – and how micropyramids can be designed, optimized, and implemented to control thermal radiation using both advanced computational and experimental approaches.

Micropyramid texturing consists of nanometer to micrometer scale pyramids with a symmetric base and can be used to modulate the optical and thermal properties of a surface. Micropyramids control optical properties by introducing localized electromagnetic confinement and geometric scattering that reduces a surface's reflectivity. These mechanisms can be leveraged by controlling the micropyramids' key geometric parameters and constituent material(s) – and if properly engineered – can induce and optimize anti-

reflective behavior at desired broadband wavelength spectrums. While the general anti-reflective properties of micropyramids and other similar surface-relief grating structures are well studied in the field of optics, much less is known about the application of micropyramids to broadband thermal management. To investigate micropyramids for thermal management, an optimization engine derived from cost-function driven thermal analysis and the finite-difference time domain (FDTD) optical solver was developed. Using this process, several common engineering materials – such as Nickel (Ni) and Alumina – were studied and analyzed for tunable optical properties by combining them with micropyramid structures. From the analysis, the key geometric and material parameters that link to thermal-optical properties were identified.

A key limitation to the cost-function driven analysis, however, is that the FDTD solver is slow and computationally expensive. To address this, a neural network method derived from deep learning was developed to act as a "surrogate" optical solver. The surrogate network can perform simulations at a rate 6 to 8 orders of magnitude faster than the FDTD simulations it was trained on, allowing for large-scale thermal optimizations of properties that would be impossible using traditional simulation methods. The network's novel design allows for discrete material inputs, and demonstrates an exceptionally high degree of accuracy in extrapolating the optical properties of materials that the model has not been trained on. The surrogate method is further refined and improved using machine-vision and image-based methods, paving the path towards neural network derived models that can predict the optical properties of complex geometries and multi-material systems without computationally expensive simulations.

While the cost-function method for thermal optimization is effective and is greatly accelerated using the surrogate neural network, it is limited in its ability to perform inverse design. Finding optical spectrums to match thermal conditions using the surrogate method requires “brute-force” optimization methods, which limits the optimization speed and scope. To rectify this, a neural network architecture was developed that inverts the problem and directly provides geometric and material solutions that best fit a desired input spectrum. This process occurs nearly instantaneously and facilitates the optimization and design of micropyramids for broadband and narrow-band applications. The inverse neural network was combined with the surrogate network and post-processing/simulation methods to form a self-learning loop that improves thermal and optical prediction accuracy as more inputs are processed. Furthermore, we utilize the network construction to develop a material search algorithm that can both search through existing materials and identify new materials that best solve for a desired input spectrum. From the analysis of micropyramids and deep-learning process, a material and geometry that improves broadband infrared (IR) thermal emission is identified and subsequently fabricated. By combining nanometer (nm)thick coatings of metal with micro and nanotextured silicon, specific control of broadband optical properties is demonstrated that would be impossible to achieve with either material on its own. While the average infrared absorptivity of untextured silicon with 20 nm of Ni is 0.11, it is shown that micro and nanotexturing can increase the average infrared absorption when combined with a 20 nm thick Ni coating to 0.46 and 0.66 respectively. The findings in this thesis will guide the design of future surrogate neural networks for microstructure design and for the optimization of micropyramids for thermal radiation control.

Chapter 1 - Introduction

1.1 Overview of Spectral Radiation

Electromagnetic (EM) radiation is the transmission of energy via the waves of an electromagnetic field that propagates through space regardless of medium[1]. The energy of the electromagnetic wave depends upon the oscillation frequency of the wave; this relation can be described by Planck's equation $E = hf$, where the energy of the wave is proportional to the frequency and Planck's constant (h). This relation can also be visualized in the form of wavelength—where wavelength is related to frequency by the speed of light, $\lambda = c/f$— as the wavelength decreases, the energy of the wave increases. This creates an electromagnetic spectrum that ranges from highly energic waves such as Gamma-rays and X-rays (< 1 pm and 10 pm – 10 nm respectively) to radio waves (cm and beyond).

As governed by Planck's law of radiation, a black body in thermal equilibrium will radiate a spectral distribution of energy dependent upon both the surface temperature and spectral properties of the surface[2]. Thermal radiation – the transfer of heat via radiation – from a surface or body can be described as a function of its Planck distribution.

$$E_{\lambda,b} = \pi I_{\lambda,b} = \frac{2hc_0^2\pi}{\lambda^5\left(\exp\left(\frac{hc_0}{\lambda kT}\right)-1\right)} \qquad \text{Eq. 1.1}$$

The sun, with a surface temperature near 5800 K, has a spectral distribution that occurs in the visible (λ = 400 – 800 nm) and near-infrared (λ = 800 – 2500 nm) regions of the EM spectrum. Most terrestrial bodies at ambient temperature (near 300 K) have a spectral distribution that is in the mid-infrared (λpeak = ~ 9.5 um). As emission and absorption usually occur at different wavelength bands, spectrally dependent emission/absorption properties are very important to the thermal response of a material.

The spectral properties of a material – and how that material will respond to electromagnetic radiation at a given wavelength – are dependent upon a host of factors but is primarily controlled by the material's refractive index. Refractive index can be simply thought of as the ratio of the speed of light to the speed of light in the material, $n = \frac{c}{v}$. The complex refractive index, $\bar{n} = n + ik$ accounts for the dispersion and attenuation of the electric field in the material by adding an imaginary coefficient k, otherwise referred to as the extinction coefficient of a material. Whereas classically electrically conductive materials such as metals are generally reflective due to high values for both the extinction coefficient and refractive index, dielectric materials are transmissive due to a characteristically low extinction coefficient. On a fundamental level, the refractive index describes the microscopic interaction of the electromagnetic oscillation with the atoms of the material and the charge disturbance generated in the atomic structure[3]. As electromagnetic radiation is a wave phenomenon, however, geometric parameters and surface topology can induce localized resonances, confinement, and near-field effects that, in conjunction with refractive index, can control how electromagnetic radiation interacts with a material.

1.2 Radiative Heating and Cooling

Combining the tunable spectral properties of a material with temperature dependent emission enables the design of materials that can selectively control emission and/or absorption of thermal radiation. Radiative heating and radiative cooling are passive thermal management techniques that depend on radiative heat transfer to either heat or cool the surface respectively. In the case of radiative heating, the intent is for the surface to absorb the entirety of incident radiation while minimizing energy lost to IR emission. For radiative cooling, the intent is to provide a surface that rejects incident radiation while maximizing

surface emission; this process can even yield surfaces that are able to cool beneath the ambient temperature.

Harnessing solar irradiation to generate energy directly via a photovoltaic conversion is a very well-known and established process[4], but the thermal energy in solar irradiation can also be efficiently used to generate electricity or as a thermal energy source. An example of this is a solar thermal collector (Figure 1-1), in which solar irradiation is concentrated onto an absorbing surface and heating a fluid that runs through it [5], [6]. The solar radiation is thus converted into a form useable either by a thermal process or usable as a heat source for a Rankine cycle to produce electricity[6].

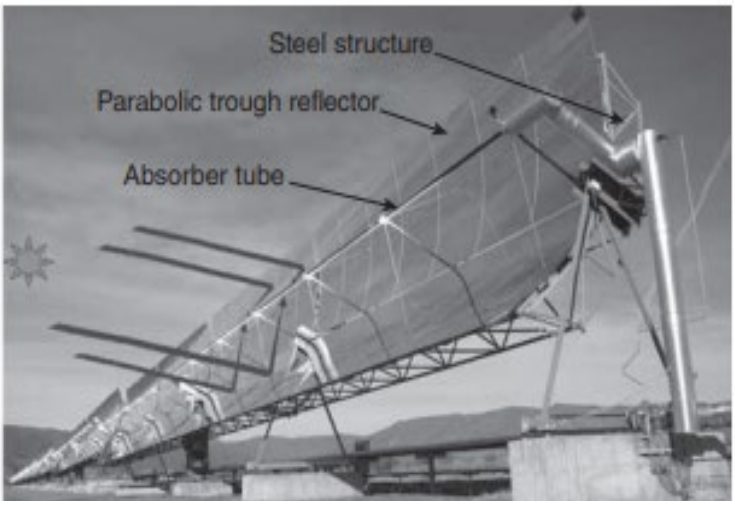

Figure 1-1. Example of a Parabolic Solar Thermal collector [5]

Thermophotovoltaic (TPV) and Solar Thermionic devices are other methods that can be used to convert absorbed thermal energy into electricity. TPVs generate electricity in the same way as a photovoltaic (PV) device does– photons of radiation are absorbed and a p/n junction generates an excess electrical charge [7], [8]. The key difference, however, is that while PVs absorb incident solar radiation from the sun (a 5800 K blackbody emitter at a

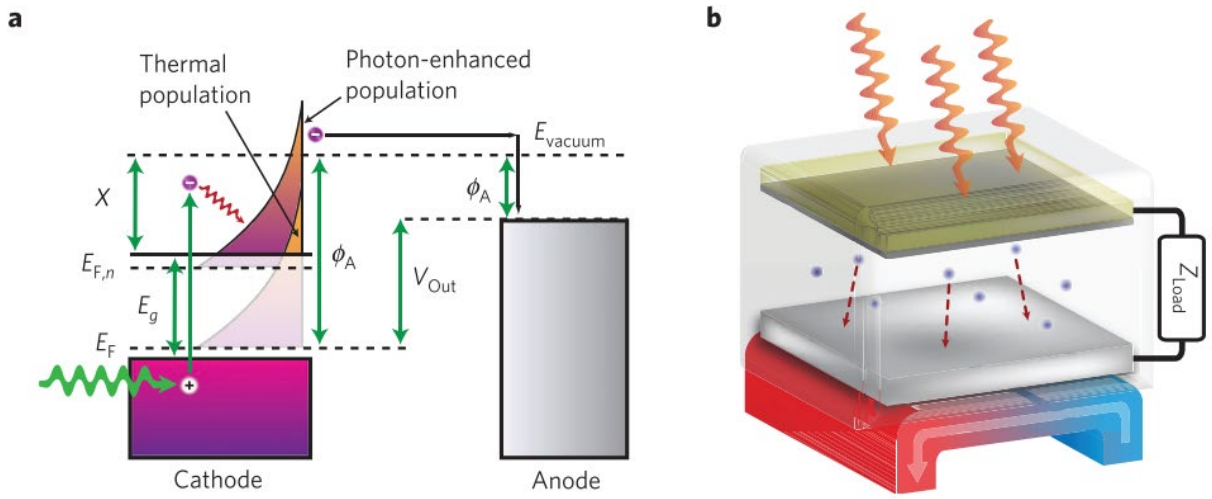

Figure 1-2. (a) Diagram of PETE process in [9]. The device can harvest both photon and heat energy as a result of photoexcitation. (b) An example of the PETE process in practice. Unused heat energy drives a thermal engine

distance of ~ 1.5e8 km) a TPV receives radiation from a surface at a temperature of 1300 – 1800 K at a separation distance of several centimeters. While the power emitted by a body varies by the fourth power of the temperature (Eq. 1.1), the inverse square law dependence of radiation dominates due to the disparity in distance. This corresponds to an unconcentrated PV system receiving radiation on the order of 0.1 W/cm^2 while a TPV receives up to 5 – 30 W/cm^2. Thus, in an ideal case of perfect emission and absorption, the power density of a TPV can greatly exceed that of a PV.

While radiative energy generation devices depend on the absorption and retention of thermal energy, passive cooling radiators are designed to limit absorbed energy while maximizing thermal energy loss via emission. Specifically, radiative cooling relies on the use of the atmospheric transmission window to emit radiation from the surface into the heat sink of space (~ 3 K). The atmospheric transmission window is a "window" of near unity transmission in the atmosphere from the EM wavelength range of 8 to 14 microns that allows

for thermal radiation to be emitted from any terrestrial surface to space through the atmosphere with nearly zero atmospheric impedance [9]. This window corresponds directly to the Planck distribution for a blackbody ~ 300 K. Thus, to properly utilize the overlap between the peak of thermal emission occurring near ~10 microns and the atmospheric window (Fig 3), a surface emissivity should be as close to unity as feasible between 8 to 14 microns for optimal radiative cooling. Simultaneously, the surface must not absorb incident radiation as that will negate any values for cooling achieved by emission in the MIR/IR. This impresses the need for selective emitter designs, as simply utilizing a highly emissive surface will lead to heating when exposed to solar irradiation. Assuming that the surface does not absorb solar radiation, surface emission can lead to significant sub-ambient cooling (~ 7 – 10 °C) [10], [11]. Interestingly, this process dates back to at least 400 BCE, where Persians formed structures that leveraged the sky window during the cool season to form ice in the desert [12]. In more recent years, the concept of radiative cooling has been applied to reducing building energy costs via surface building coatings, wearable technology for personal cooling, and many other applications.

1.3 Absorbing Materials for Radiative Heating Systems

The fundamental element in either a radiative cooling or heating system is in the design of the absorbing or emitting surface. In the case of "radiative heating" systems such as TPVs or solar thermal collectors, an essential component to maximizing efficiency is utilizing an absorbing material that achieves a near-unity spectral emissivity profile throughout the solar spectrum. In the ideal case, the surface would retain all incident radiation without reflecting any incident radiation or emitting any energy from itself. For TPVs, it is also important that the spectral absorption be maximal for a blackbody

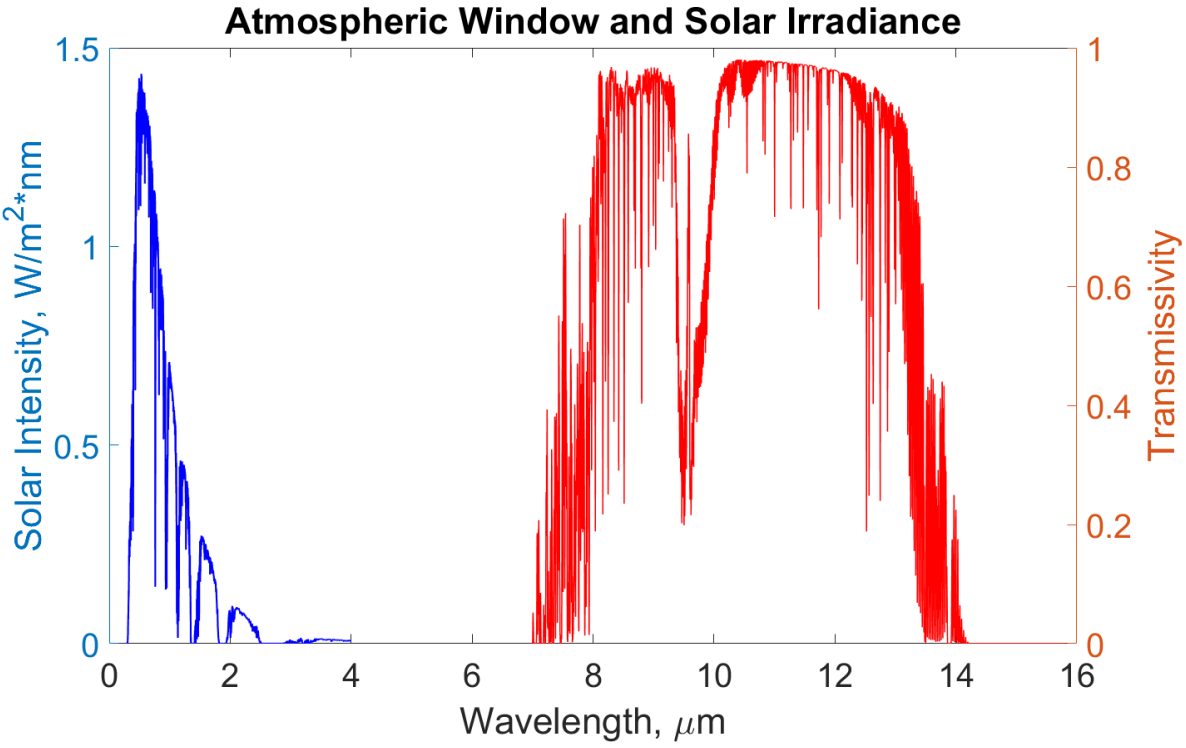

Figure 1-3. Atmospheric Transmission Window (red) and Solar Irradiance Spectrum (blue). The solar irradiance spectrum plotted is AM1.5, which accounts for irradiance after passing through an "airmass" value of 1.5; this is considered to be the nominal solar distribution for most locations on earth. When integrated it correlates to nearly ~ 1000 – 1100 W/m^2 [214]. The atmospheric transmission window occurs between 8 and 14 microns and allows radiation to pass freely through the atmosphere.

distribution matching a nominal TPV temperature between 900 and 1800 °C[7]. Simultaneously, the materials involved must be able to endure high-temperature conditions. Some simple, but limited methods, to enhance surface absorption include using triangularly corrugated surface gratings [13] and multilayer stacked structure of oxide/metal nanofilms [14]. These methods rely on geometric optics and refractive index control via multiple materials respectively. While effective in narrow wavelength bands, these methods are limited in their application to broadband optical and thermal control.

A more advanced approach to induce elective absorption/emission behavior is via engineered nano and microtextured topology. Nano and microengineered devices, such as nanodomes (Figure 1-4) [15] constructed of hydrogenated amorphous silicon that can absorb ~ 94% of light between the wavelengths of 400–800 nm. This is contrasted to a 65% absorption observed in flat and untextured devices for the same wavelength region. Similarly, the "core-shell concept" can be applied to surface topology to selectively modify the absorption/emission properties of the surface. By combining a metallic "core" with a dielectric "shell", the electric field can be selectively attenuated based on the combination of the refractive index mismatch and the structural geometry. Significant absorption enhancements have been demonstrated using a core-shell design with microstructures made of Ag/SiO_2 [20] and Ni/Al_2O_3 [16]. Metallic grating structures can also be used to selectively control the optical band absorption properties of a surface [17].

1.4 Radiative Cooling Materials

For radiative cooling structures, the surface must be designed such that spectral emissivity is maximal in the thermal emission spectrum while absorptivity in the solar spectrum is kept to a minimum. The thermal emission spectrum is a function of the temperature of the surface, normally peaking in the near-infrared and mid-infrared (NIR/MIR) wavelength regions. The ideal radiative cooler for a body near ~ 300 K has a UV/Vis/NIR absorptivity of zero and emissivity at unity in the mid-IR. Structures in literature that demonstrate high levels of spectrally engineered radiative cooling performance include similar concepts as the research into solar absorbing materials, but the materials used to create the surface differ due to the necessity of both limiting the solar absorption and

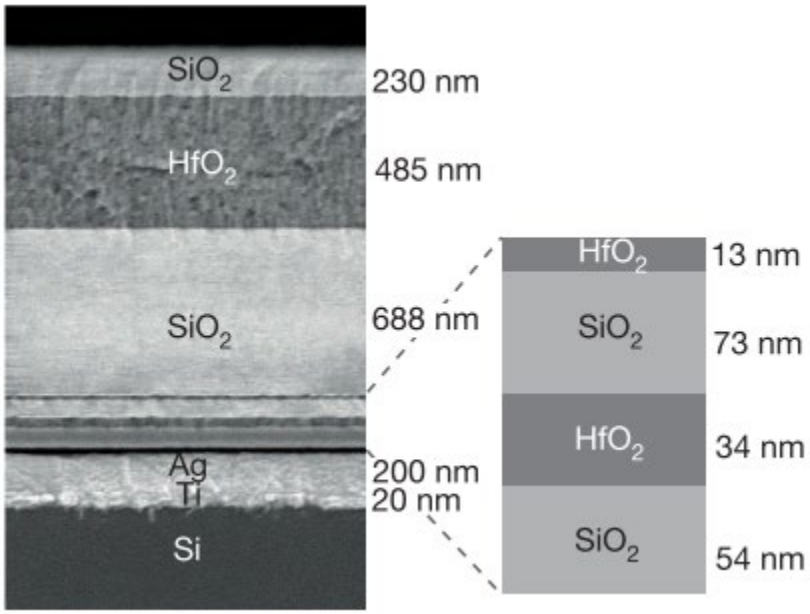

Figure 1-4 SEM cross-section of structure demonstrated by [22]. Numerical optimization defined the combination of layer thickness and material selection

maximining the thermal emission. A notable example of the similarity between radiative heating and cooling designs is in the multilayer stack demonstrated by Raman, et. al [18].

The gradient of refractive indices allows for the emission of MIR/IR radiation by employing ceramic materials (SiO2, HfO2) that emit strongly in this wavelength band, and the rejection of solar radiation by the reflective Ti/Ag layers at the bottom of the multilayer stack. As opposed to a metallic tandem absorber [15], the oxide layers are transmissive to visible light and thus absorption of solar irradiation is kept to a minimum.

Polymers are also a well-studied material for radiative cooling applications. This is due to polymers such as Polydimethylsiloxane (PDMS) being nearly completely transmissive in the visible and nearly perfectly emissive in the MIR/IR as a function of their hydrocarbon chemistry. Recent studies have focused on providing methods to enhance the native absorption while reflecting the incident solar radiation after it is transmitted through the polymer layer. Two such methods include providing a combination of SiO2 (glass) beads in the polymer matrix with a reflective back layer [19] and introducing a high volume fraction

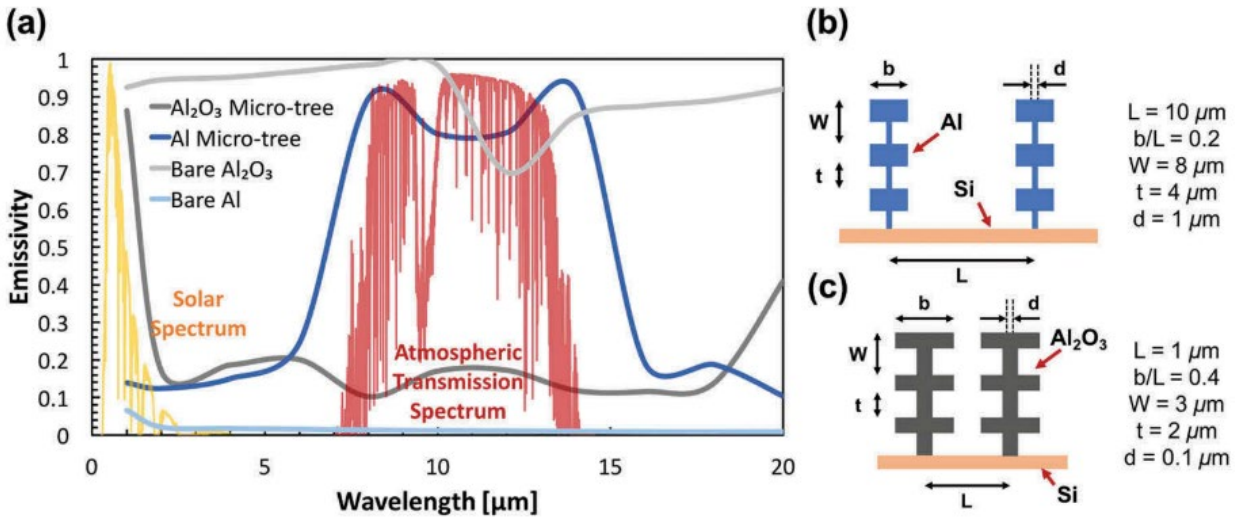

Figure 1-5 (a) Alumina (ceramic) bio-inspired micro-tree design compared with bare Alumina, and bare Aluminum from [25]. (b,c) are the dimensions and designs utilized for the tree-designs

of hierarchical hollow glass bubbles into the polymer [20]. Introducing a micro/nanoscale

pattern into ceramic materials can also provide an engineered spectral response in the IR. An example of this are nanostructured ceramic "trees" inspired by the morpho butterfly's structural coloration as demonstrated by Krishna, et. al. [21].

1.5 Micropyramidal Topology for Spectral Radiative Control

While the previous structures for spectral control have yielded excellent results, a proven way to control thermal radiation is exploit the anti-reflective behavior of periodic surface topology. Many topologies can provide spectral control based on geometric parameters, but pyramidal surface structures are selected as the key point of study for this work due to the extensive tunability of the spectral properties as a function of geometry, as well as pragmatic concerns such as the ease and scalability of manufacture and the array of materials that can be patterned with a pyramidal design. Pyramidal topology is a form of micro/nanoscale texturing that has been studied extensively for optical metamaterials[26, 27]. In previous literature, the anti-reflective properties of pyramidal texturing have been studied primarily as a means of enhancing solar absorption. A notable example of its usage is in the fabrication of pyramidally derived "black silicon" [24], [25]. Liu, et. al.[25] reduced the reflectivity (from 300 to 1200 nm) of untextured silicon from an average weighted value of 34.8% to 11.2% by introducing a microtextured pattern, leading to a more optically black appearance. Li, et. al [16] demonstrated that the anti-reflective behavior of the pyramids can be used to enhance the spectral absorption properties of nickel nanopyramids. To further optimize their results, they employed a core-shell approach, utilizing a thin ceramic layer (Al_2O_3) to further enhance the absorption profile. Based on this work, Peng, et. al.[26] developed nickel pyramidal layers that were deposited on polystyrene films to serve both as an absorption enhancement mechanism and protective layer for solar cells. While these

results demonstrate the anti-reflective properties of optical absorbing materials, they are limited by the experimental constraints employed by their process and the fixed relations between the two geometric parameters of the pyramids. Further, little attention has been paid to non-visible/NIR absorbing materials and the impact of geometry on the thermal transport in the IR for cooling applications.

1.6 Outline of Research

This thesis develops and expands the understanding of thermal management and optical property optimization using primarily micropyramid surface structures. Chapters 2 focuses on the fundamentals of micropyramids and connecting key geometric/material parameters to the optical and thermal response. Simple optimization techniques combined with finite-difference time-domain (FDTD) simulations highlight the potential to optimize a micropyramid for a set of thermal design criteria. In Chapter 3, a surrogate neural network method based on deep learning is shown that can effectively emulate the outputs of FDTD, dramatically expanding the scope of optimization and allowing for a comprehensive material search algorithm to be developed. In Chapter 4, a complementary surrogate neural network based on image-processing is presented that exceeds the performance of the previous model. Chapter 5 explores the use of the neural network methods presented in chapter 3 and 4 in generating an inverse neural network, enabling rapid optimization of structures and materials for a desired optical spectrum. Chapter 6 focuses on experimental validation of the optical performance of textured micropyramids and highlights how additional materials and geometric complexity expand the tunability of optical design. Finally, Chapter 7 offers perspectives on the expansion of the techniques shown and future opportunities for research in optical/thermal microstructures.

Chapter 2 : Optical and Thermal Analysis of Micropyramids

2.1 Introduction to Micropyramids

An approach that has proven to be effective in engineering surface optical properties is patterning a microscale pyramid-like ("micropyramid") surface texture into a material. The influence of periodic pyramidal design is well-established in the field of optics as it is known to induce anti-reflective properties at the surface as a result of light confinement by the texturing[23], [27]. One of the most common applications of micropyramid texturing is in the design of “Black Silicon” – silicon that appears black due to a significant reduction in the optical reflectivity due to micropryamid structuring[24]. Micropyramid and nanopyramid patterned silicon designs have been widely adopted for solar cell applications as the pattern leads to enhanced photon absorption in the visible (VIS) and near-infrared (NIR) wavelengths[25], [27]–[30]. The design can be further enhanced with the inclusion of nanoscale hierarchy – either in the form of silicon nanopillars/wire architecture[31]–[33] or hybrid-material nanowires[34], [35]. Silicon micropyramids can also be coated with another material—adding an additional element of control over light interaction with the surface[36]. Micropyramid geometries have also been utilized to significantly enhance the solar absorptivity of metals. Micropyramids made of nickel have received attention for solar applications due to nickel’s favorable mechanical/optical properties, with previous studies utilizing core-shell nanoscale nickel pyramids for TPV/Solar applications[16] or as a protective layer in solar panels[26]. Tungsten (W) Pyramidal grating structures have also been explored for high-temperature absorption applications: with the geometry enhancing the metal’s solar absorption coefficient to 0.92[37]. The anti-reflective properties of micropyramid texturing has also been demonstrated to enhance the absorption

characteristics of dielectric[23] and polymer[38] materials. Pyramidal surface features have broad appeal as they are both easily manufacturable and scalable[16] and can be patterned into a wide variety of materials via the template stripping technique[39], [40]. Further, pyramidal topology has demonstrated self-cleaning and hydrophobic properties[25], making it attractive for many applications.

For thermal radiation control applications, there are two spectral regions of interest for any surface: VIS/NIR and mid-infrared (MIR). The former is the most important optical parameter for solar applications as the spectral absorption from $\lambda = 300 - 2500$ nm determines the quantity of solar energy absorbed by the surface. While silicon micropyramids enhance absorption of visible light, beyond $\lambda = 1000$ nm the drop in extinction coefficient and rise in transmission in Si[41], [42] leads to a decay in the pattern's absorption enhancement. As a result, the optical properties of Si micropyramids and nanostructuring have been studied extensively between $\lambda = 400 - 1100$ nm[25], [28]–[32]. Use of coatings and fabricating micropyramids in other materials extends the region of efficacy and can also influence the NIR/MIR emissivity[16], [37], a key parameter in the determination of thermal emission from a surface. Micropyramids have been shown to enhance absorption in SiN between $\lambda = 1 - 2.5$ μm[43], inverse-Si micropyramids coated with Pt can increase emission between $\lambda = 1.4 - 5$ μm[44], and advanced processing can result in enhanced absorption through the MIR[45]. Already MIR emissive materials – such as polymers[38] and SiO_2/HfO_2[46] – can have near perfect emission in the infrared when patterned with micropyramids.

Control over the spectral absorption and emission properties of a material can yield unique thermal solutions. Beyond micropyramids, other surface topologies such as nano-

domes[15], corrugated surfaces[13], and core-shell structures[47], and gratings[17] have been proposed for high-efficiency solar absorption. By enhancing the spectral emissivity in the infrared region, surfaces

can leverage the sky-transparency window to emit radiation to space and cool beneath ambient temperatures[48]. Referred to as "passive radiative cooling", solutions range from corrugated graphene/nickel structures[49], [50], to multilayer stacks[18], and engineered

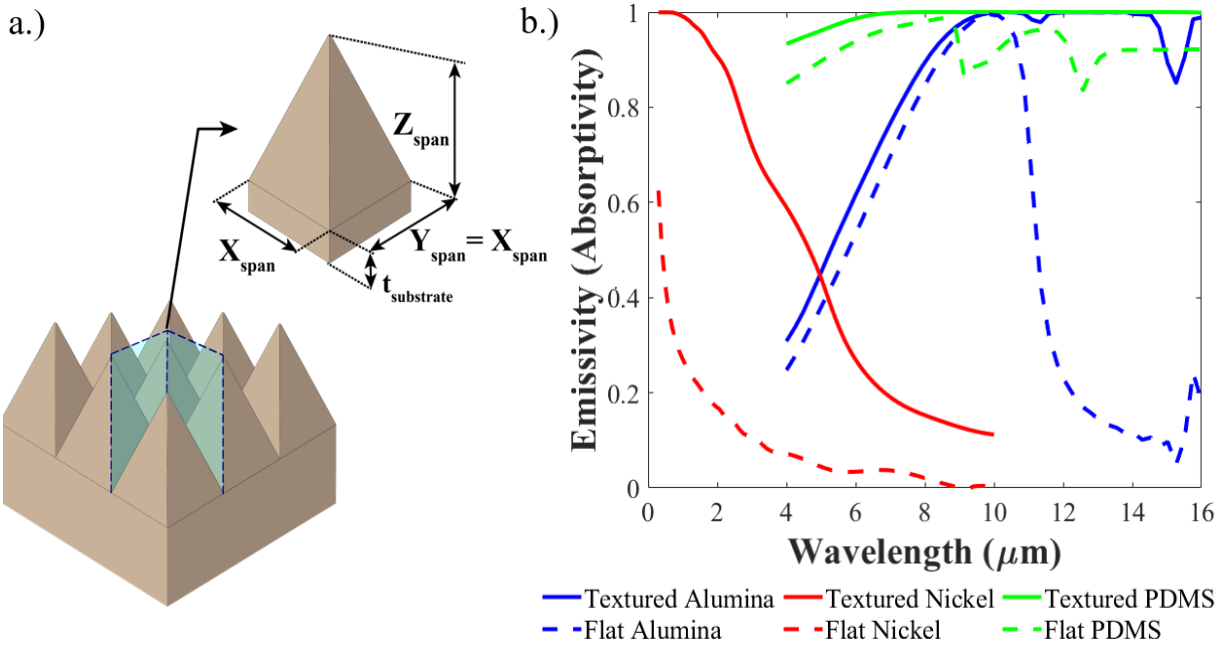

Figure 2-1 (a) Micropyramid geometry utilized in simulation. The blue region represents the imposed periodic boundary conditions, with the pyramid cut-out being the simulated unit cell. The 3-D unit geometry shown is extended infinitely in the X and Y directions. The z_{span} and x_{span} vary from 50 nm to 30 μm in simulations, and the y_{span} is set to be symmetric with the x_{span}. The substrate thickness is established per material to limit the impact of transmission – 1 um for nickel and 100 um for Alumina and PDMS simulations. (b) The emissivity of both optimized and flat nickel, alumina, and PDMS. The optimized nickel (z_{span}/x_{span} = 2.1/0.6 μm) result has a strong dependence on aspect ratio, the PDMS and alumina optimized cases (z_{span}/x_{span} = 15/5 μm and z_{span}/x_{span} = 16/6 μm, respectively) also show strong dependence on aspect ratio for the

polymers[19], [20], [51]. Solutions for both radiative heating and cooling demonstrate wide variation in design, but a common difficulty is engineering scalability, cost-effectiveness, and limited applications of the materials utilized. Micropyramid structures offer a simple and scalable design that can be patterned into a vast range of materials, allowing for a large design space.

In this chapter, we present the fundamental relationship between micropyramid geometry and thermal radiation control. By utilizing the spectrally dependent anti-reflective behavior induced by pyramidal topology [52], we can significantly enhance the thermal absorption of metallic surfaces and the thermal emission of ceramic and polymer surfaces. A generalized framework that combines thermal cost-function driven design optimization with finite-difference time-domain simulations to provide design criteria for micropyramid texturing that enhances the heating or cooling performance is shown. This is a far simpler optimization approach compared to more advanced techniques used previously for optical/thermal optimization, including machine learning models and deep-neural networks[17], [53]–[55]. As a result, the method is easy to implement and replicate for any number of domain variables or geometries, requiring no existing training data or advanced processes. In this study, nickel is selected as the basis for the heating material optimization due to its favorable material properties that enable its usage in solar absorption and high-temperature applications. For passive radiation cooling applications, it is established that introducing pyramidal topology further enhances the MIR emissivity of *Polydimethylsiloxane* (PDMS) and Alumina (Al_2O_3) surfaces. Both materials have a refractive index that generates emission in the IR spectrum which enables excellent passive cooling performance. PDMS is chosen due to the manufacturing processing being low-cost and scalable, ceramic materials

are far more environmentally adaptable, allowing for reliable radiative cooling over a wide range of operating temperatures. While we show results primarily for these three materials, the design criteria and physical insight presented from these materials can be used to extrapolate generalized design rules for other similar metallic, ceramic, and polymer materials.

2.2 Optics of the Micropyramidal Structure

The underlying principle of micropyramid anti-reflective behavior relies on the confinement of light within the structure as induced by the geometry. This is a size-effect driven process that is dependent upon two factors: the geometric design and the material(s) refractive index. To exemplify the importance of size on the outcome, it can be shown that pyramidal geometries with a period near to the optical wavelength (400 – 600 nm) are most optimal for the absorption of visible light [23]. The introduction of the pyramidal geometry enables the structure to reflect light multiple times, resulting in an increased optical path length and increasing the probability that the pyramidal structure absorbs the incident EM

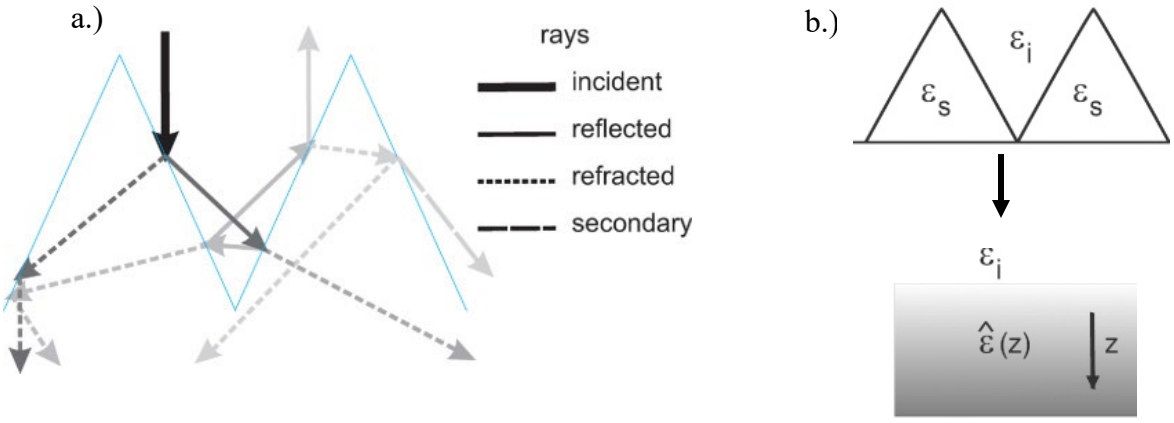

Figure 2-2 (a) Ray-approximation showing ray propagation in a pyramidal geometry - color intensity corresponds to ray intensity. (b) Visualization of the gradient in the permittivity function, printed from [27]

radiation[23], [26], [52]. In the case where a ray approximation can be used (when $\lambda << \Lambda$), the influence of the geometry can be easily visualized in Figure 2-2(a). In the case when the wavelength is larger or comparable to the structure (when $\lambda >> \Lambda$), the geometry can be visualized as inducing a gradient in the electric permittivity function (or the refractive index), as seen in Figure 2-2b. The influence of refractive index can be thought of as a fundamental limitation of geometric influence on spectral optical properties. Materials will have wavelength regions where geometric structuring can determine properties, but anti-reflective properties will have a minimal influence over a transmissive material, or a material where the refractive index is much greater than that of the surrounding medium (air, n = 1).

2.3 Micropyramid Simulation, Analysis, and Optimization Framework

2.3.1 Micropyramid Simulation Framework

A generalized form of the structure utilized in the simulation and optimization process is depicted in Figure 2-1. The illustration demonstrates both the periodicity of the design and the details of the 3D pyramidal unit cell simulated. The key geometric parameters of the unit cell are specified by the span of the pyramid's base and its height (x_{span} and z_{span} respectively). The case that is considered is where the structure's base is symmetric, so x_{span} is equal to the span along the y-axis (y_{span}). The "gap" distance between the edges of adjacent pyramids – which would be a consequence of typical fabrication techniques for periodic microstructures – is not considered in this analysis. The substrate thickness (s_{tub}) is set such that transmission through the simulation domain is negligible and thus this value varies with the chosen material.

Numerical simulations in this work are conducted using Lumerical's commercially available 2-D/3-D finite-difference time-domain (FDTD) solver. The FDTD method

discretizes a volume via a mesh and provides exact 3-D solutions for Maxwell's equations for non-magnetic materials. Specifically, the FDTD method solves Maxwell's curl equations:

$$\frac{\partial \vec{D}}{\partial t} = \nabla \text{ x } \vec{H} \quad (1)$$

$$\vec{D} = \varepsilon_0 \varepsilon_r(\omega)\, \vec{E}(\omega) \quad (2)$$

$$\frac{\partial \vec{H}}{\partial t} = \frac{1}{\mu_0} \nabla \text{ x } \vec{E} \quad (3)$$

Where H, E, and D are the magnetic, electric, and displacement fields, respectively, while ϵr(ω) is the complex relative dielectric constant[56]. These equations are solved on a discrete spatial and temporal grid, providing results for the electric and magnetic field in a material, ultimately

including both dispersion and absorption[57], [58].

The simulations utilize the unit cell depicted in Figure 2-1 in conjunction with periodic boundary conditions in both the x and y-directions to simulate a semi-infinite surface microstructure on the x-y plane. Perfectly matched layers (PML) are used at the top and bottom of the simulation domain to prevent boundary reflection. A plane wave source is used for both normal incidence (Polar Angle, θ) and angular incidence simulations, but in the case of an angular injection angle, BFAST/Bloch periodic boundary conditions replace the periodic boundary conditions. Our plane wave source utilizes a transverse-electric (TE) polarization mode for all simulations, and we set the polarization angle (φ) to be 0° for all simulations. Frequency-domain field and power monitors are positioned both above the plane wave source and above the bottom PML to monitor the reflection (R) and transmission (T) respectively. The structure's spectral emission can be calculated from $\varepsilon = 1 - R - T$, assuming Kirchhoff's law ($\alpha = \varepsilon$) is valid. For completely opaque structures, the

computation of emissivity reduces to $\varepsilon = 1 - R$, but due to the negligible extinction coefficient (k) of both alumina and PDMS within the visible and NIR regions, we use both R and T in the calculation of spectral emissivity.

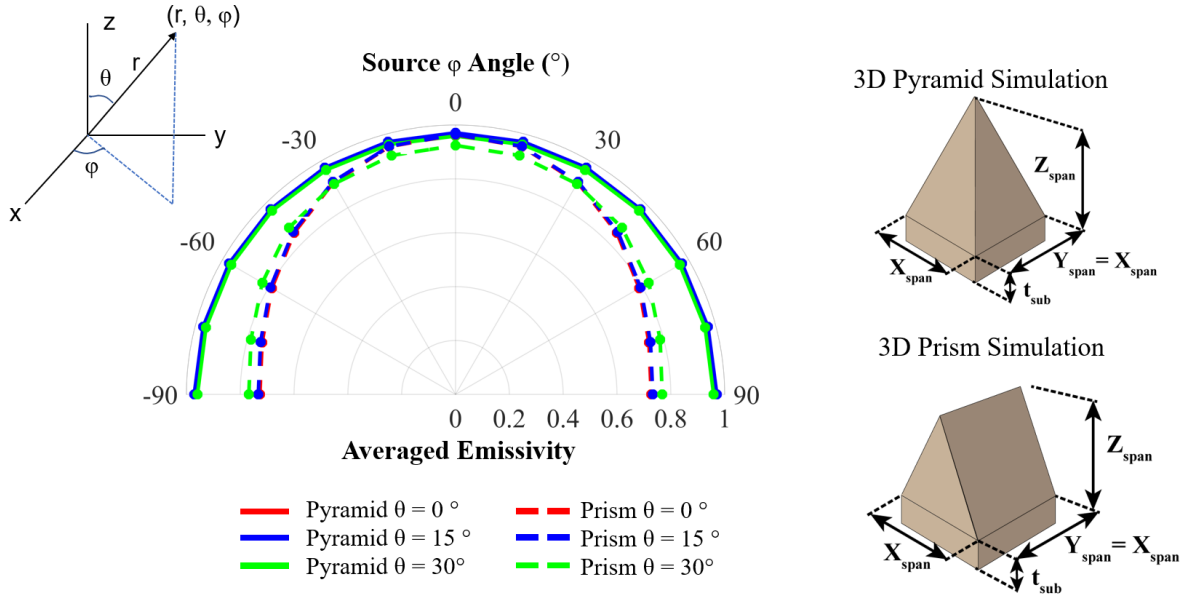

Figure 2-3 Variation in the averaged emissivity (0.3 – 2 um) for a pyramid and the 3D extrapolation of a pyramidal cross-section (triangular grating structure, referred to as a "prism") with changes in the incident angle ϕ. Whereas the Pyramid demonstrates exceptional omni-directionality, even in the case where the plane wave incident angle θ is varied, the prism structure shows a significant reduction in emissivity with changes in ϕ. Simulating the system in 3D allows for the optimization of materials at non-zero incident angles and provides an overall more accurate depiction of the optical properties when compared to 2D simulations for this geometric configuration. The value for emissivity shown is an averaged value across the

2.3.2 Thermal Optimization and Analysis Framework

To find material geometry configurations that provide optimal results for a variety of different material types, a constrained minimization algorithm is employed to drive the numerical simulations. As will be noted in the results section, although parametrically driven geometric parameters can yield reasonably optimized solution sets, the constrained minimization approach can result in more optimal geometric parameters in a much shorter timeframe. This is especially true for more complex geometric designs with more optimization parameters, as parametric optimization becomes increasingly impractical as

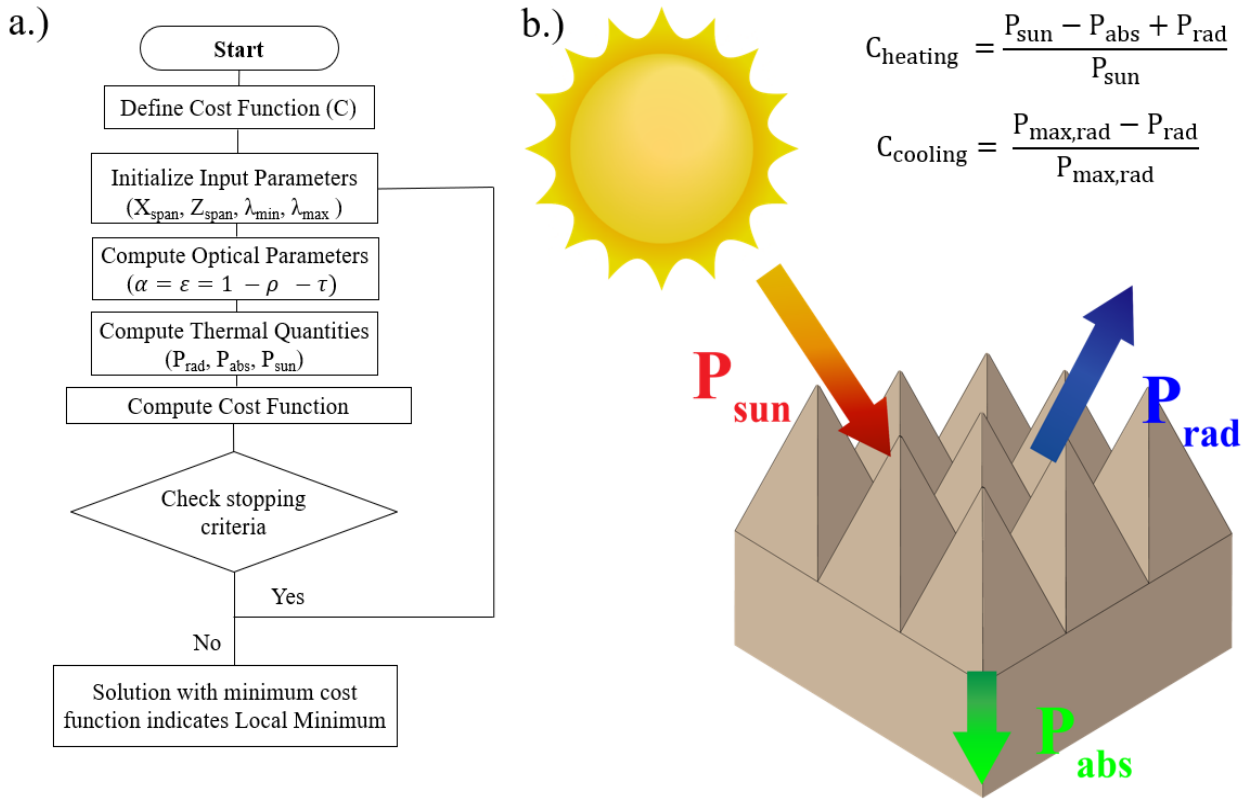

Figure 2-4 (a) Flowchart showing the optimization methodology. Gradient descent optimization tools within MATLAB are linked to FDTD simulations to optimize optical properties for intended thermal performance based on a chosen cost function ($C_{heating}$ or $C_{cooling}$). (b) Cost functions visualized with a heat-flow system diagram. The convection/conduction contribution (Pconv+cond) and atmospheric contribution (Patm) are not utilized in the present study.

the design space grows. In this chapter, the goal is a generalized algorithmic framework for optimizing pyramidal microstructures, so only two parameters (x_{span} and z_{span}) are optimized. The method itself, however, can easily be extrapolated to thermally optimize materials that feature nanotexturing, multilayer structures, coating(s), complex geometry, etc.

As seen in Figure 2-5, the optimization process can be divided into several major parts: the objective function (cost function), design factors, and the minimization function itself. Beginning with a depiction of intent of the surface material – either to absorb solar radiation or for thermal emission (Figure 2-5 (b)). – a minimization cost function is defined. The objective (or cost) function serves as a mathematical quantification of a design's thermal performance for the chosen application. For both heating and cooling applications, the cost function has been designed such that in the ideal scenario the constituent thermal terms cancel, and the objective function value becomes 0, lending to the minimization process. In the instance of heating, the primary thermal goal is to minimize the amount of heat lost in the IR while maximizing the amount of incident radiation absorbed[16]. We define the objective function for this scenario to be generally defined by the heat transfer balance of,

$$C = \frac{P_{solar} - P_{absorbed} + P_{emitted}}{P_{solar}} \tag{4}$$

We define this more rigorously as,

$$C = \frac{\int_{\lambda_{min}}^{\lambda_{max}} I_{AM1.5}(\lambda)d\lambda - \int_{\lambda_{min}}^{\lambda_{max}} \varepsilon(\lambda) I_{AM1.5}(\lambda)d\lambda + \int_{\lambda_{min}}^{\lambda_{max}} \varepsilon(\lambda) I_{BB}(\lambda, T)d\lambda}{\int_{\lambda_{min}}^{\lambda_{max}} I_{AM1.5}(\lambda)d\lambda} \tag{5}$$

Where $I_{AM1.5}$ is defined as the solar irradiance for an airmass value of 1.5, I_{BB} is the spectral radiance for a blackbody, and $\varepsilon(\lambda)$ is the spectral emissivity of the surface. The first term is the maximum amount of power that is available for the surface to absorb. For the majority of applications solar irradiation is dominant, so we define the maximum amount of power available to be a function of the solar spectrum. This term is independent of material parameters and can be treated as a constant heat flux. The second and third terms are the amount of incident radiation that is absorbed by the surface and the amount of power emitted by the surface respectively. Atmospheric contributions are neglected in the cost-functions utilized in this work. Atmospheric contributions are relevant for thermal temperature estimations – particularly for passive cooling [18] – but is significantly smaller than the thermal emission and thermal absorption so we choose to not include it in the cost functions. It can be accounted for, however, by including an additional thermal offset term like the emitted radiation term in Equation 1. We also do not include the effects of thermal convection/conduction as the surface emissivity does not impact the heat flux from convection and conduction. The entire cost function is normalized by the maximum power available yielding a value for the cost function that is between 0 and 1. Before normalization, the equation has the unit of area independent power, W/m^2.

The cost function used in the optimization of radiative cooling surfaces minimizes energy absorbed while maximizing emission. We define the objective function in a similar fashion to the heating case with the heat transfer balance,

$$C_{cooling} = \frac{P_{max,rad} - P_{rad}}{P_{max,rad}} \quad (6)$$

$$C_{cooling} = \frac{\int_{\lambda_{min}}^{\lambda_{max}} I_{BB}(\lambda,T)d\lambda - \int_{\lambda_{min}}^{\lambda_{max}} \varepsilon(\lambda) I_{BB}(\lambda,T)d\lambda}{\int_{\lambda_{min}}^{\lambda_{max}} I_{BB}(\lambda)d\lambda} \quad (7)$$

While there is a small amount of absorption in the optical wavelengths by emissive materials (PDMS and alumina in this case) it is small enough that we can omit it from the heat transfer balance shown in Equation 3. Similarly, we do not include the effects of atmospheric emission in the heat balance equation to maintain a simple relationship between the maximum emission and achieved emission by the surface in the optimization process. The Heat-flux computations shown for both the heating and cooling cases are computed using a blackbody temperature of 300 K. For the thermal absorption estimations of flat/textured nickel, the value presented is P_{abs} at a I_{BB} Temperature of 300 K between λ = 300 nm to 2500 nm. Similarly, the thermal emission fluxes (P_{rad}) of alumina and PDMS are computed between λ = 4 μm to 16 μm at $I_{BB}(T)$ = 300 K.

For a micropyramid texture like the depiction in Figure 2-5 (a), only two parameters (x_{span} and z_{span}) are optimized but the method can accommodate many more design variables. The design parameters (x_{span} and z_{span}) are defined and passed to the simulation domain for each iteration. The simulation domain utilized in the simulation and optimization process is depicted in Figure 2-5 (a). The illustration demonstrates both the periodicity of the design and the details of the 3D pyramidal unit cell simulated. The key geometric parameters of the unit cell are specified by the span of the pyramid's base and its height (x_{span} and z_{span} respectively). We only consider the case where the structure's base is symmetric, so x_{span} is equal to the span along the y-axis (y_{span}). The "gap" distance between the edges of adjacent pyramids – which would be a consequence of typical fabrication techniques for periodic microstructures – is not considered in this analysis. The substrate thickness (t_{sub}) is set such

that transmission through the simulation domain is negligible and thus this value varies with the chosen material.

2.4 Optimization of Micropyramid Topology for Radiative Heating and Cooling

The combined results of the nickel micropyramid optimization process are shown in Figure 2-1 (b). The minimization process relies on a gradient descent interior-point optimization algorithm[59] that optimizes the *x* span (x_{span}) and *z* span (z_{span}) of the pyramidal geometry (represented in Figure 2-5 (a)) by minimizing a cost function defined by Equations 4 and 5, where P_{solar} is defined as the maximum amount of solar irradiation available to be absorbed, P_{abs} is the amount of thermal energy absorbed by the surface, and

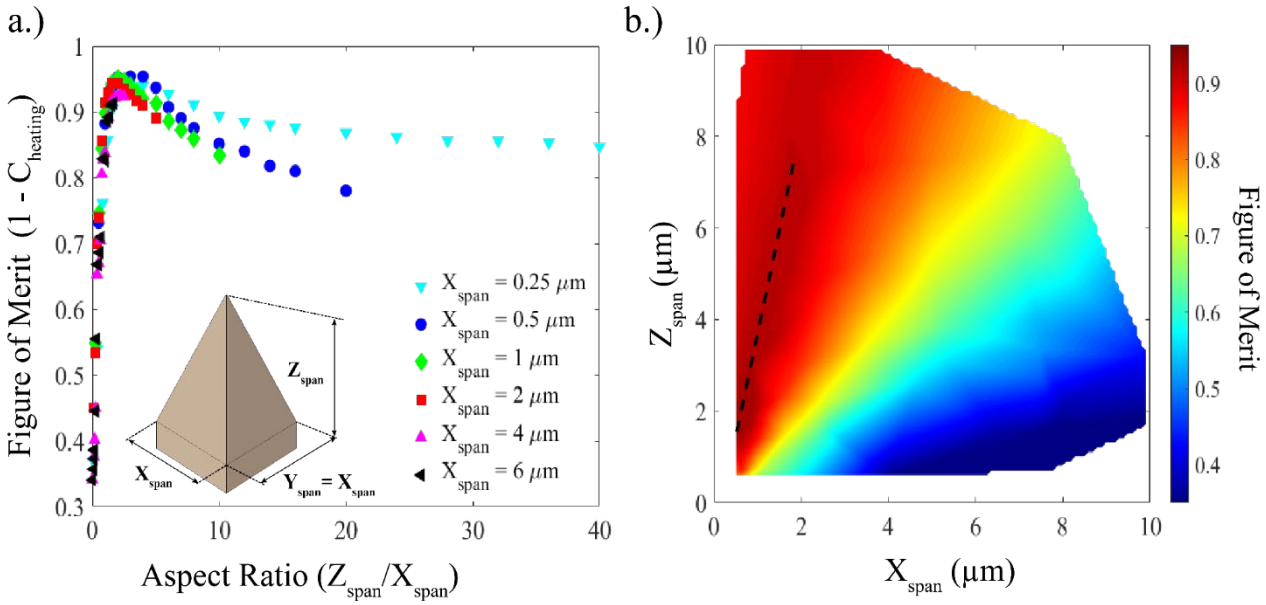

Figure 2-5 (a) The relation between the normalized aspect ratio and figure of merit plotted for the nickel texture with three different fixed base dimensions (x_{span} = 0.25, 0.5, 1, 2, 4, and 6 μm). In this plot, z_{span} is swept while x_{span} is held constant. (b) Contour plot of algorithmically derived solutions over a range of x_{span} and z_{span} combinations. Over 1500 solutions obtained from optimizations with different initialization points are used. Data interpolation is used to fill the remaining grid data. Among many FOM > 0.9 solutions an optimal region emerges as visualized by the dark-red region in the bottom left corner and along the dashed-black line.

P_{rad} is the amount of lost to emission by the surface. Both P_{abs} and P_{rad} are functions of the surface emissivity computed within FDTD simulations. The cost function is normalized by the maximum available power such that $0 < C < 1$. For the sake of visualization, we present the optimization results using a normalized figure of merit (FOM) defined by Equation 8, such that a value close to one indicates an optimal solution.

$$FOM = 1 - C_{heating} \tag{8}$$

For the nickel optimization process, we utilize a plane wave source of normal incidence in the FDTD simulations that ranges from 300 nm – 10 μm. We choose this wavelength (λ) span as λ = 300 – 2000 nm is the most relevant region for solar absorption, and due to the high refractive index in the IR, nickel is observed to asymptotically approach an emissivity ~ 0.1-0.2 beyond λ = 10 μm for most nickel micropyramid x_{span} and z_{span} dimensions. Figure 2-5(b) shows a contour map of geometric designs that result from numerous iterations of the minimization process for nickel when the cost function described by equation (8) is employed. To provide a reference point, untextured nickel – simulated as an untextured 1 μm thick nickel substrate in FDTD – has a computed FOM of ~ 0.35. This is a result of the untextured nickel substrate absorbing nearly 37% of incident solar irradiation while only losing a fractional quantity of thermal power to emission in the IR due to low IR emissivity. Comparatively, Figure 2-4(a) demonstrates that even un-optimized surface structuring via micropyramids drastically increases the FOM to 0.6 – 0.7, which is equivalent to a solar absorption efficiency of 60 - 70%, representing a 25-35% increase compared to bare nickel.

In Figure 2-5(b), the plotted contours shows that the minimization process yields a host of solutions that are quintessentially optimal and have nearly negligible variation in optical performance. The global optimum computed from multiple iterations of the optimization process has a heating FOM of 0.963, which occurs at x_{span} = 0.65 μm and z_{span} = 2.1 μm. Both the emissivity and reflectivity of this structure can be observed in Figure 2-5(b), but the exceptional increase of absorptivity to a value near $\alpha = 1$ between the wavelengths of 300 - 2000 nm results in an absorption efficiency of 98.6%. Specifically, this structure can be predicted to absorb 986.6 W out of the available 1000.4 W for AM1.5 per square meter between λ = 300 nm and λ = 10 μm. Thermal emission leads to a thermal loss of 23.9 W/m2 for the optimized structure, which is 19.1% of the maximum blackbody emission between λ = 300 nm and λ = 10 μm at 300 K. By comparison, two local minima occurring at (x_{span} × z_{span}) of (0.51 × 1.45) μm and (0.9 × 1.98) μm have absorption efficiencies of 97.3% and 96.9%, respectively. Accordingly, their FOMs are computed as 0.96 and 0.953. Although the absorption efficiency decreases by ∼1-1.5% for both local optimums when compared to the global optimum, a decrease in thermal emission - 13.8% and 13.7% of the blackbody limit respectively—results in the global optimum having a FOM that is only 0.3 – 1% higher than the local optimum geometries. Thus, while finding a global optimum using our gradient-descent based optimization would be inefficient compared to methods such as particle swarm optimization [60] or genetic algorithms[61], finding a local minimum that has exceptional performance occurs very early in our process and we can reliably and rapidly reach designs that achieve absorption efficiencies exceeding 94-96%.

The overall trend in the heating FOM can thus be described predominantly as a function of the aspect ratio of the structure. This trend can be observed in Figure 2-5(a),

which plots the FOM as a function of the aspect ratio. It is important to note that while the aspect ratio is intrinsically unitless, we choose to define aspect ratio (AR) as:

$$Aspect\ Ratio = AR = \frac{Z_{span}}{X_{base}} \tag{9}$$

where x_{base} is constant and used to normalize while z_{span} is swept in the simulations. While we observe a trend between the aspect ratio and FOM, this distinction is made such that the necessity of a nanometer/micrometer scale periodicity on the absorption enhancement and anti-reflective properties is not lost. From Figure 2-5(a) we conclude that, based on a x_{base} from 500 nm to 2 μm, increasing x_{span} will rapidly increase the FOM until it reaches a maximal value ~ 0.92 – 0.96 for an aspect ratio of ~2 - 4. After the local maximum for a x_{base} the FOM will then decrease. This trend can be explained as a function of both the thermal and absorption efficiency increasing until a critical maximum when the absorption efficiency saturates while the thermal emission efficiency continues to increase. At larger ARs, the absorption efficiency decreases while the thermal emission efficiency continues to increase.

The surface optical properties result from the introduction of anti-reflective behavior because of the patterned periodic structure as visualized in Figure 2-6 (a-d). Two geometries are plotted in Figure 2-6 (a-d) – Design I (a,c) and Design II (b,d). Design II is the optimized geometry for the nickel heating cost function, and Design I is a low-aspect ratio (AR = 0.5) structure. For comparison, both designs have the same x_{span} (0.65 μm). As the simulation domain has a near-zero transmission due to the intrinsically high extinction coefficient, the driving factor behind the emissivity/absorptivity enhancement is the decrease in reflection as a function of the geometry. As seen in Figure 2-6 (a), the maximum intensity of electric field for the same wavelength remains contained in the optimized geometry and unconfined

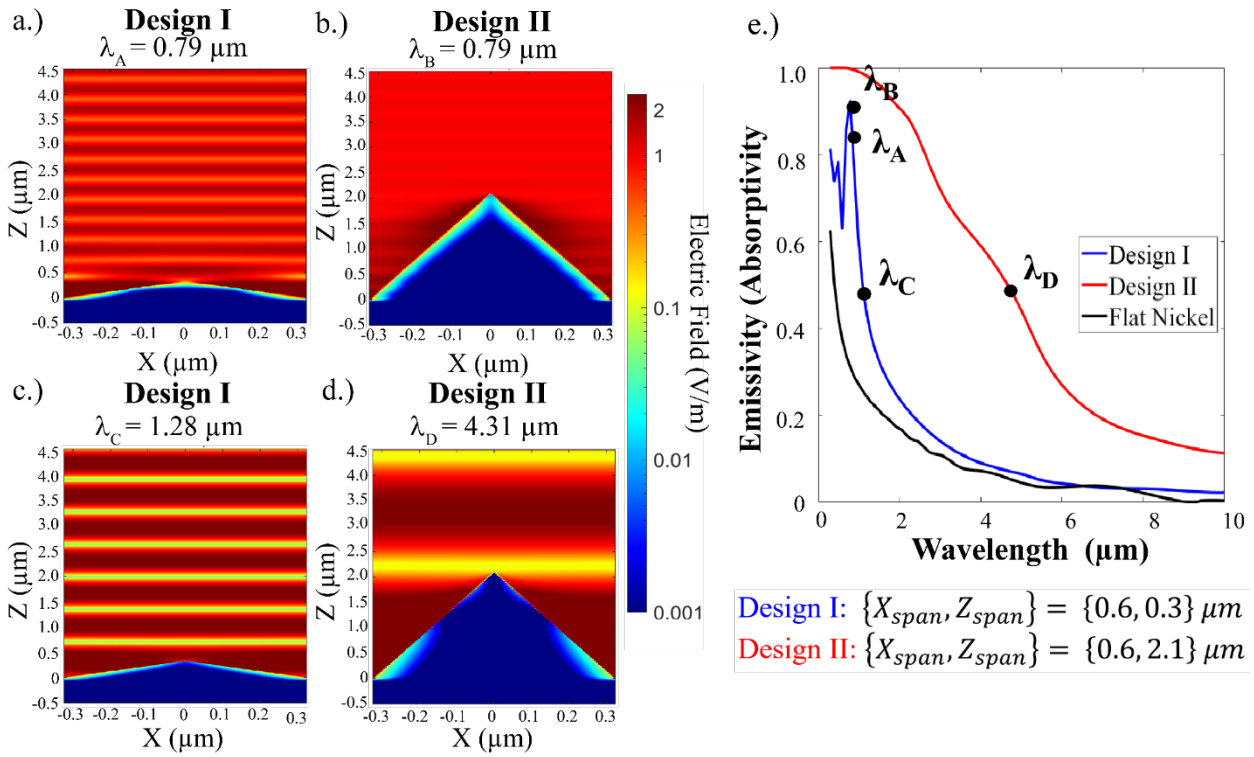

Figure 2-6 (a-d) Plots of the x-z plane (cross-sectional) Electric field (V/m) demonstrate that the optimized structure (Design II) more thoroughly confines the electric field within the texture, significantly enhancing the solar absorptivity. (a,b) At wavelength A and B (0.79 μm), where the emissivity of Design I reaches a peak– strong electric field confinement is observed in both structures. (c, d) At wavelength C and D, the effect of texture is apparent. The confinement of the electric field by Design II leads to Design II having an emissivity of 0.5 at λ_D = 4.31 μm while Design I has an emissivity of 0.5 at λ_C = 1.28 μm. The higher aspect ratio Design II leads to a much slower decay in emissivity than with Design I. A log-scale is used to show the absorption more thoroughly in (a-d). (e) The emissivity of both Design I (low-aspect ratio) and Design II (optimized) structures are shown compared to the untextured case (Black), with the reflectivity of either structure visualized by the dashed lines.

by the low-AR structure. It is evident that the higher AR structure maintains confinement – and increased absorption – over a much wider wavelength region compared to the low AR micropyramid texturing. The magnetic field component plays a limited role in the enhancement of the absorption compared to the electric field.

While the results shown in Figures 2-5 and 2-6 occur using a 3-dimensional (3D) FDTD design space, our optimization process readily transfers to a 2-dimensional (2D) design space. Reducing the geometry to 2D yields a grating structure as the simulation domain assumes the triangular shape (x_{span} and z_{span}) is infinitely extruded along the *y*-axis. For a plane wave with an injection angle of $\theta = 0°$, there are minimal differences in the absorptivity computed between the 2D and 3D domains. The computed spectral emissivity of two optimal nickel geometries are plotted in Figure 2-7 for different plane wave source incident angles (θ). A key difference between 2D and 3D simulations, however, can be seen in Figure 2-7 where the 3D pyramidal geometry has near omni-directional absorption properties that are not observed in a 2D grating structure that has been extruded into three-dimensions. While a 2D cross-section provides an excellent estimation of the 3D micropyramid's optical properties, there is a slight overestimation of the emissivity for this structure. When the 2D structure is simulated with a third dimension, the results of the grating structure geometry

vary greatly from the pyramidal geometry. This discrepancy is most apparent at different angles, as the pyramidal geometry demonstrates consistently omnidirectional properties.

2.5 Optimization of Radiative Cooling Materials using Micropyramids

The results of the alumina and PDMS micropyramid optimization processes are shown in Figure 2-8 and Figure 2-10, respectively. Similar to the nickel optimization, the optimization occurs by minimizing a cost function that is defined by Equation 3 and 4. where $P_{max,rad}$ is defined as the maximum amount of thermal emission that is possible according to Planck's law[2], and P_{rad} is the thermal energy emitted by the surface. P_{rad} is a function of the surface

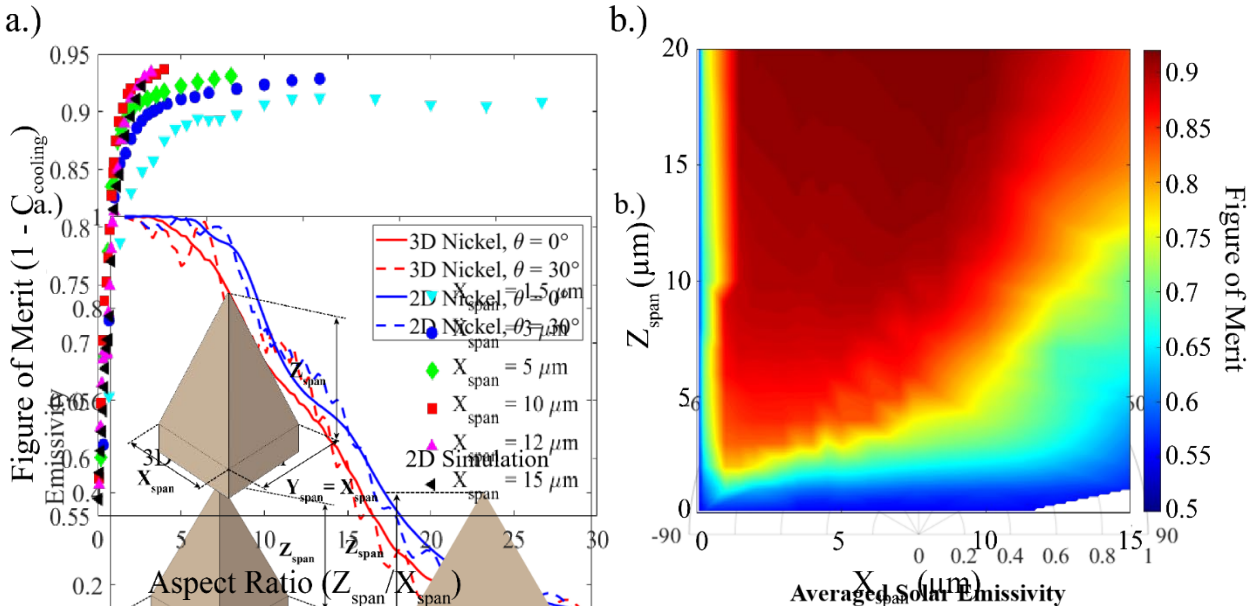

Figure 2-8 The relation between the normalized aspect ratio and figure of merit plotted for six fixed base dimensions *(*x_{span} = 1.5, 3, 5,10, 12, and 15 μm*)*. (a) Contour plot of algorithmically derived solutions over a range of X and Z span combinations. Over 1300 solutions resulting from many optimization runs with different initialization points are plotted. Data interpolation is used to fill the remaining grid contours. The Optimal region can be identified from x_{span} ~ 5 – 8 μm and z_{span} ~ 15- 20 **(b)** The relation between the normalized aspect ratio and figure of merit plotted for six fixed base dimensions (x_{span} = 1.5, 3, 5,10, 12, and 15 μm).

emissivity computed within FDTD simulations. For these thermal calculations, we define the surface emission temperature to be 300 K. The FOM presented in Figures 2-8 and 2-10 is defined by equation (6). For both the alumina and PDMS optimizations, we apply a plane wave source that ranges from 4 μm – 16 μm. This wavelength span is utilized because the blackbody distribution for a body at 300 K centers near ~10 μm, with over 60% of the total thermal emission possible occurring in this span. Simultaneously, both materials are highly transmissive in the VIS/NIR region for the thickness required by the simulation to negate MIR transmission (100 μm). Consequently, the VIS/NIR response of the cooling materials is not a function of geometric optimization and is instead a function of the substrate.

The contour plot of solutions visualized in Figure 2-8(b) demonstrates that a large range of geometric combinations for alumina yields highly optimal results. The results in Figure 2-8 (a) for FOM vs. Fixed-Base AR also establish that the FOM of the ceramic texture has a strong dependence upon x_{span}. For the results shown in Figure 2-8 (a), the z_{span} is limited to 40 μm. Based on the results shown in Figure 2-8 (a) and (b), however, the near equivalency in thermal emission between structures with AR > 2-5 mitigates the necessity of simulating structures beyond this constraint. The trend in the FOM is to asymptotically approach a maximum that is dependent upon x_{span} for the structure. When x_{span} = 10 μm, the FOM approaches ~ 0.95, indicating that the geometry can emit ~95% of the theoretical maximum at 300 K. Comparing z_{span} = 5 μm, 10 μm, 20 μm, and 40 μm for a fixed z_{span} of 10 μm, the FOM is 0.753, 0.856, 0.920, and 0.937, respectively (AR = 0.5, 1, 2, 4). This corresponds to an increase in FOM of ~0.22, 0.32, 0.39, and 0.41 when compared to bare alumina. The asymptotic behavior between AR and FOM indicates that while the maximum for a given z_{span} might not be observed when the z_{span} is constrained, increasing z_{span} will not

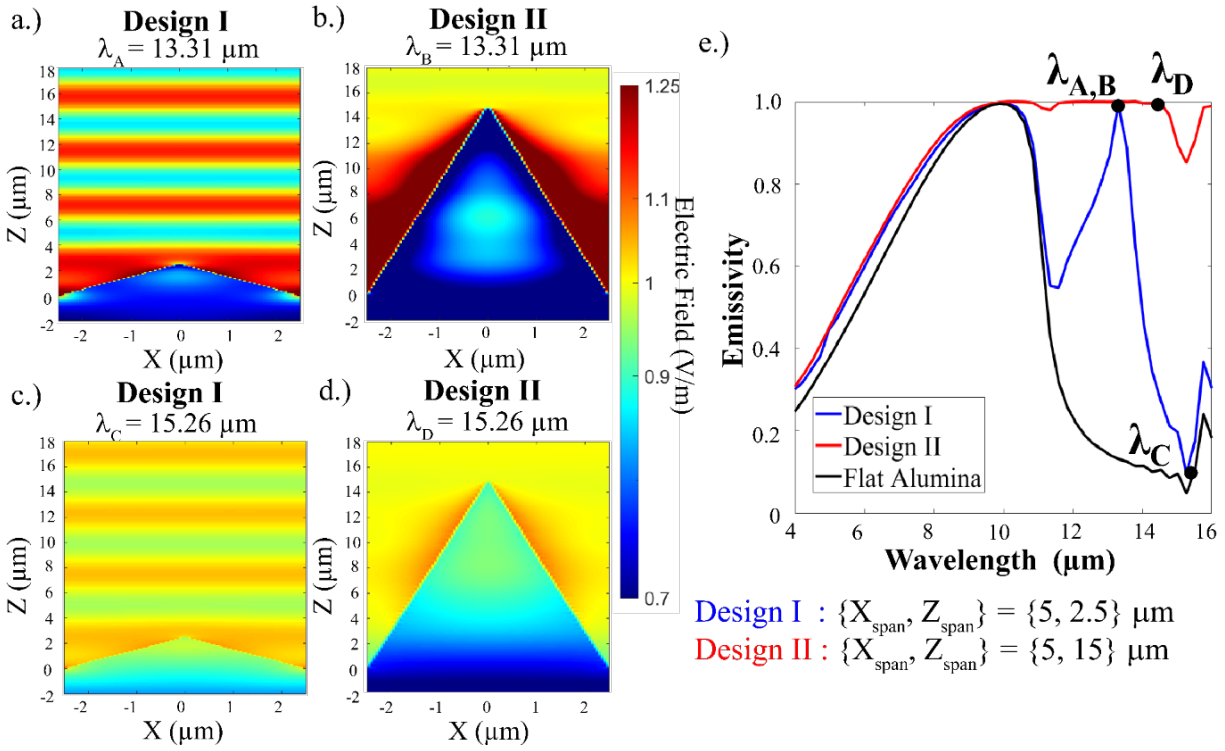

Figure 2-9 (a) Electric field cross-sections for alumina that demonstrate that the optimized structure (Design I) more thoroughly confines the electric field inside the texture, significantly enhancing the solar absorptivity. Wavelength A (13.06 μm), where the emissivity of Design I is maximal –and wavelength B (15.27 μm), where the emissivity of Design II reaches a minimum. A log-scale is used to show the absorption more thoroughly within the micropyramid at both points. (b) The emissivity of both Design I (optimized) and Design II (low aspect ratio) structures are shown compared to the untextured alumina case (Black), with the reflectivity of either structure visualized by the dashed lines.

significantly impact the FOM. The optimization of the cooling cost function for alumina quickly yields local minima beneath $C_{cooling}$ = 0.1 (FOM = 0.9) but this solution is unlikely to contain the entirety of the optimal geometric region due to the constraints utilized.

The negligible difference between the cost functions at higher ARs is a result of a saturation in emissivity. The results plotted in Figure 2-9(e) show that the micropyramid pattern significantly reduces reflection that occurs in the MIR beyond λ = 10 μm. The anti-

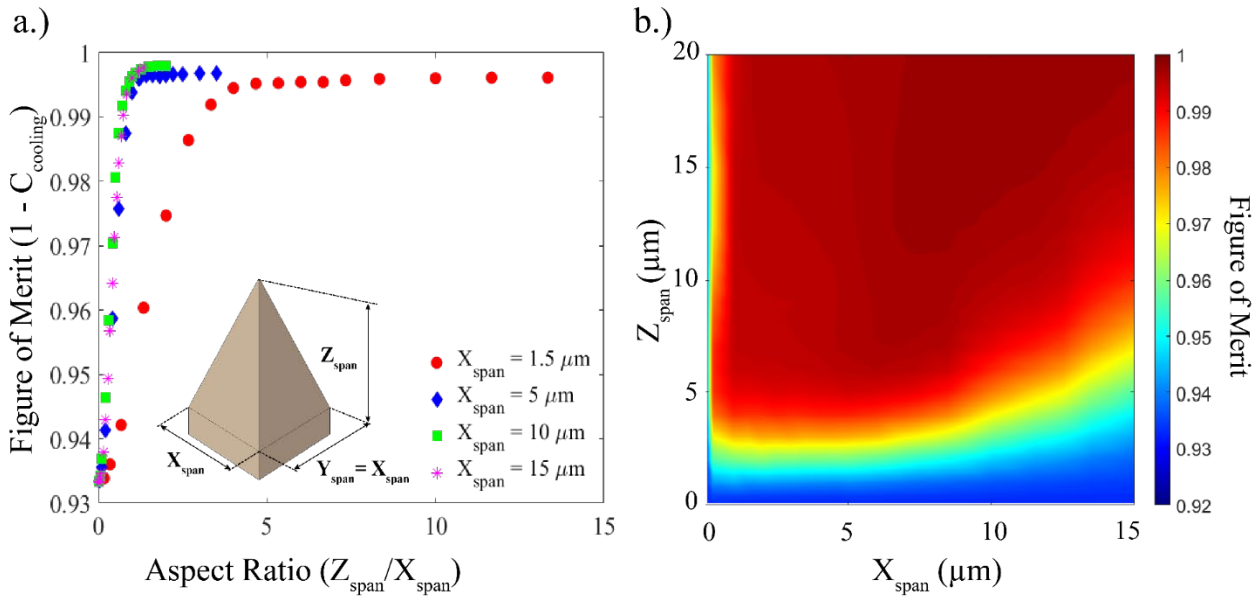

Figure 2-10 (a) The relation between the normalized aspect ratio and figure of merit plotted for four fixed base dimensions (x_{span} = 1.5, 5,10, and 15 μm*).* The relation between the aspect ratio and figure of merit is shown to asymptotically approach 1. Higher aspect ratio structures are shown to approach higher values for FOM, but with larger base dimensions, the necessity of high aspect ratio structures is minimized as the structure's emission reaches a maximal point and the aspect ratio no longer influences the optical properties. (b) Contour-plot of algorithmically derived solutions over a range of X and Z span combinations for PDMS. Like alumina, identifying the bounds of the optimal region for the PDMS texture is more challenging because of the geometric scale and time required to simulate larger structures.

reflective behavior can again be observed in Figure 2-9 (a-d) to be a function of the confinement of the electric field by the geometry. While the efficiency of the anti-reflective behavior is a function of the geometry, the emissivity can only range from 0 to 1, so the influence of geometry on the emissivity decreases both as the AR increases and X_{span} increases. This phenomenon is seen in Figure 2-9(e), in which a low-AR (0.5) and high-AR (3.0) geometry are plotted simultaneously. Compared to the bare alumina case, the low-AR micropyramid pattern has a drastic effect on the emissivity by significantly decreasing the

spectral reflectivity when $\lambda > 10$ μm. For the high-AR geometry, the emissivity is almost a unity across the spectrum, leaving marginal room to further improve the emissivity.

Although PDMS has an innately high emissivity in the MIR/NIR regions due to its intrinsic refractive index[62], employing the same cooling optimization procedure results in the same anti-reflective trend and subsequent increase in MIR emission that has been observed in alumina. The cooling cost function equation defined by Equation 6 and 7 that was used for the alumina optimization results in a FOM = 0.91 ($C_{cooling} = 0.09$) for untextured PDMS. The results shown in Figure 2-10(b) exemplifies that even minor texturing of a PDMS surface can increase the FOM to a value near 1.0, indicating that textured PDMS is a near perfect NIR/MIR emitter when textured. Despite having a characteristically high emissivity, the introduction of micropyramid texture to the surface reduces the already minimal reflectivity to a value near 0 in the NIR/MIR. The trend observed in Figure 2-10 (a) is that even low-AR texturing with AR < 1 yields emission efficiencies of 95-96%, with AR > 2 PDMS micropyramids displaying thermal emission efficiencies of ~99% or higher for pyramidal base dimensions near the IR wavelength.

2.6 Discussion

Planar metallic surfaces are generally poorly absorbing materials – this is due to most metals being conductive and thus featuring a steep complex refractive index curve that leads to untextured metals being highly reflective. Although the characteristically high reflectivity of metals can be reduced by introducing severe oxidation at the surface, we have demonstrated that strong absorption within the visible and NIR regions is possible by microscale geometric patterning of a nickel surface without the need for an oxide coating or nanoscale texturing.

The relation between the absorptivity enhancement and geometry of the texturing is fundamentally linked via the material's refractive index. For nickel, the refractive index in the VIS/NIR enables strong geometrically based anti-reflective behavior. Thus, nickel is very well suited to optimization as a passive radiative heating material. Subsequently, the goal of the optimization process for nickel is to maximize the amount of energy absorbed – particularly in solar relevant wavelength regime of 500 – 1000 nm – while minimizing the amount of energy lost to emission. While further emissivity enhancement is possible geometrically beyond the NIR, this is counter-productive to the goal of minimizing energy loss via emission. If the optimization intent is high temperature cooling instead of solar absorption, then the increased importance of MIR/NIR emissivity to the spectral distribution would necessitate higher emissivity texturing for λ beyond 3 - 4 μm. While we do not demonstrate a metallic high temperature cooling optimization procedure in this work, this form of optimization is easily performed with our method by adjusting the cost function equation and the emission temperature.

The absorption enhancement provided by the nickel texturing in the VIS/NIR is a combined effect of the complex refractive index and the geometric scale of the nickel micro/nanopyramidal surface topology. For wavelengths beyond the solar spectrum (> 2000 - 3000 nm) the complex refractive index of nickel begins to rapidly rise, which leads to surface morphology having a reduced impact on the optical properties of the surface. Figure 3(a) validates that while increasing the AR to form very steeply angled structures (AR > 5) can lead to a moderately increased absorption coefficient in the IR-band, it is far more limited in scope than the geometric enhancement available in the visible/NIR. From simulations with other metals such as silver and aluminum shown in Figure 2-11, we observe that

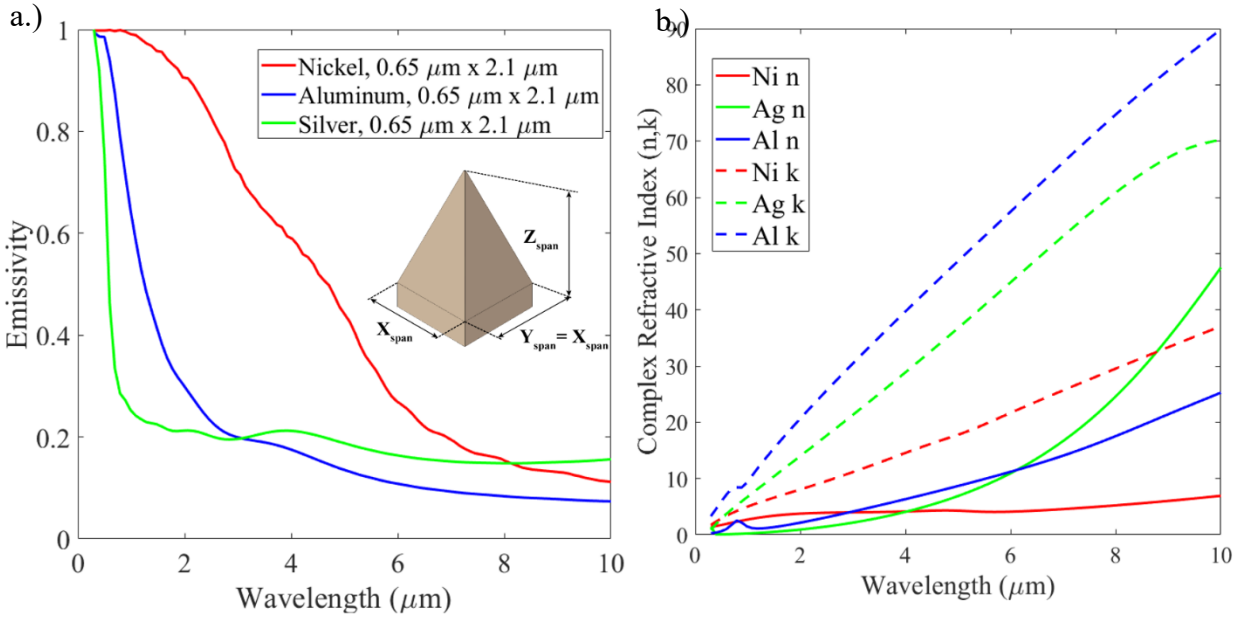

Figure 2-11 (a) Comparison of the same structure simulated in different materials (Ag, Al, and Ni) that highlights how geometry has impact on particular materials over a broad-spectrum region. Geometry has a lessened impact as the complex refractive index is increased relative to the medium index (in this case air) (b) With higher index materials (Al, Ag) the impact of geometry on the optical properties is significantly lessened.

geometric-dependent anti-reflective behavior has a far more limited spectral range of influence. This is predominantly due to a much higher slope in the refractive index for these materials that limits the spectral enhancement provided by surface geometry. Additionally, the optimization process yields that the most optimal results have x_{span} comparable to solar spectrum wavelengths ($x_{span} \sim 500 - 2000$ nm for $\lambda_{solar} \sim 300$ nm – 2400 nm).

The results shown are for nickel, alumina, and PDMS are to be expected as localization and resonance effects as a function of geometry are most effective when the structure's period dimension is sub-wavelength[63]. Micropyramid textures are also known in the

broader community as a surface-relief gratings or anti-reflection gratings (ARGs). when the incident wavelength is much larger than the critical dimensions (Λ) of the ARG, or $\lambda >> \Lambda$, the electromagnetic propagation through the structure can be approximated via an effective-medium electric permittivity function that has a gradient in the *z*-direction[23], [27]. The interaction of light with sub-wavelength structures (SWS) can also be approximated by Maxwell-Garnett (MG) [64], [65] or Bruggeman[66] effective-medium theory (EMT) models. Both of these EMT approximations represent the heterogeneity of a ARG in terms of a homogenous medium with a single effective complex refractive index [63].

For our micropyramid based ARG topology, as the complex refractive index in the IR (where $\lambda >> \Lambda$, for small x_{span} nickel textures) is large, the structure behaves much like untextured nickel, with a high reflectivity. In the case where $\lambda << \Lambda$, the structure can be visualized using geometric optics, with light potentially being preferentially confined by the geometry due to the multiple scattering interfaces induced by the texture[23], [27]. While increasing x_{span} to being comparable to IR wavelengths does have the expected effect of slightly increasing emission properties in the IR, it also causes the solar absorption properties to be significantly reduced. This effect can be visualized in Figure 3(a), where pyramids featuring a larger base dimension also have a reduced figure of merit due to the reduced inability to absorb incident solar radiation in the visible spectrum. This relation ultimately leads to the combination of an AR of 2 – 4 with a $x_{span} \sim$ 500 – 2000 nm being optimal for solar absorption in nickel. It also explains the concave relation between FOM and AR observed in all of the samples shown in Figure 3(a)Increasing the aspect ratio beyond 2 – 4 for nickel reduces the FOM as it increases the IR emissivity and thereby the thermal emission. The increase in solar absorption and thermal emission with aspect ratio – as

observed in Figure 3a and in the local minima presented in the results section– can be attributed to subwavelength structure behavior when the spacing of the array is smaller than the incident wavelength [63]. Additionally, increasing a metallic ARGs aspect ratio (depth/period) has been previously shown to slightly increase the broadband emissivity of metal structures, including nickel [67], [68] and our results demonstrate this behavior.

Although periodic microstructures significantly enhance the spectral absorption of metals in the VIS/NIR, and therefore become excellent solar absorbing materials, metallic micropyramids cannot provide optimal passive cooling purely as a function of geometry. Unlike nickel and other metals, the complex refractive index of most ceramic and polymer materials is significantly lower and does not follow the same increasing trend as the wavelength increases that conductive materials such as nickel demonstrate. Subsequently these materials are already well suited for absorption in particular wavelengths. By utilizing a similar combined effect between the complex refractive index and texture geometry we can enable the anti-reflective behavior observed in both the alumina[69] and PDMS textures shown in the results. For both alumina and PDMS, the absorption bands are situated in the MIR/IR portion of the spectrum, with low ($k \sim 0$) extinction coefficients in the VIS/NIR bands leading to near 100% transmission of VIS/NIR radiation from wavelengths below ~ 6 μm. The absorption bands in the IR – attributed to an increase in the extinction coefficient (k) – enable IR anti-reflective behavior to be induced by geometry and further enhance emission characteristics of these materials. While the reflection is already low for these materials, optimized texturing can reduce the reflectivity to a value near 0. This relation can be observed in Figure 6(e), where an optimized texture expands the emission properties of

alumina by making it emissive from 8 – 16 μm as a result of anti-reflective behavior. We validate the results shown in Figure 2-9

(e) utilizing both a MG approximation in conjunction with a characteristic matrix [63], [70] and Rigorous-Coupled Wave Analysis (RCWA)[71], [72] in Figure 2-12. The numerous assumptions in analytical and semi-analytical optical models limits their applicability across the geometric design space we present in this work. Classical, analytical, and semi-analytical models capture the anti-reflective behavior of micropryamid designs[23], [27], [63], [70]–[73], but to ensure accurate optical and thus thermal computations across the entire design space we rely on the proven accuracy of FDTD simulations[74].

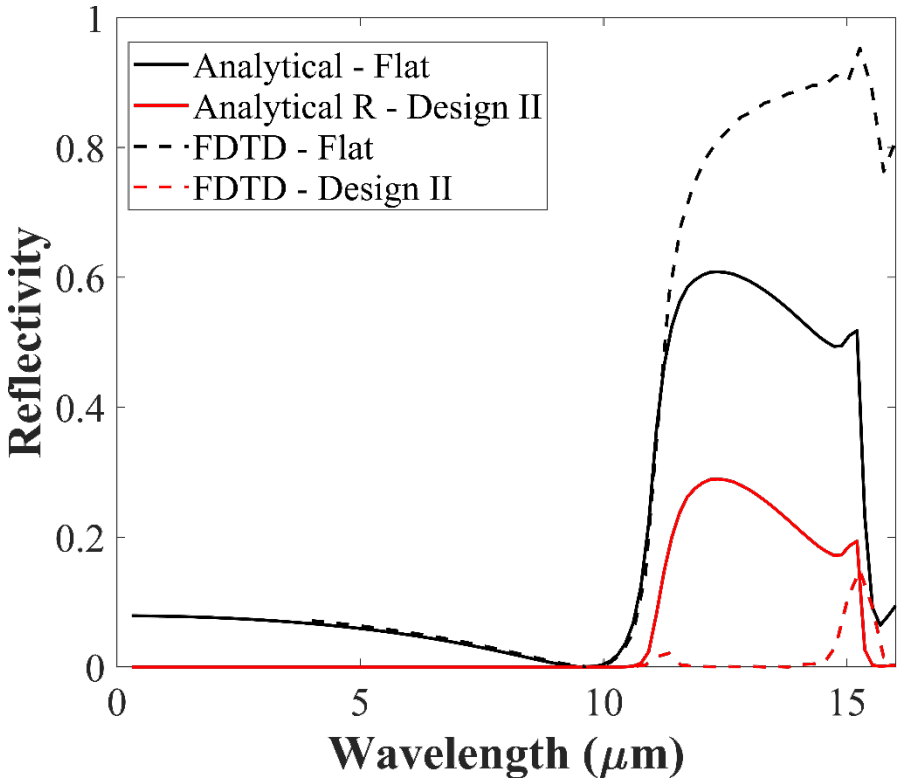

Figure 2-12 Reflectivity computed via the FDTD method and analytical method described using the characteristic matrix and EMT approximation. Design II (5 x 15 um) shows a significant reduction in reflection when compared to the flat case, and the analytical model mimics the peak location(s).

Fundamentally, the anti-reflective behavior of the alumina/PDMS textures is the same behavior observed in nickel, but the spectral region has shifted. A key difference between the polymer/ceramic optimization and the nickel optimization is the relation between the AR and x_{span}. Whereas Figure 3(a) makes it clear that the FOM of textured nickel depends strongly on AR as all of the x_{span} base dimensions demonstrate the same concave behavior with the inflection point near AR ~ 2 – 4, however, this behavior is not observed in alumina/PDMS. Figure 2-8(a) and Figure 2-10(a) show that the FOM instead behaves not only asymptotically, but that the asymptote is reached far more quickly as x_{span} increases. Additionally, Figure 2-8(a) makes it clear that increasing the aspect ratio does not have as significant of an effect on the optical properties when the base dimension is significantly smaller than the critical incident wavelengths where anti-reflective behavior is observed. Alumina and PDMS have similar behavior between AR and FOM, but the "most optimal" geometric combinations for either material occur in different regions of the contour plots of Figure 2-8(b) and Figure 2-10(b). PDMS is the most optimal when $x_{span} > 15$ μm, and alumina texturing is most optimal when $x_{span} \sim 7.5 – 10$ μm. Unlike nickel, which has a distinct observed optimality region highlighted in the dark-red region in Figure 2-5(b), the saturation of the IR-emissivity for alumina/PDMS makes it difficult to define a the boundaries of the optimal geometric region. While we expect that increasing the bounds of our optimization process from an x_{span}/z_{span} of 15 μm/20 μm respectively to much larger values would enable the definition of a distinct optimal combination region akin to the nickel results in Figure 2-5(b), the computational time is not deemed to be worth the potential < 0.1 - 1% increase in emissivity. Additionally, it should be noted that as a consequence of the asymptotic behavior between the cooling FOM and AR, the alumina/PDMS optimization

process very quickly yields highly optimal geometric solutions. For all the materials presented, while we can identify specific combinations of geometry that are most-optimal, we observe that local minimums in the cost-function can have significant variation in their aspect ratio despite marginal variation in the computed absorption/emission efficiencies. The optimality region that develops in the thermal cost function is a result of the overlap between material properties, incident wavelength, and geometry. In simulating micropyramids made of other materials, we expect this trend to continue and that a micropyramid with an aspect ratio from 2 – 4 that has a base dimension near the critical wavelength with an appropriate complex refractive index ratio compared to the surrounding medium will yield effective anti-reflective behavior.

The optimized geometries for the heating and cooling cases (nickel and alumina/PDMS respectively) have a significant impact on the thermal performance of each material. In a typical ambient environment, Nickels best computed geometry (x_{span} = 0.65 μm and z_{span} = 2.1 μm) has a surface temperature that is 44.2 °C higher than an untextured nickel surface. This demonstrates the heating applications of textured nickel, as the textured nickel surface absorbs over 98.6% – 982 W/m^2 – of the incident solar radiation from λ = 300 nm to 2500 nm while the untextured surface only absorbs 33.7%. For cooling applications, textured alumina emits an average of 170 W/m^2 compared to the 106 W/m^2 figure of untextured alumina (emission from λ = 8 to 14 μm) under typical ambient conditions. This

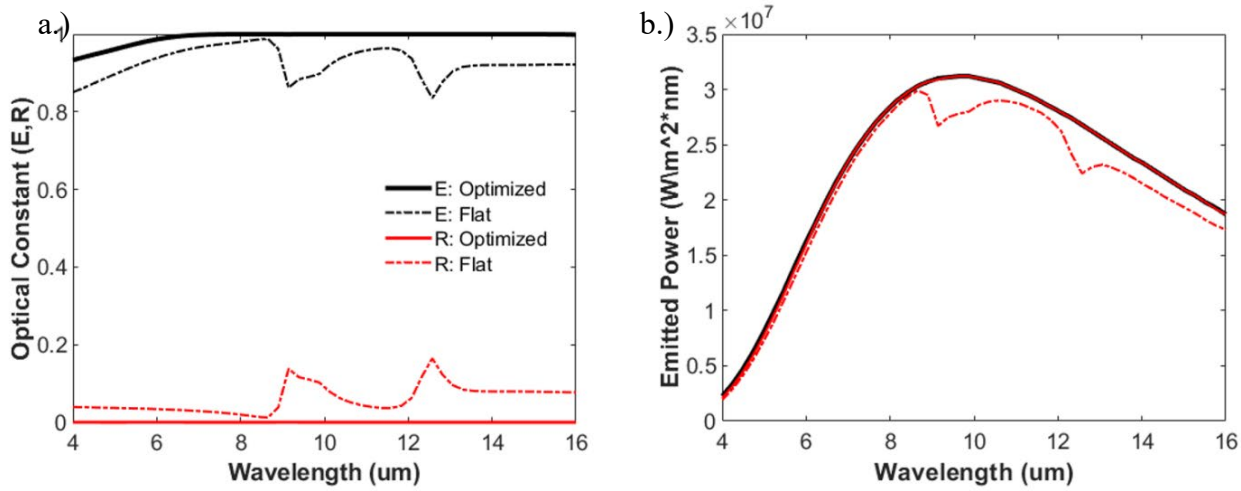

Figure 2-13 The emissivity and reflectivity of the flat/optimized PDMS surface. The effect of texture is to reduce the minimal amounts of reflection (R < 0.2) in the IR region to values near 0. **(b)** The reduction in reflection and maximization of emissivity results in the thermal emission being nearly identical to the ideal blackbody distribution and making PDMS a

nearly perfect emitter.

emission difference corresponds to a textured alumina surface temperature that is 9.8 °C below the ambient and a surface temperature of 6.1 °C below the ambient for the untextured case. Optimized PDMS geometry leads to the emission in the atmospheric transmission window of 8 – 14 μm increasing from 160 W/m^2 to 172.46 W/m^2 at a surface temperature of 300 K. While the 7.2% enhancement in textured PDMS's emission vs flat PDMS is not a significant as the geometrically induced absorption enhancement in nickel or emission increase in alumina (192.8% and 39.2% respectively) it is significant as it is only 0.007 W from the maximum blackbody emission from a surface at 300 K (over 99.99% of the theoretical limit). The emission spectra of the flat and textured PDMS relative to the blackbody limit is plotted in Figure 2-13.

2.7 Conclusion

Using a minimization algorithm in conjunction with finite-difference time domain simulations, we have demonstrated that we can quickly arrive at micropyramid geometric parameters that provide near-ideal solutions for thermal radiation and absorption. It has been shown how we can rapidly optimize a two-variable geometric optical pattern to selectively reduce spectral reflection in metal, ceramic, and polymer materials. Further, it has been shown that uncoated nickel periodic structures can research absorption efficiencies exceeding 98%, with the optimized design increasing emission from 337 W/m^2 (untextured) to 982 W/m^2. Simultaneously, the optimized nickel micropryamid design maintains a thermal emission that is below 20% of the maximum blackbody emission. By applying the same algorithmic process and geometry to both polymer and ceramic materials, it has been shown how these materials can be designed to be more efficient thermal emitters. We have seen geometries that significantly improve the cooling performance of Alumina and PDMS surfaces from their untextured values of 106 W/m^2 and 160 W/m^2 to 170 W/m^2 and 172.4 W/m^2 – respectively – when the texture is applied. The enhancement of the thermal absorption in nickel and thermal emission in alumina and PDMS are driven by localized resonance and field confinement by the surface, and we have specified design guidelines on how to maximize these effects for the given materials. This work not only establishes the design criteria for micropryamids in thermal design applications, but it also delivers an easy-to-use algorithm, set of heat-transfer metrics, and adaptable framework that can be applied to a wide variety of future simulations and geometries.

Chapter 3 – Deep Learning Based Micropyramid Analysis for Thermal Radiation Control

3.1 Deep Learning Introduction

The design and optimization of textures to control light – such as micropyramids – can be a challenge as simulating across the available design space is a computationally demanding process that often requires dedicated numerical simulation software[75]. To compound this problem, the vast array of available materials means that for a given set of application requirements and constraints there can be a different material that is best suited to fulfill those requirements. A powerful approach that has emerged in the field of nanophotonics is the use of Deep Learning (DL) and Deep-Neural Networks (DNNs) to fill the design space and to circumvent the necessity of large time investments in simulations. Inspired by the biology and architecture of the human brain, the DL methodology is capable of high levels of non-linear abstraction from datasets[76]. DL and Machine Learning (ML) have been used, in a broad setting, to solve complex problems ranging from machine vision for self-driving vehicles[77] to automatic speech recognition[78] and spacecraft system optimization[79]–[82]. In the field of optics, DL has been used recently to predict and model plasmonic behavior[76], [83]–[87], grating structures[53], [88], ceramic metasurfaces[89], [90], chiral materials[91], [92], particles and nanosturctures[55], [93], [94], and to do inverse design[55], [76], [86], [94]–[97]. Deep-Learning has also been used extensively in the field of heat transfer for applications such as predicting thermal conductivity[98], [99] and thermal boundary resistance[100], studying transport phenomena[101], optimizing integrated circuits[102], modelling boiling heat transfer[103], predicting thermal-optical properties[53], [104], [105], and addressing thermal radiation problems[106]–[109].

Spectrally selective surface designs are heavily dependent upon material selection. The interaction of light with a surface is a process regulated by the complex refractive index of the material(s) involved[63], [70], and material selection is fundamental to a microstructure's performance. Different material classes such as metals, ceramics, polymers, and dielectrics interact differently with light, and the influence of geometry and microstructure can vary significantly even for small changes in the constituent material's complex refractive index. A polymer, for example, has a strong mid-infrared response as a function of its complex refractive index, but due to the extinction coefficient of ~0 in the VIS-NIR, it is optically transparent. To manipulate the optical properties in those wavelengths, another material needs to be included in the polymer matrix[20], [110]. To provide a comprehensive thermal optimization, it is imperative that the designer can exhaustively search across a material catalog to find what material and geometry combination are best suited for the thermal design requirements.

In this chapter, a methodology based on a DNN to predict the optical properties of micropyramids across a wide design space of geometries, wavelengths, and, most importantly, materials is presented. As opposed to many other previous studies that provide a deep learning approach to a structure with a single material[83], [95], a geometry with fixed materials[53], [91], [94], or a material input defined by one-hot encoding with a random forest[55], the DNN method shown in this chapter is designed to predict the optical properties of a vast array of materials and is not constrained by material input. While there are many available machine learning methods[55], [87], [105], [111]–[115], the deep neural network approach is used due to the method's input flexibility, scalability, and the ability to extrapolate outputs from unseen inputs.

The model can predict the transmissivity, reflectivity, and emissivity of micropyramids across a diverse library of materials. It emulates finite-difference time-domain (FDTD) simulation outputs by predicting spectral properties for a combination of the plane-wave source wavelength, geometric properties of the texture, and material. Further, it differentiates materials by taking discrete material inputs derived from the complex refractive index and subsequently builds relationships between the material inputs and the geometry and wavelength to predict the transmissivity and reflectivity. From the predicted optical data, we make thermal predictions for the texture's thermal emission and absorption performance. For a given material, there is a vast optical property design space afforded by a microstructure. By using the network to search across a library of materials, the material and geometry combinations that best optimize a set of thermal conditions is provided. We can rapidly perform exhaustive searches across a material database and geometric design space to find optimum combinations, a process that would be too computationally expensive with previous micropyramid optimization approaches. While the methodology is applied to micropyramid structures, it has wide applicability for neural network designs that can replicate and effectively replace optical simulations for metasurface and microstructured surface optimization.

3.2 Deep Learning Method

Solutions using the FDTD method, while accurate, are time consuming. Optimizing the spectral properties of a microstructure can be a challenge due to the number of simulations required. We employ a deep neural network architecture that can estimate the simulation outcome to predict optical properties rapidly and accurately. We design a network that can predict across the geometric design space of a micropyramid for a given minimum and

maximum wavelength (λ_{min} and λ_{max})and is capable of modeling and predicting the behavior of micropyramids constructed of an array of materials. Once the model is trained, the prediction phase is nearly instantaneous. Thus, if the model's predictions are accurate, we can perform accurate optimizations in the span of seconds and mitigate the necessity of additional computationally expensive simulations.

3.2.1 Simulations

Our model is trained, validated, and tested on a dataset constructed of data compiled from 35,500 different simulations from Lumerical's commercially available 2D/3D FDTD solver. The simulation framework provides exact solutions for Maxwell's equations across a finite element mesh and we can extract the dispersion and absorption from the results[57], [58]. For this work, all simulations are calculated in 2D to minimize simulation time and generate large datasets for each material. 2D FDTD simulations deliver accurate results for micropyramid geometries, but slightly overestimate the emissivity when compared to a more realistic 3D simulation[116]. We chose to simulate our periodic micropyramid structures using FDTD instead of a semi-analytical approach such as RCWA[21], [44] due the accuracy of the FDTD method as well as the scalability and applicability of FDTD beyond the geometrically simple structures shown in this work. The simulations are based upon the geometry shown in Figure 3-1, with key independent geometric parameters: the triangle base span (x_{span}), height (z_{span}), and substrate thickness (t_{sub}). We utilize periodic boundary conditions for our simulations: the structure shown in Figure 1 occupies the entire unit cell. Additionally, as micropyramids have been shown to demonstrate omnidirectional optical properties[16], [24], [36], [116], we do not vary the source angle of incidence or polarization. For this work we assume that Kirchhoff's law is valid and the emissivity we calculate from

the simulations is derived from $\alpha = \varepsilon = 1 - R - T$, where reflectivity (R) and transmissivity (T) are calculated from power monitors above and below and domain respectively and where absorptivity (α) is synonymous with emissivity (ε). For each material, we generate a uniformly distributed random matrix of x_{span}, z_{span}, and t_{sub} variables and run the simulation with a plane-wave injection source that ranges from λ_{min} to λ_{max}. The size of the randomly generated geometric property matrix corresponds to the number of simulations, with the randomness generally ensuring that simulations in a dataset have a unique combination of the three geometric variables. While the x_{span} and z_{span} coordinates are randomly generated with values ranging from 0 – 10 um, the range of t_{sub} and λ_{min} to λ_{max} properties are selected based on the material.

3.2.2 Model Architecture

We use a deep neural network with fully connected dense layers as shown in Figure 3-1. Our deep learning approach is built upon the open source keras library in python[117]. The architecture of the neural network shown in Figure 3-1 is designed to emulate the critical simulation inputs that influence the computed optical properties. In total, our

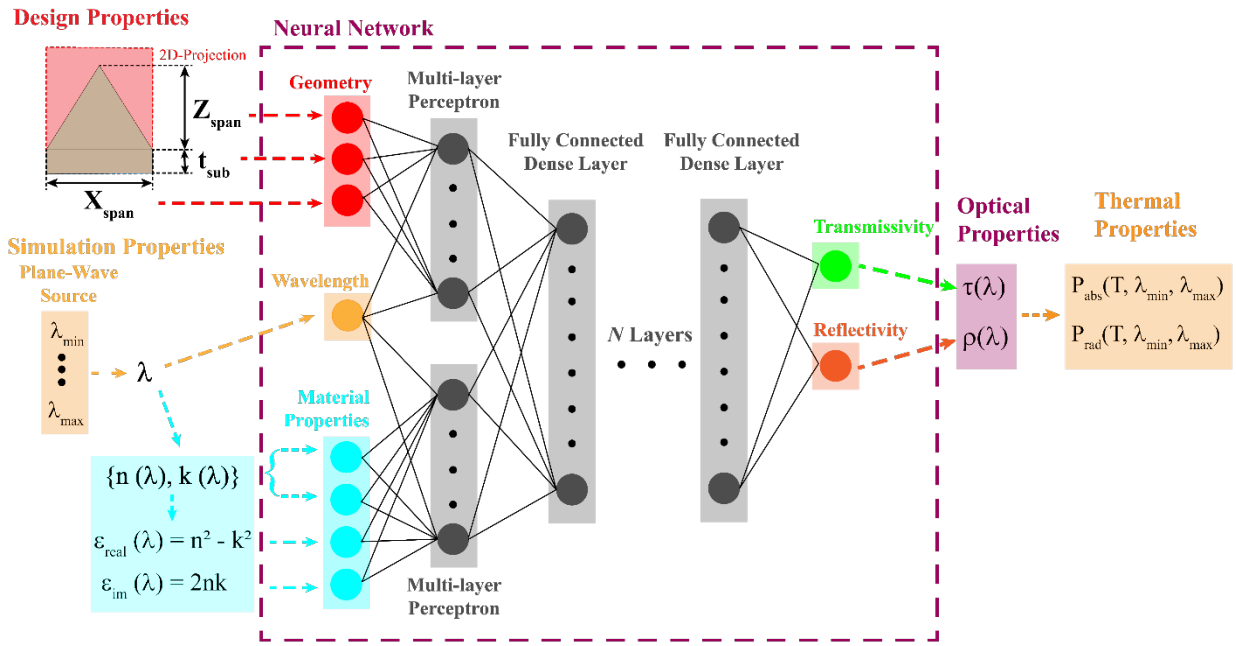

Figure 3-1 Visualization of Deep-Neural Network (DNN) construction and overall process flow. The geometric input parameters used in simulations and input into the DNN are the independent parameters x_{span}, z_{span}, t_{sub}. We assume periodic boundary conditions for a unit cell that contains a single micropyramid with the specified geometric parameters. We divide the wavelength spectrum used in simulation into a set of single inputs. Each wavelength point has a set of λ-dependent n, k, ε_{real}, and ε_{im}. The material properties are used as inputs to one multi-layer perceptron (MLP) and the geometric properties/wavelength are grouped as inputs for another MLP. The MLPs concatenate and connect to a larger DNN structure. The outputs of the DNN are a reflectivity and transmissivity point corresponding to λ.

network employs 8 inputs: x_{span}, z_{span}, $t_{sub,}$ λ, n, k, ε_{real}, $\varepsilon_{im.}$ These inputs follow three classifications: geometric parameters, wavelength, and material data. The geometric parameters are x_{span}, z_{span}, and thickness of the substrate under the surface texture (t_{sub}). We include the substrate thickness to capture the optical property behavior with respect to the thickness so that our model can more accurately interpret and predict the behavior of transmissive materials. The second input classification is the injection wavelength (λ). The wavelength is the fundamental determining factor that links the output and material data together. In a FDTD simulation, each frequency/wavelength point we solve at has a corresponding set of optical properties (ε, R, T) so to emulate that behavior we utilize a single wavelength point as a network input. The solution to Maxwell's equations is not sequentially dependent, meaning that we can separate a large, simulated wavelength spectrum into smaller groupings of inputs for the neural network. Previous network designs employed the full simulation wavelength spectra and the corresponding wavelength dependent material properties, but we found that dividing the full-spectrum simulations into single wavelength inputs yields much more accurate results.

Correspondingly, the FDTD method uses the complex refractive index to differentiate between materials. At each wavelength point of the solution, there is a matching refractive index value (n) and extinction coefficient (k). The third grouping of the neural network's input parameters – the material properties – enable the DNN to differentiate materials similar way to how a FDTD simulation would. To better strengthen the connection between material properties and the output, we include two correlated parameters – the real (ε_{real}) and imaginary permittivity (ε_{im}), shown in Figure 1. Compared to using only normalized n and k inputs to differentiate materials, the inclusion of the correlated parameters

strengthens the connections between the material input and the output optical properties, enabling higher prediction accuracy for materials not included in the training of the model. The output of the neural network is the reflectivity and transmissivity that correspond to the wavelength input and material/geometric properties. This design emulates the output of the power monitors used in the FDTD simulations. Predicting all three optical properties is unnecessary as – assuming Kirchhoff's law is applicable – we calculate the emissivity from the other two properties. To further enhance the connection between input and output, we utilize two smaller multi-layer perceptron (MLP) architectures that allow the model to build connections with the geometry/wavelength and wavelength/material properties respectively. The outputs from these MLPs are fed into the larger DNN structure. The uncoupled MLP structures are implemented to increase the connections between the inputs and to develop separate non-linear relationships between the key independent parameter (λ) and the geometric information and the material information. The concatenated output of the MLPs is fed as an input to the larger and fully connected sequential DNN structure. In our design process, we have found that this methodology has led to increased accuracy in extrapolating optical properties for new materials.

Gen	Inputs*	Input Neurons	Architecture	Normalization	Outputs	Type of Output**	Library Accuracy
1	7	304	DNN	Linear	200	E, R	0.105
2	7	304	DNN	**Linear/Log**	**200**	**R, T**	0.095
3	**6**	**6**	DNN	Linear/Log	2	R, T	0.068
4	**8**	**8**	DNN	Linear/Log	2	R, T	0.049
5	8	8	DNN	**Lin/Log/Quant**	2	R, T	0.032
6	8	8	**2 MLP + DNN**	Lin/Log/Quant	2	R, T	0.027

* Number of Inputs: 7 - (X, Z, AR, tsub, lambda, n, k)
6 - (X, Z, tsub, lambda, n, k)
8 - (X, Z, tsub, lambda, n, k, ereal, eim)
9 - 2 sets of inputs: (X, Z, tsub, lambda) and (lambda, n, k, ereal, eim)
** Output Type: Emissivity (E), Reflectivity (R), and Transmissivity (T)

Table 3-1 Comparison of successive model iterations, comparing the differences in model architecture, output type, input type, and ultimately the model's accuracy in predicting the library of materials. The final generation – the one shown in the paper – performs exceptionally well, predicting the optical properties of micropyramids constructed from materials not included in training with a high degree of accuracy. Changes from generation to generation are bolded. Scores are given as an MAE score (Eq.2)

The optimized DNN uses 8 fully connected dense layers with 400 neurons per layer, and both MLPs are 4 layers of 50 neurons each. Optimization of the hyperparameters is performed with the built-in hyperband optimization method[118]. Manual cross-fold validation for limited hyperparameter optimization is used to augment this. For training, the loss function is defined by the Mean-Squared Error (MSE) and validated/evaluated using a mean-absolute error (MAE) score based on equations 1 and 2 respectively, where Y_i is the predicted value.

$$MSE = \frac{1}{n}\sum_{i=2}^{n}\left(Y_i - \widehat{Y_i}\right)^2 \quad \text{(Eq.1)}$$

$$MAE = \frac{\sum_{i=1}^{n}|Y_i - \widehat{Y_i}|}{n} \quad \text{(Eq.2)}$$

Adam is the optimization engine used for the network training. To minimize overfitting, we utilize L2 regularization in the training and validation process, in addition to utilizing early stopping, checkpoint save, and reduce learning rate on plateau callbacks.

3.2.3 Datasets and Normalization

Several normalization methods are employed depending on the input type. X, Z, and λ are considered uniform, and a simple linear normalization is applied to each separately using Eq. 1. For the refractive index (n) we use a log-linear normalization, using Eq. 4 with α = 0 and then Eq. 3 to bring the values between 0 and 1.

$$x_{norm} = \frac{x - x_{min}}{x_{max} - x_{min}} \quad \text{(Eq.3)}$$

$$x_{norm} = \log_{10}(x + \alpha) \quad \text{(Eq.4)}$$

The distribution of k, t_{sub}, $\varepsilon_{real,}$ and ε_{im} pose a more significant normalization challenge. The ε_{real} permittivity value is of particular concern due to the negative values induced by $-k^2$. A fundamental problem faced is that optically, the difference between k = 1e-4 and 1e-3 is not mathematically large, but the difference does have a large impact on the transmission behavior through the substrate. Thus, the data is grouped near 0 but we need to differentiate values in a meaningful way to distinguish the physical behavior of each material. Log normalization reduces the severity of the weighted inputs but does not solve it. Thus, for these variables, we turn to more complex normalizations. For this work, we utilize quantile normalization with sklearn's built in quantile transformer, to generate a uniform

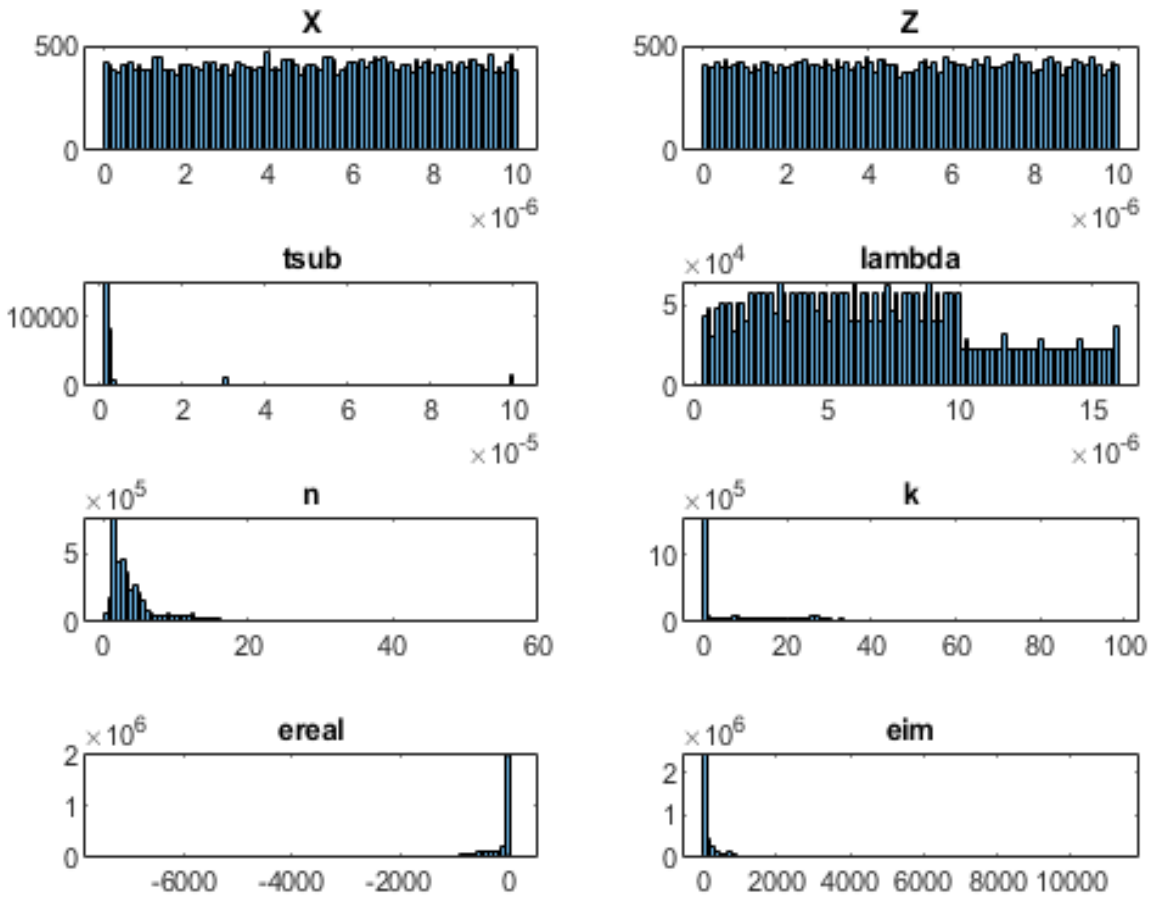

Figure 3-2 Distribution of the datasets before normalization. Although t_{sub} is generated randomly, due to the large number of metals, the primary distribution is near 1 – 5 um.

distribution of inputs for k, t_{sub}, ε_{real}, and ε_{im}. To ensure our values for all materials stay between 0 and 1 on all inputs, we normalize all the simulations together.

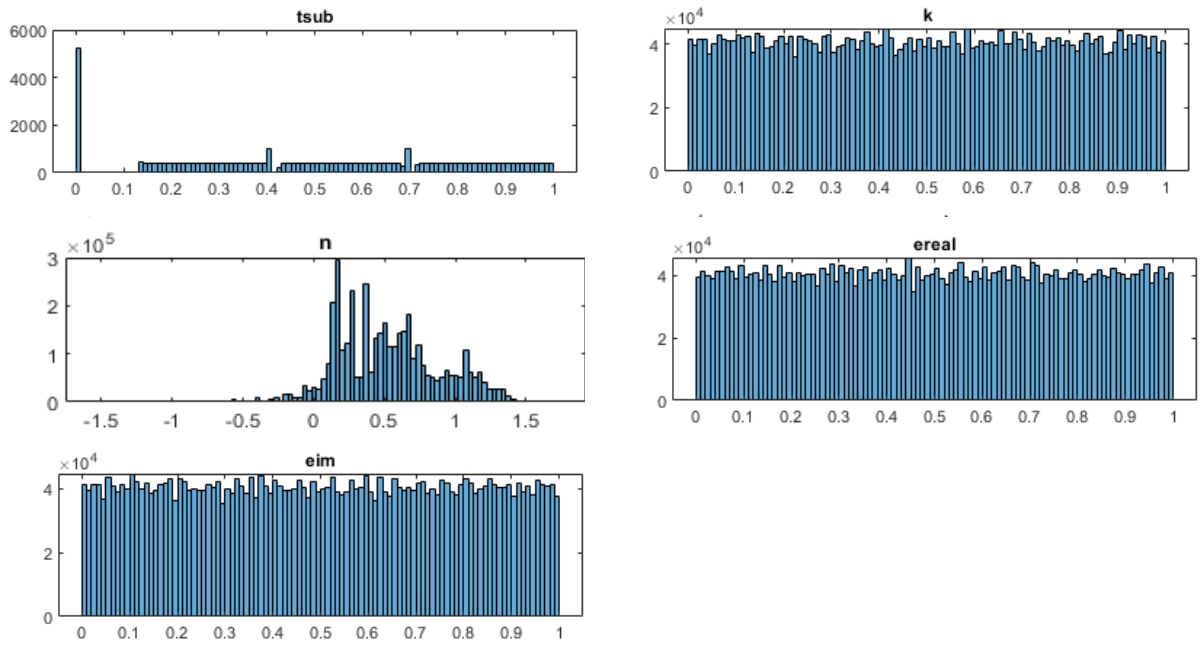

Figure 3-3 Datasets after normalization. tsub, k, ereal, and eim are all normalized using quantile normalization. To reduce complexity without sacrificing model accuracy, n is normalized using a simple log and then linear normalization method.

3.2.4 Model Training and Evaluation

The DNN is trained using the FDTD generated datasets and allow it to learn and predict the non-linear relationships between the input geometry, wavelength, material properties, and the output spectra. The simulation data is divided into three separate subgroups: training, validation, and testing, which carry a 70/20/10 split respectively. We use the training and validation data in the model generation process. The test dataset – unseen during training – is used to evaluate the performance and accuracy of the network in interpolating optical properties for new geometric and wavelength combinations. The training/test datasets encompass simulations from 14 different materials of widely varying complex refractive index, including metals (Ni/Ag/Al/Cr/Fe/Sn)[69], [119], [120],

refractory metals (Ta/W)[69], [121], a phase-change material (VO2 Metallic/Insulating)[122], a polymer (PDMS)[62], a semiconductor (SiC)[123], a ceramic (SiO2)[69], and a material with a near zero extinction coefficient across a wide spectrum (Diamond)[124]. The network predictions vs the simulation results for the test dataset are shown in Figure 3-2(a, b). The diverse set of materials enables the network to interpret a wide range of n and k inputs – including extreme values – during the training process. The values of the complex refractive index are plotted in Figure 3-3(c), to highlight the differences between the materials in the training/validation/test datasets.

The test dataset does not contain new material data, but it includes geometric combinations that the model has not seen in training. Our model demonstrates an ability to predict with an extreme accuracy new geometric/wavelength combinations made of materials included in the training process. The error between the prediction and simulation values is plotted in Figure 2(a) and broken down by material in Figure 3-3(b). The mean absolute error (MAE) for the training and validation sets are 0.0034 and 0.0035 respectively. These error values correspond to an MSE error for the training/validation datasets of 1.22e-4 and 1.34e-4 respectively. The test dataset has an MAE and MSE error of 0.0034 and 1.53e-4 respectively. While some outlier predictions do exist, as visualized in Figure 3-3(a), the error by material in Figure 2(b) validates that our model is interpolating the optical properties for "seen" materials with high efficacy. An apparent relationship from Figure 3-3(b) is that transmissive materials show a larger error in the predicted transmission, and metallic materials show an increased error in reflection. This is a manifestation of the role of the extinction coefficient, with a high extinction coefficient leading to reflection dominated optical properties and low extinction coefficient leading to transmission dominated optical

properties. For some materials with a low extinction coefficient (k << 1), geometry has little to no influence on the reflection and t_{sub} is the only geometric parameter that determines the optical properties. This relationship necessitates that the design of the network correctly connects the material properties, wavelength, and geometry, to make accurate predictions for any arbitrary material not included in training.

The small differences in error between the test/evaluation datasets and the training/validation training errors verify the network can predict the optical properties for inputs within the design limits with a high degree of accuracy. Additionally, the minimal difference in error between the test and training/validation datasets allows us to conclude with a high degree of certainty that the model is not overfitting during training.

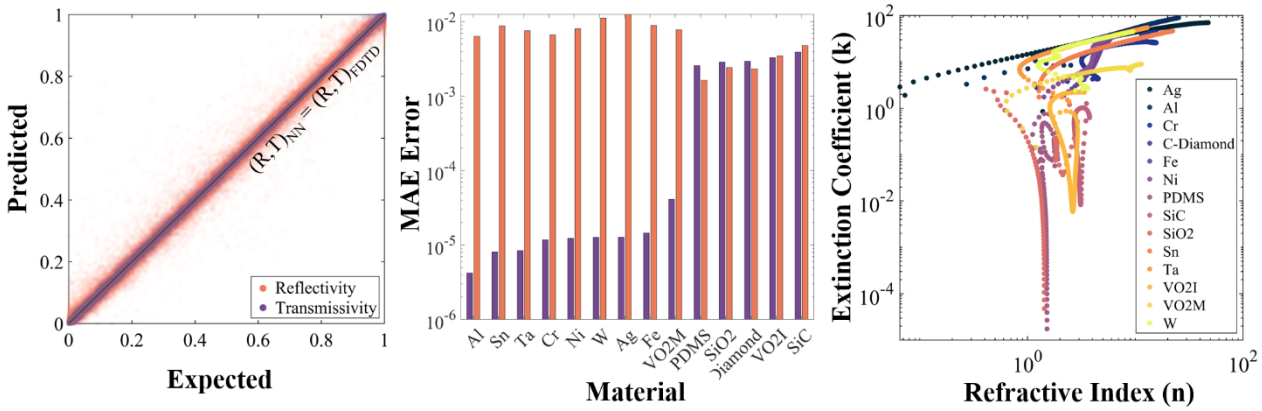

Figure 3-4 (a) neural network predictions of the optical properties compared to the properties obtained from FDTD simulations plotted for the test dataset. (b) By material average mean absolute error (MAE) for reflectivity (orange) and transmissivity (blue) separately for the test dataset. No error exceeds 0.01, the overall test dataset has an MAE of 0.0034. (c) The extinction coefficient (k) vs the refractive index (n) for all of the materials included in the test dataset, highlighting the differences between the materials used in the training of the network.

3.2.5 Thermal Optimization

While we can choose to define thermal optimization equation for specific applications such as radiative cooling or heating, high temperature cooling, etc., for this work we use a simple relation for easy comparison in the unseen material predictions. The cost function used in this work neglects solar absorption and focuses only on maximizing thermal emission. We define the objective function with the heat transfer balance,

$$C_{cooling} = \frac{P_{max,rad} - P_{rad} + P_{abs} + P_{trans}}{P_{max,rad} + P_{solar}} \quad \text{(Eq. 5)}$$

$$C_{cooling} = \frac{\int_{\lambda_{min}}^{\lambda_{max}} I_{BB}(\lambda,T)d\lambda - \varepsilon(\lambda)(\int_{\lambda_{min}}^{\lambda_{max}} I_{BB}(\lambda,T)d\lambda + \int_{\lambda_{min}}^{\lambda_{max}} I_{AM1.5}(\lambda)d\lambda) + T(\lambda)\int_{\lambda_{min}}^{\lambda_{max}} I_{AM1.5}(\lambda)d\lambda}{\int_{\lambda_{min}}^{\lambda_{max}} I_{BB}(\lambda)d\lambda + \int_{\lambda_{min}}^{\lambda_{max}} I_{AM1.5}(\lambda)d\lambda} \quad \text{(Eq. 6)}$$

Where $P_{max,rad}$ is the maximum amount of blackbody radiation that can be emitted by the surface, P_{rad} is the emitted radiation, P_{abs} is the amount of absorbed solar radiation, P_{trans} is the amount of transmitted power through the surface, and P_{solar} is the amount of power available to absorb from the sun. P_{abs} and P_{trans} cannot be larger than P_{solar}, as defined by the integrals in Eq, 4. We do not include the effects of atmospheric emission in the heat balance equation to maintain a simple relationship between the maximum emission and achieved emission by the surface in the optimization process. The heat transfer equation shown in Eq. (5) is a cost-function equation that prioritizes cooling performance when subjected to solar radiation. Preferentially, the surface should reflect all incident radiation while maximizing thermal emission. As we are only considering a single material system, we include a term that accounts for transmitted power. Some materials (such as PDMS or SiO2) are good emitters but would allow solar radiation to pass through, leading to deceptive performance

unless a term that accounts for transmission is included. In our search process utilizing these equations, we are attempting to minimize the cost function.

3.3 Optical Predictions for Select Materials Unseen in Training

The network's input design – with distinct material inputs, wavelength, and geometric parameters – enable our network to dynamically predict the optical spectra of micropyramids made of materials that are not included in the training process. We first test our network's capacity to predict the optical properties of new materials with two new datasets: a metal (Titanium)[69] and a ceramic (Alumina, Al_2O_3)[125] dataset comprised of 1500 simulations each. These materials are not used in the training or validation process, and they were explicitly chosen as Ti/Al_2O_3's complex refractive index values significantly differ from the materials used in training. Comparisons of the refractive indices used in training to those predict the titanium and alumina datasets are shown in the supplementary materials. These datasets were generated with the same methodology as before and each simulation has a unique combination of t_{sub}, x_{span}, and z_{span}. After making predictions with a trained neural network that does not include any Titanium or Alumina data in training, we generate a different model that includes 10 randomly selected simulations from the alumina and titanium datasets (<1% of the simulations) to compare the prediction accuracy when a small amount of data is included in the training process.

Figure 3-5(a,b) plots the predicted optical properties by FDTD simulation vs the neural network predictions. The MAE between prediction and simulation for the alumina and titanium datasets are 0.0175 and 0.0131 respectively. Broken down by individual output, the $MAE_{Reflectivity}$ is (0.026, 0.0063) and $MAE_{Tranmissivity}$ is (6.01e-5, 0.028) for titanium

and alumina respectively. The error in the reflectivity and transmission mirrors the results in Figure 3-4(b) – metallic materials have reflection driven optical properties with geometry and show a very low error in transmission. Conversely, the relationship between the substrate thickness and extinction coefficient of alumina leads to non-zero transmission, with geometry playing a reduced role in determining the reflection and transmission properties. In Figure 3-5(c,d) we compare the absolute difference between the neural network and FDTD predicted emissivity for the alumina and titanium datasets. Across both the geometric and wavelength space, we observe a high degree of accuracy in the neural network predictions. The exception to this is a significant deviation in the titanium dataset (Figure 3(d)) that occurs in a region with high material/geometry specific resonance. Similarly, the network minorly underpredicts the role of transmission in Al_2O_3, leading to the observed prediction differences. Despite these differences, the model is clearly able to differentiate material in a meaningful way and extrapolate accurately beyond the dataset used in training.

To improve the prediction accuracy, we examine what occurs when we include a seemingly trivial amount of simulation data from the "unseen" materials in the training process. We select 10 simulations at random from the Ti and Al2O3 datasets (<1%) and include them in the training/validation/test datasets. Figure 3(a,b) and Figure 3(e,f) underscore that the small inclusion of data has a large impact on the prediction accuracy. The overall MAE score becomes (0.0073, 0.0049) while $MAE_{Reflectivity}$ improves to (0.014, 0.004) and $MAE_{Tranmissivity}$ improves to (7.69e-5, 0.0058) for titanium and alumina when 10 simulations of each are included in the training dataset. These error values are close to those shown in Figure 2(b) for the materials in the test dataset, indicating that only a small amount

of simulation data is required to calibrate the model for a new material. Figure 3-5(e,f) demonstrates that even this small amount of data – while not enough to completely remove error – effectively reduces prediction error throughout, even in the highly erroneous resonant region of Ti. While the prediction error from completely unseen data is excellent, including a small number of simulations align the accuracy of the "unseen" materials with the accuracy of the much larger datasets included in training.

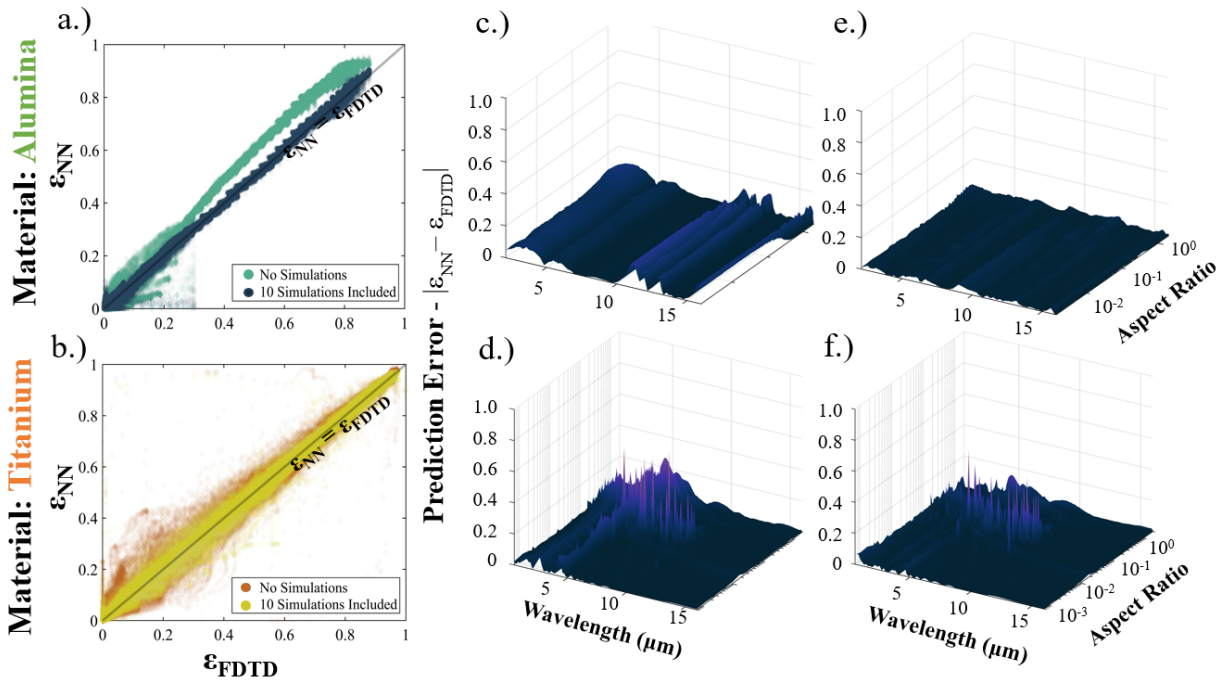

Figure 3-5 Neural-network predictions for two materials (Ti/Al2O3) that are not used in the in the training process**.** (a, b) The predicted optical properties vs. the FDTD computed properties, with and without 10 simulations included in training for alumina and titanium. Surface plot of the absolute error between prediction and simulation with no simulations included (c, d) and with simulations included in training. The wavelength is on the x-axis and the geometric information is visualized with the aspect ratio on the y-axis. Including 10 simulations (1% of the dataset) dramatically reduces the error in the alumina to a near zero value across all wavelengths and aspect ratios. For Ti, the resonance driven peaks in the low-aspect ratio structures are reduced and the error in all other sections becomes approximately zero.

3.4 Optical Predictions for a Library of materials Unseen in Training

To further demonstrate the capability of our model to provide accurate optical predictions for microstructures made of materials outside of the scope of the model's training, we compare the network's predictions to simulation results for 23 additional materials that were not seen in the training process. As many of these materials require much more time to simulate each geometric combination, we only perform 100 simulations for each material, for a total of 2300 additional simulations. The materials included in this library range

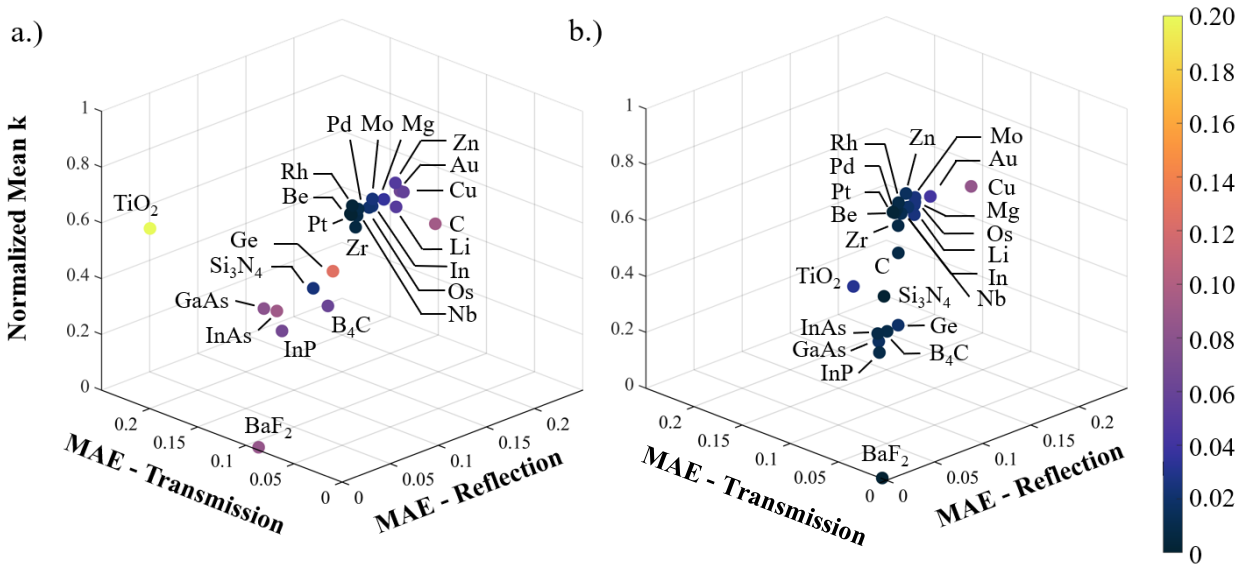

Figure 3-6 MAE for the transmission and reflection predictions compared to FDTD simulations for the 23 unseen library materials. (a) Plotted error when the materials are completely "unseen" and (b) after 5 simulations for each material are included in the training/testing/validation process. The log and then linearly normalized average extinction coefficient is shown in the z-axis, pointing to the role of the material in predicting where the error will occur. The error's (x,y) distance from an MAE error of zero is shown with the color bar. Including 5 simulations systematically reduces the prediction error for the rest of the dataset, indicating that very little data is needed to calibrate the model for new materials and lead to accurate predictions.

dramatically in material properties, with the complete material list and compilation of prediction accuracy shown in Table 3-2.

	MAE Reflection		MAE Transmission		Error Difference	
Material	No Simulations	5 Simulations	No Simulations	5 Simulations	ΔR	ΔT
Au[126]	0.0637	0.0456	2.63E-05	3.88E-05	-0.018	1.25E-05
B_4C[127]	0.0394	0.0098	0.0542	0.0091	-0.030	-0.045
BaF_2[128]	0.0040	0.0009	0.0907	0.0053	-0.003	-0.085
Be[129]	0.0086	0.0067	5.01E-06	3.72E-06	-0.002	-1.29E-06
C[130]	0.0972	0.0124	3.11E-04	3.12E-05	-0.085	-2.80E-04
Cu[69]	0.0709	0.0880	1.07E-02	1.80E-05	0.017	-0.011
GaAs[69]	0.0249	0.0106	0.0927	0.0186	-0.014	-0.074
Ge[69]	0.0869	0.0216	0.0964	0.0094	-0.065	-0.087
In[131]	0.0312	0.0223	6.95E-06	4.30E-06	-0.009	-2.65E-06
InAs[132]	0.0036	0.0030	0.0849	0.0121	-0.001	-0.073
InP[132]	0.0098	0.0053	0.0722	0.0126	-0.005	-0.060
Li[133]	0.0570	0.0297	8.23E-04	8.21E-04	-0.027	-2.04E-06
Mg[134]	0.0434	0.0295	5.84E-06	4.14E-06	-0.014	-1.69E-06
Mo[121]	0.0316	0.0296	7.39E-06	5.04E-06	-0.002	-2.35E-06
Nb[135]	0.0156	0.0154	4.55E-06	3.13E-06	0.000	-1.42E-06
Os[136]	0.0282	0.0291	1.21E-04	1.20E-04	0.001	-1.70E-06
Pd[129]	0.0168	0.0109	1.48E-05	1.02E-05	-0.006	-4.56E-06
Pt[69]	0.0096	0.0086	5.49E-06	4.32E-06	-0.001	-1.17E-06
Rh[69]	0.0106	0.0125	8.07E-06	6.89E-06	0.002	-1.18E-06
Si_3N_4[125]	0.0021	0.0021	0.0321	0.0046	0.000	-0.028
TiO_2	0.0006	0.0016	0.2003	0.0359	0.001	-0.164
Zn[128]	0.0554	0.0203	1.77E-05	1.34E-05	-0.035	-4.31E-06
Zr[128]	0.0141	0.0122	3.21E-05	2.17E-05	-0.002	-1.04E-05

Table 3-2 MAE Errors in the reflection and transmission without no simulations included in the training data and 5 simulations included in training. The relative error for each material is shown, with nearly all materials showing a significant decrease in error as a result of the small amount of data being included.

The error between the predicted optical properties and simulated optical properties for the unseen material library is plotted in Figure 4(a), with the errors shown in more detail in Table 1. The only material with an MAE > 0.1 is TiO2, with a transmission prediction error of 0.2003. Low extinction coefficient materials generally exhibit more error in transmission and high extinction coefficient materials exhibit a larger error in reflection. The results indicate that while the neural network does not perfectly replicate the physics of the FDTD simulations, it is nevertheless accurate in making predictions for materials that vary significantly from those used in training– the overall mean average error across all 23 materials is 0.0279.

We can improve this accuracy and calibrate the model by including a small number of simulations in the training/validation/test datasets. Here, we choose 5 random simulations from each of the 100 to include in the training/validation/test datasets. After training the model on this data, we show the improvement to the predictions in Figure 4(b). Despite using only 5% of the simulations contained in these materials' datasets, the small calibration data has removed much of the error on every material. The combined MAE score after 5 simulations are included in the training process is 0.0118. The increase in accuracy provides further validation that our model has connected the inputs to the outputs via the simulation physics well enough that it only requires a small amount of calibration data to produce extremely accurate results across the rest of a material's latent design space.

3.5 Material Selection Algorithm and Thermal Optimization

The strength of the neural network architecture is applied to make large-scale optical predictions for a library of materials. The resulting optical predictions from the neural

network are used to perform thermal optimization and search for the material and geometry that best optimize the selected thermal conditions. In total, 41 materials are passed into the trained neural network. The materials cross a wide spectrum and include all the materials that were included in training, titanium/alumina, and the 23 other materials that are unseen by the network during training.

To fully demonstrate the speed of the network and how comprehensive it can be in searching the latent design space, a grid of coordinates (xspan, zspan) is generated that spans from 0 to 10 um across both axes in increments of 0.1 um, for a total of 10,000 geometric coordinate pairs for each material. Over all 41 materials, this correlates to a total input of outputs of 410,000 optical simulations. For each of these simulations, there are 100 wavelength points, for a total of 41 million sets of inputs to the network. The network requires approximately 25 – 40 seconds to predict the optical properties across all 1,000,000 synthetic simulation input sets for each material. In total, the network requires 15 – 20 minutes to make predictions for all 41 materials. Each individual DNN approximated simulation requires anywhere from 30 - 40 microseconds on our computer. The output encompasses a total of 82 million datapoints for all 41 materials. The remarkable speed of prediction punctuates our desire to use a neural network to mostly supplant FDTD simulations, as the trained network can comprehensively predict a library of materials' optical spectrums in minutes.

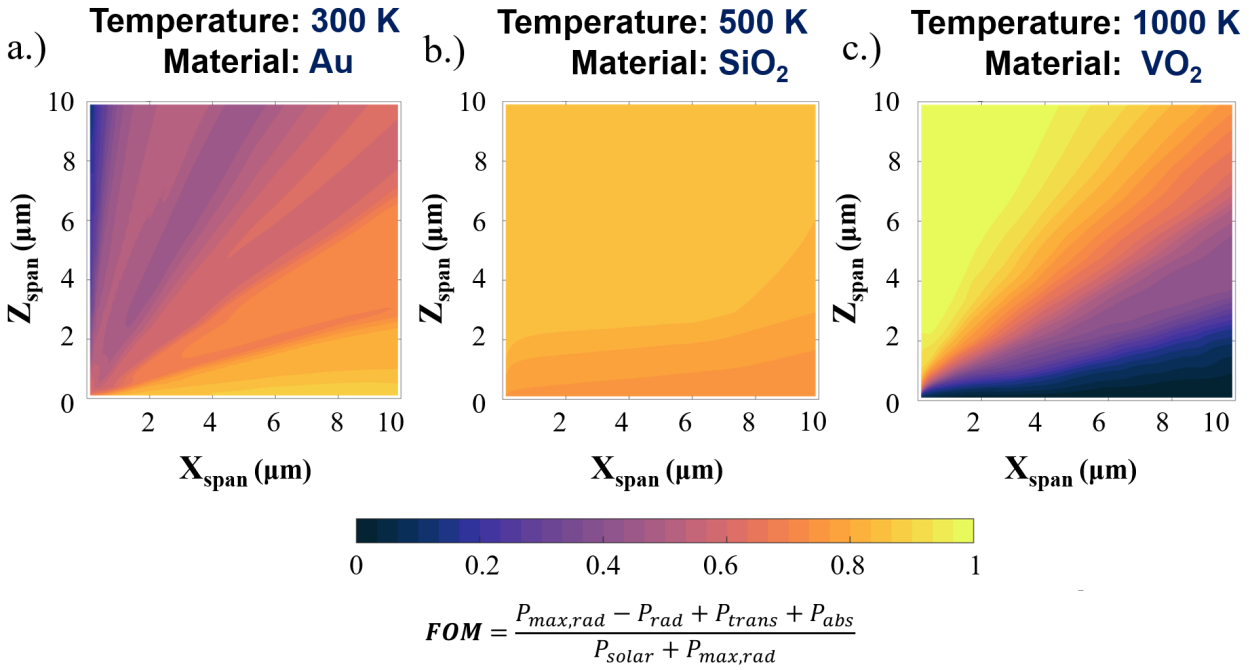

Figure 3-7 Material search algorithm identifying the most optimal microstructures for cooling at surface temperatures of 300, 500, and 1000 K based on the figure of merit defined by Eq. 5 - 6. Due to the role of transmission in Eq. 5, the most optimum microstructure for cooling at room temperature is Au (FOM = 0.772) as typical cooling materials such as PDMS and SiO_2 transmit thermal radiation in the visible wavelengths, negating cooling for a surface below. At 500 K, we identify SiO2 micropyramids as being most optimal (FOM = 0.852). At 1000 K, the algorithm identifies VO_2 as best performing micropyramid structure (FOM = 0.982) among all 41 materials that were predicted by the network. All materials are predicted assuming a minimum wavelength of 0.3 and maximum wavelength of 16 um to capture both thermal emission and solar absorption optical properties.

Temperature	Material	FOM	X_{span} (μm)	Z_{span} (μm)
300	Au	0.772	7.141	0.304
500	SiO_2	0.852	1.415	5.555
1000	VO_2	0.982	0.203	9.293

Table 3-3 Identified optimal material(s) and geometries that maximize the cooling figure of merit equation Eq.5.

The DNN spectral predictions are then used to perform a material search process to identify what materials and geometries best optimize a set of imposed thermal optimization equations. The selection of the thermal optimization equation is application specific. For the sake of demonstration, the optimization is for high-temperature cooling. The thermal optimization equations are processed for each wavelength dependent spectral property matrix to generate a figure of merit (FOM), a task that requires a significantly larger amount of computational time than the neural network's optical predictions. Figure 3-7 shows the materials and Table 3-3 shows the geometries identified by the search process that best optimizes the cooling thermal balance defined by Eq. 2-3 at three different surface temperatures: 300, 500, and 1000 K. The definition of Eqn. 5 leads to Au being the most optimal material for a single material cooling microstructure at 300 K, a result that hinges upon the role of transmission in the equation. Despite being a transmissive material, SiO2 is identified by the search algorithm as the most optimal material at 500 K. This as a result of a balance of the transmission of solar radiation with the large thermal emission at that temperature. It should be noted that the material data inputs into the network were not changed to account for temperature variation. The design of the network material inputs

allows the user to adapt the material data for different temperatures if a significant difference in the material properties is expected.

The ability to generate hundreds of thousands of simulations synthetically in seconds also means we can perform comprehensive optimizations that would not be possible previously. We can set constraints on the data generated and then subsequently search the entire set of generated optical properties within the confines of the set constraints. An example of previously unrealistic optimization that is now possible via our neural network

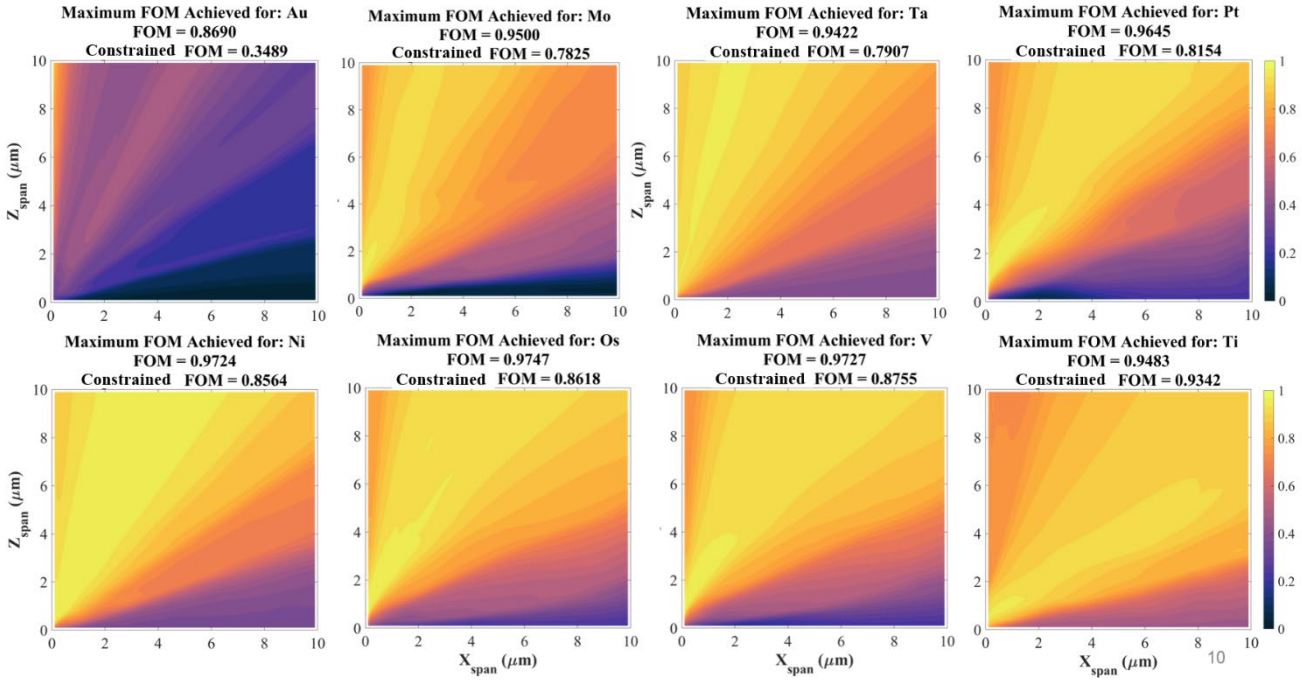

Figure 3-8 Thermal prediction plots generated using the heating figure of merit shown in Figure 8 for titanium and discussed in the methods section. The predictions are done using the 10,000 synthetic simulation reflectivity/transmissivity predictions done by the neural network. This process identifies titanium has having the best radiative heating performance across all materials when the aspect ratio of the structure is constrained to < 0.85, with a value of 0.934. This is compared to Os/Ni which are identified as two of the best heating materials when aspect ratio is not constrained, at 0.975/0.972 respectively. When their aspect ratios constrained to a value less than 0.85, they demonstrate a substantially lower maximum figure of merit.

is in the identification of optimal geometries that fall under a particular aspect ratio. The scalable methodology used to fabricate the base silicon molds has a process limited aspect ratio of ~ 0.8, so being able to identify not only what geometry but also what material leads to the best thermal result across all the materials simulated and within that constraint would not have been possible previously. In Figure 3-9, we demonstrate the identification of the best constrained geometries based on the heating figure of merit shown in Chapter 2.

This process enables us to provide thermal optimizations for a wide array of solutions to complex thermal problems. An often-studied application of micropyramids is for high-

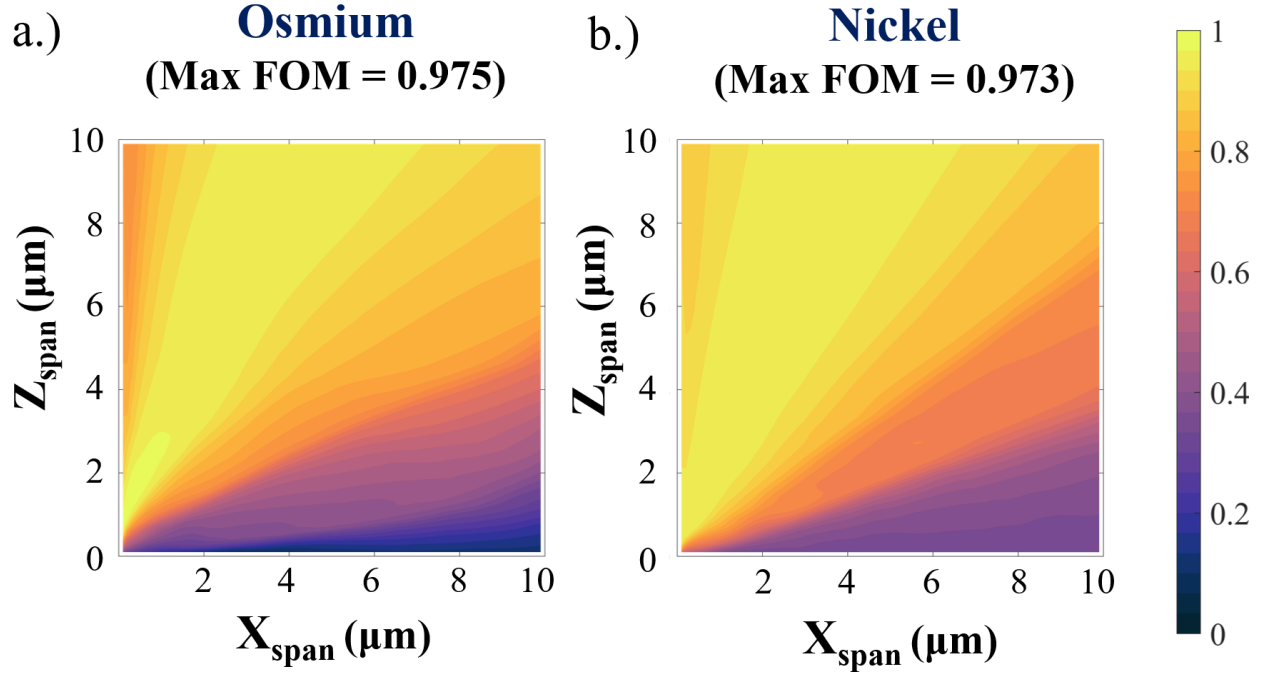

Figure 3-9 Identifying the micropyramid material that best optimizes the heating figure of merit (Eq. 4) at a surface temperature of 300 K. The predictions made by the neural network for the geometric grid (10,000 simulations per material) were used as the basis of the wavelength dependent emissivity in Eq. 5. (a) Our network emulated optical data projects that Osmium micropyramids would be the most optimal material for radiative heating. (b) Nickel, a common engineering material that is often used for micropyramids in previous work, is projected to perform nearly as well as Osmium.

temperature heating or radiative heating applications. Nickel – a highly mechanically and optically versatile metal – is a key area of research focus. Using the neural network, we can generate optical solutions for many metals and compare them to one another for a radiative heating application, in particular to see how nickel performs compared to other metals. We find that nickel – among the materials that we have selected to study – is a top-performing metal, suggesting that it is likely one of the best suited metals for radiative heating applications. The neural network assessment validates the earlier evaluation of Nickel as a prime candidate for radiative heating in Chapter 2.

3.6 Discussion

In contrast to FDTD simulations, which can take anywhere from minutes to hours to run, each DNN prediction takes approximately 30—40 μs/input to predict the spectra of a geometry/material/wavelength combination. Comparatively, we estimate simulating the same 10,000 parametric grid of geometries would require on average 1 – 3 months for the solutions to compute in FDTD via our simulation computers for each material. Accordingly, the neural network approach is approximated to be 6 - 8 orders of magnitude faster than traditional simulation methodologies. This estimation changes based on the available computational resources, but a tremendous benefit to a neural network driven approach is that an already trained model requires a miniscule quantity of resources to operate and make predictions. Our methodology is also scalable beyond the 2D micropyramid simulations we used in this work. We utilized 2D simulations such that we could more rapidly generate large training datasets, but our approach can be easily applied to replace or significantly reduce the reliance on simulations of more complex geometries or designs of other microstructures to increase throughput by orders of magnitude.

While our approach cannot completely replace simulations, we dramatically reduce the necessity of computationally expensive optical simulations. The use of material information and wavelength enables the model to build connections between the inputs and the physics, providing accurate predictions for a wide variety of materials that are highly dissimilar from those used in training the model. The model we show can be used to make generally accurate predictions for a material, with an overall MAE of 0.0279 for the library of completely unseen materials. Despite this accuracy, we can make more confident predictions by including a small amount of calibration data from simulations to tune the model to new physics, resonant behavior, etc., that may be present in the new material as a function of material properties or geometry. Including merely 5 simulations in training (500 datapoints) reduces our error on the remainder of the dataset to 0.0118. This indicates that our model is not merely interpolating existing material/geometry results and is making reliable predictions for materials that vary dramatically from those used to train the network.

The speed of the network combined with the ability to predict materials unused in training facilitates explorations of the design space in ways that would be impossible with traditional simulations. Figure 5 shows several specific instances of material and or geometry combinations that suit several generalized thermal balance equations, but there are near limitless combinations of temperature and environmental conditions. Our methodology allows for us to define a set of thermal conditions and search hundreds of thousands of material/geometry combinations in seconds to determine which combination yields the best result.

The network can perform thermal optimization in minutes – a task that would take years to generate a similarly sized dataset to search through using FDTD. The capability to explore the comprehensive material and geometric latent space of our problem empowers us to solve complex problems both rapidly and comprehensively. An example of this is using the network to identify optimal fabrication designs within particular constraints: for example, if the aspect ratio needs to be limited, we can identify in seconds both the material and geometric combination that provide the best expected results under the constraints. The network can also be utilized to quantify expected fabrication and experimental uncertainty by exploring the effects of nanoscale changes in the geometric parameters on the optical properties.

Ultimately, a fundamental problem facing surrogate models is the diminishing returns: to provide accurate results, more data is required, to the point where the design space has been thoroughly explored to generate the neural network model. The test dataset exemplifies this. While we can still explore minutia and small variations in geometry, a large amount of computational time was invested in generating the combined training dataset, to the point where the necessity of the neural network is diminished for these materials. Where our network is different from others that merely interpolate geometric or existing results is in the prediction of materials that have drastically different relationships between the incident wavelength, material properties, and geometry. We desire a network that can accurately extrapolate optical properties from any input material, without needing distinct and/or limiting classification methods or a large amount of new data. A particular challenge in developing the model to this end was overcoming errors in the prediction of transmissive materials. Whereas the reflection is primarily a material/geometry dependent phenomenon,

transmission depends on more parameters. The inclusion of separate MLP's, the permittivity inputs, and different normalization methods were all designed to improve the prediction accuracy of the model for both reflective and transmissive materials, ultimately improving the model's connection to the relevant physics.

The ability of the model to take different material inputs and predict outside of its original training scope – not bound to classification – unlocks many possibilities. This includes predicting optical changes at different temperatures, enabling much more complex temperature dependent optimizations. While we do not demonstrate a reversible network in this work, the network shown could also serve as a basis for a reverse-network structure. Multiple problems – such as multiple material solutions for the same desired optical output – will need to be overcome to implement a successful reverse network capable of predicting across a wide array of materials. These insights will inform the next generation of models that move to more complex microstructures with more material, geometric, and thermal parameters.

3.7 Conclusion

We have demonstrated a Deep-Neural Network that can emulate finite difference time domain simulation outputs that can be used for the rapid thermal and optical optimization of microstructured surfaces. The network can make accurate predictions for micropyramids across a wide array of materials and can accurately extrapolate optical properties from input data that is outside of the scope of training. Further, the network design allows us to accommodate and train on any number of materials and allows us to make predictions for the optical properties of micropyramids made of materials the model has not been trained

on. We have demonstrated how our model can be used as the basis for a material search algorithm that can identify materials and geometries that best optimize a thermal environment and set of constraints. The neural network driven predictions occur at a rate 6 - 8 orders of magnitude faster than the simulations that were used to train the model. The network predicts the optical spectra of over 1 million simulations per minute regardless of material choice, generating output datasets in seconds that would take years to simulate in FDTD. The material search process demonstrated in this work can identify the optimal material/geometry combination across a vast latent space nearly instantaneously. Furthermore, the methodology can be easily translated to other geometries beyond micropyramids, enabling DL based models that can significantly reduce the need for computationally expensive simulations for a variety of microstructure surface textures. Our methodology effectively replaces FDTD simulations for micropyramids, decreases the time required to optimize surface conditions, and allows for more complex and comprehensive studies to explore the latent space of the problem.

Chapter 4 – Image Based Deep Learning Surrogate Method

4.1 Introduction

The design and optimization of textures to control light – such as micropyramids – can be a challenge as simulating across the available design space is a computationally demanding process that often requires dedicated numerical simulation software[75]. To compound this problem, the vast array of available materials means that for a given set of application requirements and constraints there can be a different material that is best suited to fulfill those requirements. A powerful approach that has emerged in the field of nanophotonics is the use of Deep Learning (DL) and Deep-Neural Networks (DNNs) to fill the design space and to circumvent the necessity of large time investments in simulations. Inspired by the biology and architecture of the human brain, the DL methodology is capable of high levels of non-linear abstraction from datasets[76]. DL and Machine Learning (ML) have been used, in a broad setting, to solve complex problems ranging from machine vision for self-driving vehicles[77] to automatic speech recognition[78] and spacecraft system optimization[79]–[82]. In the field of optics, DL has been used recently to predict and model plasmonic behavior[76], [83]–[87], grating structures[53], [88], ceramic metasurfaces[89], [90], chiral materials[91], [92], particles and nanosturctures[55], [93], [94], and to do inverse design[55], [76], [86], [94]–[97]. Deep-Learning has also been used extensively in the field of heat transfer for applications such as predicting thermal conductivity[98], [99] and thermal boundary resistance[100], studying transport phenomena[101], optimizing integrated circuits[102], modelling boiling heat transfer[103], predicting thermal-optical properties[53], [104], [105], and addressing thermal radiation problems[106]–[109].

Image-based deep learning methods have been shown to be particularly effective in generating robust networks that are capable of both high levels of extrapolation and in material and topology optimization. While often used for classification[137], [138], images processed using convolutional layers are highly effective in making predictions for both classification and regression problems[111]. For optical applications, convolutional networks have been shown to be effective in predicting properties of fabricated samples[139]–[141], for plasmonic structures[87], [95], metamaterials[89], [142], [143], and when combined with a generalized adversarial network (GAN)[144], [145]. Convolutional networks are designed to learn and develop patterns from large tensors of information (images) and to develop non-linear relationships within the image data that enable high levels of accuracy and dataset extrapolation.

In this chapter a methodology based on a convolutional deep neural network to predict the optical properties of micropyramids across a wide design space of geometries, wavelengths, and materials is shown. As opposed to many other studies that provide a deep learning approach to a structure with a single material[83], [95], a geometry with fixed materials[53], [91], [94], or a material input defined by one-hot encoding with a random forest[55], the CDNN shown in this chapter is designed to directly emulate the simulation process by taking in finite-element like mesh images that contain geometric and material information. This method is combined with the previously developed network shown in Chapter 3 and results in a significant improvement in accuracy when extrapolating the optical properties for new materials. The model shown is a direct improvement upon our previous work[146], with a significantly higher prediction accuracy for microstructures made of materials not included in the training process. These models are not bound by

material classification, and while we apply the methodology to improve our prediction accuracy for micropyramids, the method we show has vast potential applications to complex metasurfaces, higher order geometries, and systems with multiple materials. Ultimately, the method shown here could be developed into a method that could potentially completely replace FDTD simulations for periodic microstructures and enable complex inverse network designs.

4.2 Convolutional Deep Neural Network Design

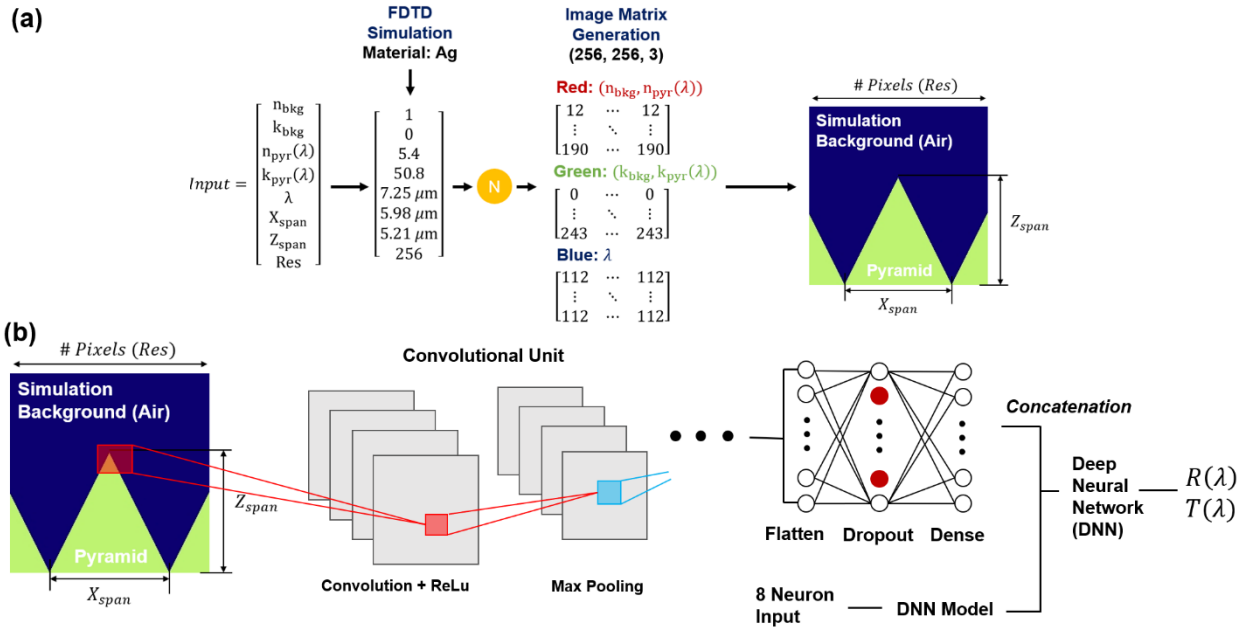

Figure 4-1 (a) Discretization process of inputs into an image. Each pixel contains 3 values (corresponding to the RGB channels, the refractive index (n), extinction coefficient (k) and wavelength (λ). The background (shown in blue) will always contain an invariant value for the n and k values (1 and 0 respectively), while the pyramid structure is defined by the material information for a given wavelength. (b) The network takes in this image, and processes using multiple groups of Convolution, ReLu, and max pooling layers. The CNN output is combined with the DNN model and processed through a final DNN before outputting the λ value dependent reflectivity and transmissivity

We further enhance the neural network design philosophy shown in Chapter 3 by more directly mimicking the FDTD optical solver by making a network that analyzes a pseudo-mesh. In FDTD, the optical solution for a given combination of material and geometry is derived from solving Maxwell's equations across a discretized mesh[147]. The only way the FDTD model can differentiate between two distinct materials (e.g., air and the pyramid) is by assigning the λ-dependent material properties to each cell across the mesh. Here, we approximate that process by generating an image that utilizes the spectrally dependent material in conjunction with the geometric information.

From a mathematical perspective, an image is nothing more than a tensor. Thus, we can effectively use an image to convey multi-dimensional information that relates material properties and spatial orientation. As shown in Figure 1, we take a three-dimensional matrix of material information and translate it to a standard 3-channel RGB image, with each pixel containing a vector of material data. While the convolutional process is compatible with higher or lower order tensors, for ease of use and to simplify data storage/the image generator, we utilize a standard 3-channel color image. The vector used to generate each image is the same 8-input vector described in the Chapter 3, which contains the simulation wavelength (λ), pyramid geometry (x_{span}, z_{span}, t_{sub}), and material properties of the microstructure (n, k, ε_{real}, ε_{im}). As the image contains information beyond the pyramid, two additional static background material properties ($n_{bkg} = 1$ and $k_{bkg} = 0$) are required to fully define the space. As the maximum Xspan and Zspan in the simulations are fixed to a maximum of 10 μm, each image is set to be an effective 10 x 10 μm – with the vertical and horizontal pixel resolution defining the "cell" length. To minimize memory consumption, we employ a 256 x 256-pixel configuration. This effectively means that each pixel represents ~

40 nm, indicating that the minimum feature size we can effectively depict is ~ 40 nm. Therefore, we eliminate any simulations with a pyramid base size or height less than 40 nm. As visualized in Figure 2, we build pyramids symmetrically about the center of the image, filling in the remainder of the space symmetrically until the combined pyramid base span is 10 um. As an example, a pyramid with a base span of 10 um will perfectly fill the bottom horizontal axis of the image. A pyramid with a base span of 1 um will be replicated a total of 10 times in the image. This can be thought of as equivalent to the mesh resolution in an FDTD simulation, with a larger image conveying more spatially dependent information and allowing more accurate simulations and more complex structures. For the sake of minimizing memory consumption and training time, we choose to utilize a 256 x 256 image (~ 40 nm per pixel), but the selected size is only functionally bounded by minimizing computational time.

Two set of inputs CDNN architecture evaluates two inputs: the generated image and the 8-input vector of geometric, material, and wavelength information. The image component is interpreted by a convolutional neural network. The convolutional neural network is comprised of multiple "units" – each "unit" contains a convolutional layer with a ReLU activation function (defined by Eq.1) followed by a max-pooling layer.

$$f(x) = \begin{cases} 0 & for\ x < 0 \\ x & for\ x \geq 0 \end{cases} \qquad \text{(Eq.1)}$$

After 5 convolutional units with an increasing filter configuration (64, 128, 256, 256, 512), we apply a 0.25 dropout layer followed by a flatten layer, a dense layer, a larger 0.5 dropout, and finally a dense layer. The second component, the 8-input vector is used as an input to a

deep neural network. This input vector contains details that either cannot be in the image – such as the thickness and excluded material properties – or information present in the image such as the material information and geometry to reinforce the model's interpretation and prediction performance. The output of this DNN is concatenated with the output of the CNN, and then passed through a final set of dense hidden layers. While we could directly link the concatenation to the output, we found that combining the concatenation of the DNN and CNN with another set of dense fully connected layers significantly improved prediction performance. The model's output is the same as the previously demonstrated DNN's output in Chapter 3 – the reflection and transmission value that correspond to the input simulation wavelength.

Architecturally, the CDNN network combines a similar DNN structure with a CNN model. The first DNN structure takes in the same input vector as previously discussed network but uses a smaller set of layers and neurons (5 hidden layers, 300 neurons). The CNN uses 6 groups of convolution – ReLU – max pooling. The filter configuration for the convolutional layers is 64, 128, 256, 256, 512, 512. The final convolutional layer is followed by a max pooling, dropout (0.25), flatten, dense, dropout (0.5), and then a final dense layer. The output is concatenated with the DNN structure and fed into another DNN, which is 7 fully connected dense layers with 1024 neurons each. We utilize a custom image generator process to handle the import of images and their associated deep neural network properties into the model. We combine 35,500 FDTD simulations for micropyramids made of 14 different materials to form our training, validation, and test dataset. We follow a 70/20/10 percentage split respectively. The test dataset is used to evaluate the performance and overfitting of the model and it is not seen by the network in the training process; this dataset

includes only materials that were seen by the model in training and validation. We shuffle the complete dataset every time the model is run or generated such that the training, validation, and test datasets are never identical from iteration to iteration. An additional 1500/1000 simulations of Ti and Al2O3 micropyramids respectively and 25 materials with 100 simulations each (5000 simulations total) are used to evaluate the performance of the network in predicting materials not included in the training/validation process. All simulations are normalized using the quantile method to ensure dataset uniformity and, more importantly, limit the network's loss of understanding for parameters with near 0 values where the output difference for an input of 1e-2 and 1e-3 or 1e-4 can be significant.

4.3 Model Prediction Results

The CDNN surrogate method is more effective at accurately extrapolating optical properties for new materials when compared to the DNN only surrogate method. When only 20% of the available simulation data (~ 710,000 images) is used in the training/validation/testing process, we can match or exceed the performance of the DNN. The precise performance is dependent upon the selection of the material properties used in the three available pixel matrix dimensions. While the selection of the first two-pixel dimensions (the complex refractive index) is straightforward, the third quantity was a point of study. In table 1, we show the performance of the CDNN architecture in predicting the Ti, Al2O3, and material library datasets when different quantities are used in the third matrix dimension. Based on these results, we observe that the wavelength is the most effective parameter to use in the third dimension. This provides additional confirmation that the wavelength is an extremely important parameter in enabling the model to build proper connections between the input and output. This is despite each image there will be no

variation across the matrix for the wavelength value, effectively making the third channel to always be 1 of 100 possible values. The model evaluations shown in Table 1 are performed using the complete unseen datasets, we apply the 20% limitation only to the model's training data. While the deep neural network shown in Chapter 3 outperforms the limited CDNN, the performance is comparable despite the CDNN using only 20% of the available data. It is likely that increasing the dimension of the input tensor of the "image" would also increase the accuracy, but it would also serve to further complicate the process, increase computational demands, and decrease user intuition. In Figure 2, we compare the accuracy of the DNN and CDNN in predicting the test dataset for both the reflectivity and transmissivity. While we only use 20% of the dataset to train and validate the CNN model, we randomly select 10% of the entire simulation data pool to generate the test dataset in both cases. Despite the significant difference in available training data, the two methods do not show a significant discrepancy in the observed training and validation errors.

Method (% Data)	Channels	Train	Validation	Ti	Al2O3	Library
DNN (100%)	N/A	0.0032	0.0033	0.0175	0.0141	0.0279
CDNN (20%)	n, k, 0	0.0031	0.0036	0.0171	0.0225	0.0373
CDNN (20%)	n, k, ε_{im}	0.0019	0.0032	0.0266	0.0176	0.0378
CDNN (20%)	n, k, ε_{real}	0.0029	0.0031	0.0233	0.0184	0.0346
CDNN (20%)	n, k, λ	0.0025	0.0031	0.0185	0.0163	0.0314

Table 4-1 Comparison of training, validation, and unseen material dataset performance for the DNN and CDNN methods. To greatly speed up the training/validation time, we only use 20% of the available data to train the CDNN (~ 710,000 images of 3.55 million)

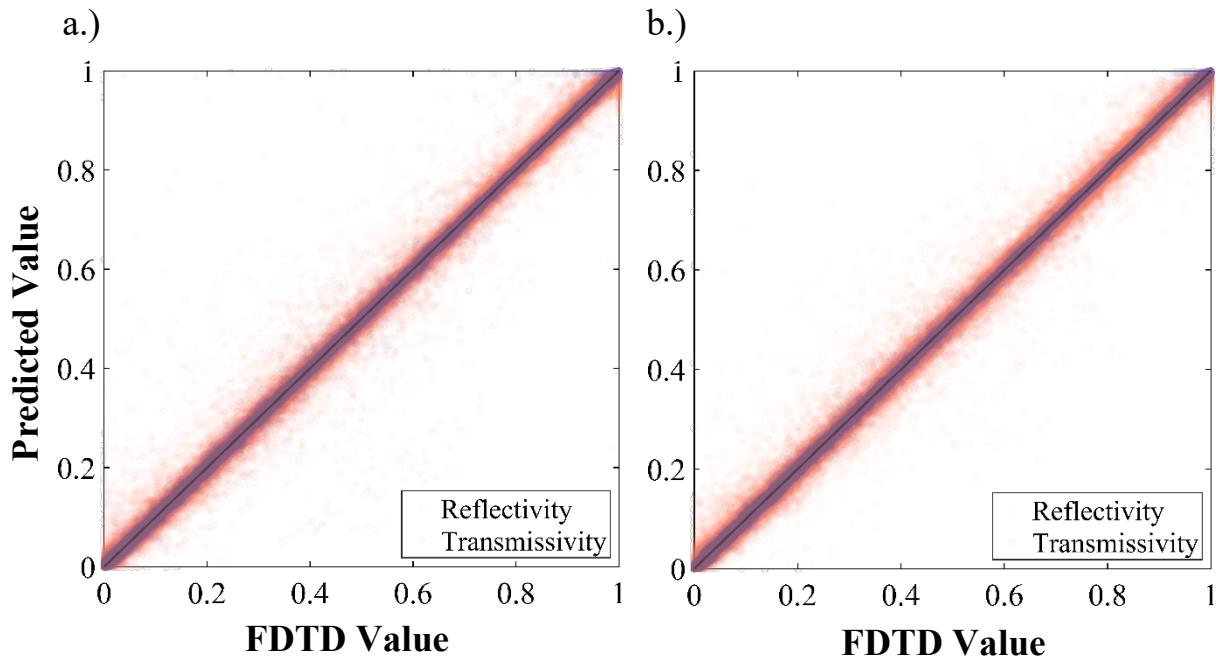

Figure 4-2 Comparison of the test dataset results for the (a) deep neural network standalone network and (b) convolutional deep neural network. The results are virtually indistinguishable, with an exceptionally high prediction accuracy in both cases. All materials in the test dataset simulations are seen by the neural network in training

When we enable the model to see the full simulation dataset in training that the DNN does (3.55 input vectors, or 3.55 million images taken from 35,500 simulations), the CDNN method significantly outperforms the DNN method. The Ti, Al2O3, and library datasets have an evaluated MAE of 0.0155, 0.0113, and 0.0226 respectively. When we calibrate the model with 5 – 10 simulations as previously demonstrated in the DNN, this decreases to 0.0067, 0.0043, and 0.0098 respectively. In Figure 3, we compare the library predicted values for the

calibrated DNN to the calibrated CDNN that is trained on the entire 35,500 simulation dataset. While the two models have the same data available to them, the CDNN shows significantly improved performance in extrapolating the optical properties of materials that are outside of the scope of the training data.

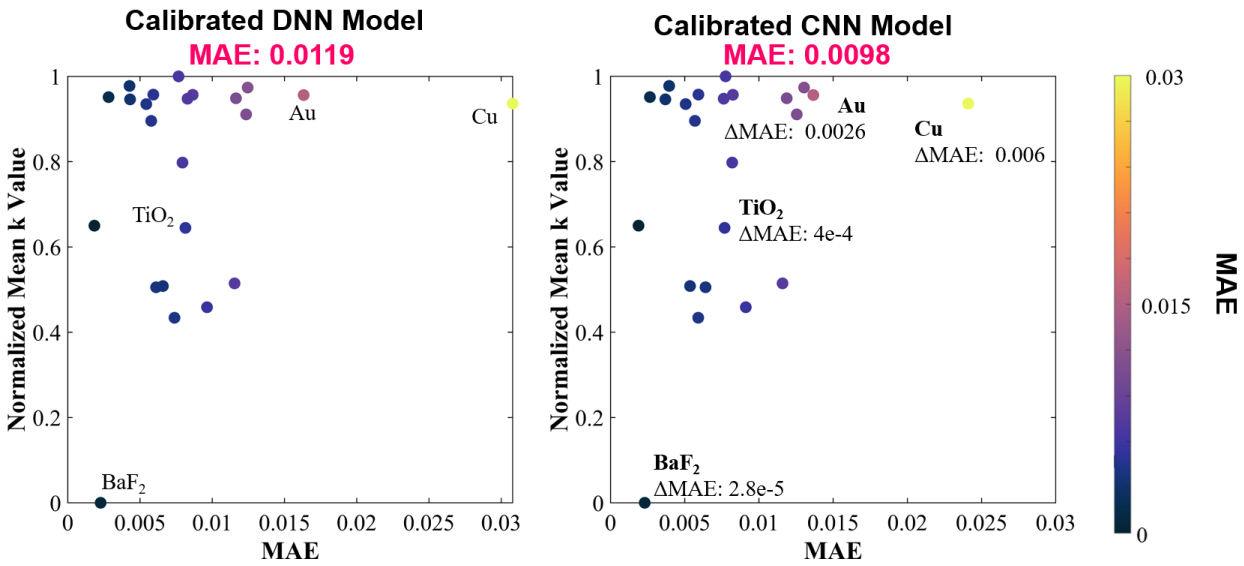

Figure 4-3 Visualization of error between the calibrated DNN shown in Chapter 3 and the CDNN method for the unseen library of 23 materials. While some materials significantly improve (such as Au and Cu), the change in some other materials is virtually indistinguishable

4.4 Discussion and Comparison to DNN

Perhaps the most significant advantage of a surrogate method using deep learning is the significant decrease in prediction time for an input compared to the method it is replacing. For the deep neural network surrogate, we demonstrated previously, we estimated that the predictions could occur from 6 to 8 orders of magnitude faster than using traditional FDTD simulations. While the CDNN method we demonstrate here is more

accurate than the DNN, due to the relative increase in parameters, memory scale, and type of input the training time and prediction time for the CDNN is significantly longer than the DNN. The significant training time necessitated network architecture tuning, hyperparameter tuning, and network design to occur with 5-20% of the available simulation data and limited our ability to train networks with 100% of the available data as we had with the DNN shown in Chapter 3. With our available computational resources, training the CDNN on the complete dataset could take 500 – 900 hours, compared to no more than 30 – 50 hours to train the DNN. Training time can often be an investment, however, and should not necessarily be considered a strong limitation as once the model is completed, it does not require such significant amounts of time to run. Therefore, what may often matter more is the prediction speed of the network. Here, the DNN is still superior. The DNN can predict a full simulation in approximately ~ 200 us, compared to ~ 20 milliseconds per simulation for the CDNN. Thus, we estimate that the CDNN is 4 – 6 orders of magnitude faster than a FDTD simulation. While still incredibly fast comparatively, the speed difference is readily apparent when predicting large grids of simulation information. This significantly impacts the time required to perform optimization or generate training data for an inverse network (Ch. 5). Despite the significant accuracy increases of the CDNN to the DNN, the accuracy of the calibrated DNN is still very high, and in most cases, it is likely that the time required for usage is not worth the increase in prediction accuracy for very large datasets.

While the DNN does outperform the CDNN in time performance, the results make it abundantly clear that the image-based approach is significantly more accurate, especially in extrapolating for materials that are outside of the scope of training. Part of this could be attributed to the significant increase in training parameters in the CDNN compared to the

previously shown DNN. However, when we experimented with increasing the layer and neuron configuration in the standalone DNN led, we observed significant overfitting as the model improved in training and validation accuracies but decreased in extrapolation performance for the unseen material simulations. It is also important that decreasing the extrapolation error becomes more and more challenging as the error approaches zero. As discussed in Chapter 3, early iterations of the deep neural network architecture, normalization, etc., yielded mean-absolute errors for the unseen materials up to 0.1. This value rapidly decreased with initial improvements and modifications but plateaued near the discussed error values. The image-based approach we demonstrate here moves past these limitations, enabling the model to have a much deeper physical understanding of the available problem. The extrapolation results substantiate this, as completely unseen materials are predicted with a far higher accuracy by the CDNN than with the DNN despite no additional simulations or information being made available to the CDNN.

The advantages of the image-based approach will be more apparent – and significant – for systems that demonstrate higher levels of geometric or material complexity than the single material micropyramid. Variations in material add significant levels of complexity to the problem, but that complexity would be further amplified by the inclusion of multiple materials in a single domain. This could be complicated even further by including higher order geometries such as hierarchical structures, coatings, or asymmetric geometries. Moving beyond micropyramids, complex structures such as composite porous layers, microsphere composites, materials with embedded inclusions, etc., demonstrate a significantly higher number of degrees of freedom and would be much more difficult to model with the standalone DNN approach. The significant advantage of the image-based

approach is that it can accommodate not only multiple materials but complex geometries. As the CDNN method is similar to discretized mesh, high resolution images with a low nm/pixel value are capable of abstracting the optical properties for complex geometries and multi-material systems in ways that the deep neural network is unable to. The image based surrogate method with enough simulation data for varying structures could eventually be generalized to a solver that is capable of extrapolating optical properties for unit cells of arbitrary shapes and materials. Furthermore, this structure could potentially build upon itself using an adversarial design, forming a self-learning topology, geometry, and material optimization engine for optical metasurfaces.

Conclusions

We have exhibited a surrogate neural network that can replace finite difference time domain simulations for microstructured surfaces. The model is capable of accurately extrapolating the optical properties of micropyramids made of materials that are far beyond the scope of training and can do so far more accurately than the standalone deep neural network. The image-based convolutional deep neural network is a direct improvement upon our previously developed deep neural network surrogate, reducing the error on predicting for a library of materials from 0.0279 to 0.0196 when uncalibrated and 0.0118 to 0.0098 when 5 simulations of each unseen material are included in the network training data. The model shown here can make optical predictions at a rate that is 4 to 6 orders of magnitude faster than the same inputs simulated in FDTD. Furthermore, the results of the convolutional deep neural network are nearly indistinguishable from the FDTD simulation results, even when extrapolating optical properties for micropyramids made of materials not included in

the training and validation process. The surrogate network demonstrated here validates the approach of using an image to convey material and simulation information, enabling the model to learn complex and non-linear relationships between the inputs and understand how geometry and material are related to the optical properties. This methodology can not only be translated to other microstructures but opens the possibility for networks that can predict the optical properties and make thermal predictions for multi-material and geometrically complex systems.

Chapter 5 – Inverse Micropyramid Design Driven by Deep Learning

5.1 Inverse Design Introduction

Designing and optimizing structures to selectively control optical properties can be a significant and time-consuming challenge. Beyond the potential for many degrees of freedom in the geometric design space, material selection adds an additional level of complexity. Solving the interplay between a complex geometry and material selection can require both a significant investment in computational resources and a dedicated numerical method such as a finite-difference time-domain (FDTD)[75] solver. A highly effective method that has emerged to counteract the necessity of complex simulation tools is the use of Deep Learning (DL) to predict optical properties. A branch of machine learning (ML), DL methods have shown to have a high degree of non-linear abstraction from datasets[76] and to address complex issues such as self-driving cars[77], speech recognition[148], and natural language processing[149]. Deep Learning has been used in the field of photonics and nanophotonics to predict and model problems such as plasmonic interactions[76], [87], grating structures[46], [53], [88], particles[55], [94], and nanostructures[93]. DL has also been extensively applied within the field of thermal engineering to study topics such as thermal conductivity[98], boiling heat transfer[150], and radiative thermal transport[104], [108], [109].

Deep Learning has proven to be not only effective in predicting the "forward" problem by replacing the optical solution process, but also in performing inverse design[55], [76], [86], [94], [96], [97], [151], [152]. Inverse design, broadly, is taking a desired input and outputting a set of features that generate the input. Compared to common optimization tools,

inverse design via machine learning methods is highly effective in increasing throughput and prediction speed. A multitude of methods exist for executing an inverse design scheme in nanophotonics[153], but several common methods include the use of a surrogate model in conjunction with an optimization method[154], [155], the creation of a the "tandem" or bidirectional scheme[55], [76], [91], [96], [156], and adversarial networks[142], [157]. Inverse design methods based on machine learning have been applied to the design of selective emitter structures; methods based on images[158], deep learning[159], deep-binary search[160], transfer learning[161], and genetic algorithms[162], [163] have been shown to be effective in previous studies. While some studies do factor in the material selection as an output in the inverse design process, they are often limited to a small set of fixed material outputs[55], [161].

Material selection plays a fundamental role in the design of selective emitters as the interaction of light with the surface is regulated by the spectral material properties[70]. If a microstructure or material is not capable of regulating certain wavelengths, a designer can coat additional material(s) to enhance the broadband response[36], [47], [164], [165], create a new composite material[110], [166], or select a new material as the basis for patterning. Thus, it is critical to be able to exhaustively search over the available material space to provide the best fit for a given set of thermal design criteria[146]. To be exhaustive in the inverse design approach, the material output cannot be fixed and should be flexible to allow the discovery of unique combinations of material properties with geometric properties.

In this work, we propose an inverse microstructural design method based on a tandem neural network constructed to take in a set of desired optical properties and output a set of

material and geometric properties. We supplement the tandem neural network – consisting of a surrogate network and inverse network – with post-processing methods to allow the aggregated network to consider critical physical design constraints. The aggregated network is designed in an adversarial style process loop to facilitate the model to iterate and build upon itself over subsequent generations and consider focused feedback from the post-processing checkpoints. The foundation of our method is built upon a previously developed optical simulation surrogate based on a deep neural network (DNN)[146]. As opposed to many other studies that provide a deep learning approach to optics where a single material is simulated[95], the materials are fixed[53], or are one-hot encoded[55], our surrogate method does not constrain material input and can extrapolate to make predictions for materials that were not used in training. The flexibility provided by this method enables us to build an inverse neural network structure to work in tandem with the surrogate that is similarly unconstrained by material classification. Our inverse network structure is capable of not only predicting an optimal material for a given desired input but is capable of extrapolating new material properties to match a given desired input.

The model we demonstrate takes in a simple input of optical properties across a wavelength range and outputs a material and micropyramid geometry that best match it. Multiple deep learning methods are utilized in the construction of the method. We compare the previously established deep neural network surrogate to an image-based surrogate and incorporate recurrent neural network functionality to improve the inverse network's prediction performance. While we demonstrated limited optimization using the surrogate[146], the inverse network enables far more rapid, dynamic, and global optimization. The output of the inverse neural network is put through a post-processing

stage where user set geometric and material constraints are used to produce appropriate solutions. The novel generated material properties are matched to a material from a library material, the constrained output is simulated, and the results are incorporated in the surrogate network. Using this process, we can rapidly optimize a material and geometric combination for a desired optical spectrum in a process that would be too computationally expensive to perform otherwise. While we apply our methodology to micropyramid structures, the approach that we demonstrate can be modified to accommodate any number of microstructural surface topologies.

Figure 1 provides a comprehensive schematic of the aggregate neural network framework. As visualized in Figure 1, the general process flow is FDTD simulations are used to train the surrogate neural network and the surrogate is used to make large-scale predictions derived from a library of materials. The predictions are then used to train an inverse neural network component. The input of the inverse network is a desired optical spectrum (λ, ε, R, T) and the output is the predicted micropyramid base span, height, substrate thickness (X_{span}, Z_{span}, and t_{sub}), and a vector of complex refractive index values ($n(\lambda)$, $k(\lambda)$) that correspond to the input wavelength. The post-processing module then interprets the output. Here, user constraints – such as the maximum aspect ratio – are used to adjust the predicted output and provide appropriate new solutions that satisfy the restrictions. The adjusted solutions are then passed through both FDTD and the surrogate model. Based on the results, a decision is made to either retrain the surrogate with the new simulation data, or to stop the loop if the solution is deemed to be sufficient and accurate. Any details not discussed in any of the major subcategories for all modules and connections can be found in the methods section or in the linked code repository.

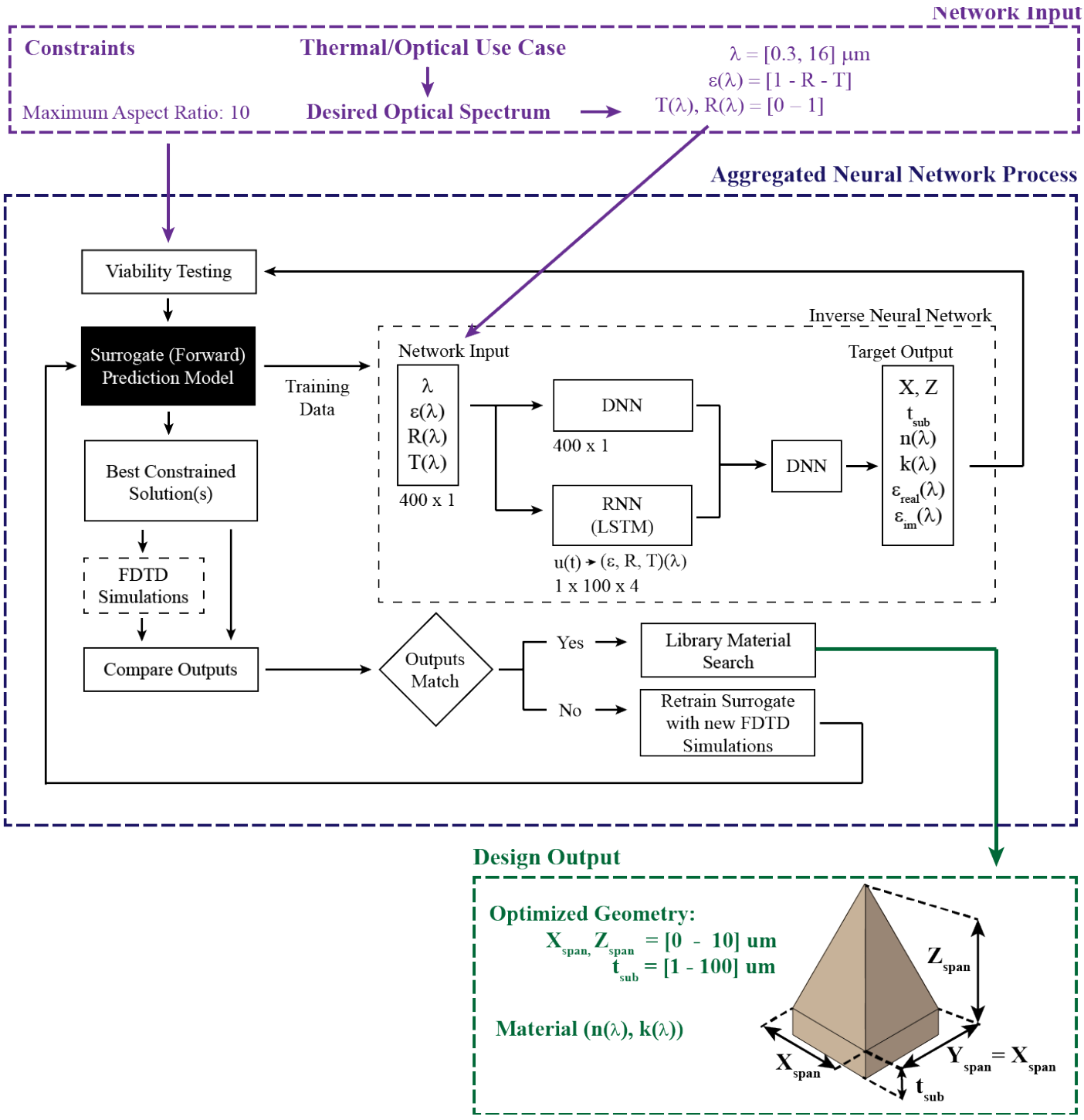

Figure 5-1 Aggregate Neural Network Design. The user inputs the desired design spectrum, wavelength, and specifies constraints. The neural network identifies a material and geometry that solve the inverse problem. The neural network uses simulation results to learn from prediction mistakes and retrain the surrogate network to make better subsequent predictions

5.2 Methods

5.2.1 FDTD Simulations

Solutions using the FDTD method, while accurate, can be time intensive – this is especially true for large or geometrically complex structures. For this work, the training, validation, and testing data used by the surrogate neural network is compiled from simulations completed in Lumerical's commercially available 2D/3D FDTD solver. The simulation framework provides exact solutions for Maxwell's equations across a finite element mesh, and the absorption and dispersion are derived from the resulting electrical fields[57], [58]. Rather than simulating a 3-dimensional (3D) pyramid microstructure, we simulate the middle-cross section in 2-dimensions (2D) to minimize simulation time and to enable the generation of large quantities of simulation data. While this does lead to an overestimation of the micropyramid's emissivity[116] compared to the 3D micropyramid simulations, the results are still accurate as we do not vary the incidence angle in our simulations and assume the broadband wavelength source to be at a normal angle to the material's surface. Additionally, while we could choose to use a semi-analytical approach like RCWA to run the simulations[21] to estimate the optical properties of a 2D structure, FDTD's accuracy, scalability, and its applicability to other more complex geometries make it a far viable long-term solution. The simulations are based upon a micropyramid geometry visualized in Fig. 2, with the key independent geometric parameters being the triangle base span (x_{span}), height (z_{span}), and substrate thickness (t_{sub}). For this work, we assume that Kirchhoff's law is valid and the emissivity can be derived from $\alpha = \varepsilon = 1 - R - T$, where reflectivity (R) and transmissivity (T) are calculated from power monitors above and below and domain respectively and where absorptivity (α) is synonymous with emissivity (ε)[146]. To develop

the simulation datasets used to train the surrogate, we generate and simulate matrices of randomly generated uniformly values for the x_{span}, z_{span}, and t_{sub} for each material included. For simplicity, we assume no additional coating materials, hierarchical structures or surface roughness. Additional details on our FDTD simulation methodology can be found in Chapters 2 – 3 and in our prior work[20], [110], [116], [164].

5.2.2 Network Architecture and Optimization

We use a deep neural network with fully connected dense layers. Our deep learning approach is built upon the open source keras library in python[117]. The surrogate network, as previously published[146], uses an optimized DNN with 8 fully connected dense layers with 400 neurons per layer, and both MLPs are 4 layers of 50 neurons each.

The CDNN network combines a similar DNN structure with a CNN architecture. The first DNN structure takes in the same input vector as previously discussed network but uses a smaller set of layers and neurons. The CNN uses 6 groups of convolution – ReLU – max pooling. The filter configuration for the convolutional layers is 64, 128, 256, 512, 512, 512. The final convolutional layer is followed by a max pooling, dropout (0.25), flatten, dense, dropout (0.5), and then a final dense layer. The output is concatenated with the DNN structure and fed into another DNN, which is 7 fully connected dense layers with 1024 neurons each. We utilize a custom image generator process to handle the import of images and their associated deep neural network properties into the model.

The inverse network takes the same set of inputs (1 x 400 vector) and applies it in two separate ways. The first is a direct input to a deep neural network, with a 1 x 400 input shape, which consists of 6 fully connected dense layers of 750 neurons each. The second input

recasts the original 1 x 400 vector into a 1 x 100 x 4 vector and is put into a recurrent neural network. The RNN is constructed of 3 bi-directional LSTM modules – that is, a bi-directional LSTM layer followed by a dropout (0.5). Each bi-directional LSTM layer has 320 neurons, and the final layer's output is non-sequenced. The outputs of the RNN and DNN are concatenated and then fed into a larger deep neural network that consists of 6 layers of 1000 neurons each. The final output is 403 neurons with no applied activation function. We experimented with different methods of combining the two outputs – including matrix multiplication, addition, and subtraction – but found that the concatenation was consistently yielded the best results.

For training all the models, we utilize a MSE loss function and validate/evaluate using an MAE score based on equations 1 and 2 respectively, where Y_i is the predicted value. A key change to the model training compared to prior results is that all data is made available to the network and there are no "unseen" materials in the training process. For the grid generation process, we do utilize several materials that are outside of the scope of the training process, but no simulation data was generated for these materials prior to training the reverse network. The full list of materials included in training and in grid generation are provided in the

$$MSE = \frac{1}{n}\sum_{i=2}^{n}\left(Y_i - \widehat{Y_i}\right)^2 \qquad \text{(Eq.2)}$$

$$MAE = \frac{\sum_{i=1}^{n}|Y_i - \widehat{Y_i}|}{n} \qquad \text{(Eq.3)}$$

In all cases, optimization of the hyperparameters is performed with the built-in hyperband optimization method[118]. Adam is the optimization engine used for the network training in all cases. To minimize overfitting, we utilize L2 regularization in the training and

validation process, in addition to utilizing early stopping, checkpoint save, and reduce learning rate on plateau callbacks with low patience values[146]. Some models incorporate dropout layers to further reduce model overfitting.

5.2.3 Datasets and Normalization

All datasets used by the neural networks are derived from FDTD simulation inputs and outputs directly. For each material in the training/validation/test dataset of the surrogate models, we generate a uniformly distributed random matrix for each of the geometric properties to use as inputs for the simulation. The simulation wavelength and n and k values are taken from each simulation and split into sets of input data, spanning a total of 8 neural inputs (n and k are converted into ε_{real} and ε_{im}). The simulation output is 100 emissivity and 100 reflectivity points that one-to-one match the simulation wavelength vector, which is divided into pairs for each λ. For this work we utilize several normalization methods depending on the input dataset. X, Z, and λ are considered uniformly distributed random numbers, and a simple linear normalization is applied to each separately using Eq. 4.

$$x_{norm} = \frac{x - x_{min}}{x_{max} - x_{min}} \qquad \text{(Eq.4)}$$

The distribution of k, t_{sub}, ε_{real}, and ε_{im} pose a more significant normalization challenge. The ε_{real} permittivity value is of particular concern due to the negative values induced by $-k^2$ term shown in Eq. 5.

$$\varepsilon_{real} = n^2 - k^2 \qquad \text{(Eq.5)}$$

The dataset distribution before and after normalization for each input is shown in the supplementary materials. A fundamental problem faced is that optically, the difference between k = 1e-4 and 1e-3 is not mathematically large, but the difference does have a large impact on the transmission behavior through the substrate. Thus, the data is grouped near 0 but we need to differentiate values in a meaningful way to distinguish the physical behavior of each material. Log normalization reduces the severity of the weighted inputs but does not solve it. Therefore, for these variables, we turn to more complex normalizations. For all of the datasets shown in this work, we utilize quantile normalization with sklearn's built in quantile transformer, to generate a uniform distribution of inputs for k, t_{sub}, $\varepsilon_{real,}$ and ε_{im}. A change from our previous results[146] is that we simplify the normalization pipeline by normalizing the refractive index n using the quantile method. All datasets used in this work, and the techniques used to normalize, denormalize, and configure the data are provided in our GitHub repository linked Appendix B.

For the surrogate models, we combine 40,500 FDTD simulations for micropyramids made of 41 different materials to form our training, validation, and test dataset. We follow a 70/20/10 percentage split respectively. The test dataset is used to evaluate the performance and overfitting of the model and it is not seen by the network in the training process. We shuffle the complete dataset every time the model is run or generated such that the training, validation, and test datasets are never identical from iteration to iteration.

For the inverse model, the training data is generated using the surrogate data. Whereas the surrogate provides the reflectivity and transmissivity provide an output for an individual wavelength point, the inverse uses a full vector input by stacking predictions from

the surrogate. The full wavelength vector input that corresponds to an output we refer to as a "surrogate simulation". For each material, we develop a grid of surrogate simulations by varying the xspan and zspan of the micropyramid and attaching a randomized wavelength vector and thickness value for each individual set of (xspan, zspan) in the grid. The grid is generated using a meshgrid process with the xspan and zspan set as linearly spaced vectors. The randomization process for the wavelength vector involves creating a linearly spaced vector of 100 points with a randomized minimum and maximum value. The minimum and maximum values are the randomly generated parameters and are between (0.3 – 15) and (2 – 16) μm respectively. If the randomly selected "minimum value" is larger than the "maximum" value, the values are switched in generating the wavelength vector. The random process is iterated to ensure that the gap between the minimum and maximum wavelength values is 1 um. The material information is generated from inputting the generated wavelength vector into a splined curve fit. The splined curve-fits are generated using a 2000-point dataset for each material.

5.2.4 Post-Processing: Material Fitting

The output of the inverse neural network contains a vector of n and k values, matched to an input of wavelength points. To provide the "best-fit" material, we compare the material data (n, k) to the material data in the library. The library data is generated using the same spline process as described in the previous section and depends on the user wavelength spectrum that was input into the reverse network. We check each (n, k) vector combination in the material library against the model output using the least-squares method shown in Eq.6.

Before comparing the values using Eq.6, we adjust the (n,k) vector using a log transformation shown in Eq.7. While a comparison using Eq.6 is still viable, the log adjustment allows for better comparisons to materials that depend strongly on minute differences in n, k values. As discussed, transmissive materials depend strongly on small changes in the n and k values, so having a scale that enables better comparison for small values enables us to draw better conclusions from Eq. 6as to which materials best match the ML output.

$$LSE = \sum_{i=2}^{n}\left(Y_i - \widehat{Y}_i\right)^2 \qquad \text{(Eq.6)}$$

$$(n,k)_{adj} = \log_{10}((n,k) + a) \qquad \text{(Eq.7)}$$

5.2.5 Post-Processing: New Solution Generation

In the post-processing module, we adjust the inverse network output according to user set constraints. In our present work, we only limit the aspect ratio, but the method can easily be adjusted to account for more conditions. To do this, we generate two sets of new geometric coordinates (for the same material) that do not violate the constraint. The process starts by adjusting the original solution's x and z coordinate while fixing the other coordinate until the aspect ratio is within the constraint's bounds. This follows our previously established intuition on the role of aspect ratio in determining optical/thermal property optimality[116]. For a different microstructure, we would need to adjust this process to match the observed patterns for the microtexture and the desired constraint. From these two new points, we generate new geometric pairs within a radius around the modified geometric coordinate. The generation process is random and uniform, and solutions that are not below or equal to the desired aspect ratio are eliminated. All viable solutions are then

passed into the surrogate for predictions; the results that best match the desired input are simulated in FDTD. We also select random points from the remaining pool of randomly generated viable geometric solutions to have additional solution variety and to reduce concerns of over-biasing the network when the surrogate incorporates the new FDTD solutions in training. The desired input and model/FDTD outputs are evaluated for optimality using Eq. 5. This process is used to generate solutions separately for the direct ML material output and then the "best-fit" material(s). We will often only use a single "best-fit" material, but for some cases we will look beyond the first library match.

5.2.6 FDTD Simulations

Solutions using the FDTD method, while accurate, can be time intensive – this is especially true for large or geometrically complex structures. For this work, the training, validation, and testing data used by the surrogate neural network is compiled from simulations completed in Lumerical's commercially available 2D/3D FDTD solver. The simulation framework provides exact solutions for Maxwell's equations across a finite element mesh, and the absorption and dispersion are derived from the resulting electrical fields[57], [58]. Rather than simulating a 3-dimensional (3D) pyramid microstructure, we simulate the middle-cross section in 2-dimensions (2D) to minimize simulation time and to enable the generation of large quantities of simulation data. While this does lead to an overestimation of the micropyramid's emissivity[116] compared to the 3D micropyramid simulations, the results are still accurate as we do not vary the incidence angle in our simulations and assume the broadband wavelength source to be at a normal angle to the

material's surface. Additionally, while we could choose to use a semi-analytical approach like RCWA to run the simulations[21] to estimate the optical properties of a 2D structure, FDTD's accuracy, scalability, and its applicability to other more complex geometries make it a far viable long-term solution. The simulations are based upon a micropyramid geometry visualized in Fig. 2, with the key independent geometric parameters being the triangle base span (x_{span}), height (z_{span}), and substrate thickness (t_{sub}). For this work, we assume that Kirchhoff's law is valid and the emissivity can be derived from $\alpha = \varepsilon = 1 - R - T$, where reflectivity (R) and transmissivity (T) are calculated from power monitors above and below and domain respectively and where absorptivity (α) is synonymous with emissivity (ε)[146]. To develop the simulation datasets used to train the surrogate, we generate and simulate matrices of randomly generated uniformly values for the x_{span}, z_{span}, and t_{sub} for each material included. For simplicity, we assume no additional coating materials, hierarchical structures or surface roughness. Additional details on our FDTD simulation methodology can be found in both the methods section and in our prior work[20], [110], [116], [164].

5.3 Aggregate System Design

5.3.1 Surrogate Neural Network

Deep learning modules have been shown to be exceptionally strong and versatile in solving the so called "forward" problem[76], [97]. In this case, the problem to solve is the optical response from a geometric and material input for a uniform periodic micropyramid surface. The design intent of the surrogate neural network is to act as an ultra-fast and accurate predictor of optical properties such that we can rapidly and accurately predict the optical properties of vast quantities of simulations. Furthermore, it is important that the surrogate network can extrapolate optical properties for materials beyond its original

training scope. As such, we compare two methods that serve this function: an improved version of a previously developed deep-neural network[146], and an image-based deep convolutional neural network (DCNN). Both methods utilize datasets generated in FDTD that are subdivided into training, validation, and test datasets. The datasets used to train and validate the model encompass over 35000 simulations of microstructures comprised of 14 different materials. The materials chosen have widely varying complex refractive indices, and include metals (Ni/Ag/Al/Cr/Fe/Sn)[69], [119], [120], refractory metals (Ta/W)[69], [121], a phase-change material (VO2 Metallic/Insulating)[122], a polymer (PDMS)[62], a semiconductor (SiC)[123], a ceramic (SiO2)[69], and a material with a near zero extinction coefficient across a wide spectrum (Diamond)[124].

Surrogate Neural Network: Deep Neural Network

The architecture of the deep neural network – visualized in Fig. 1 of our previous work[146] (Chapter 3)– is designed to emulate the critical simulation inputs that influence the computed optical properties. The network employs a total of 8 input neurons: 3 geometric inputs (x_{span}, z_{span}, t_{sub}), the source wavelength (λ), and 4 material inputs (n, k, ε_{real}, ε_{im}). The substrate thickness is a key geometric parameter to consider as it enables the model to interpret the relationship between the spectral optical properties and underlying material thickness and ultimately to predict the broadband spectral behavior of transmissive materials. Micropyramids of different materials are differentiated using discrete material inputs for the complex refractive index (n and k) and the correlated permittivity values (ε_{real}, ε_{im}). Compared to using only n and k, using both the complex refractive index and the permittivity is essential to accurately extrapolate the optical properties of materials not seen

in the training process. The source wavelength (or frequency) is the fundamental factor that links the geometric and material inputs. For each FDTD simulation, we simulate 100 wavelength points (100 frequency points), each of which has a discrete solution for reflectivity and transmissivity. Accordingly, each simulation is divided into 100 discrete input vectors as the solution to Maxwell's equations is not sequentially dependent. To strengthen the connection between the input and the output optical properties (R, T) and the key independent parameter (λ), we utilize two smaller multi-layer perceptron groupings (MLPs) to separately consider the relationship between the geometry/wavelength and the material data/wavelength. The MLPs outputs are concatenated and fed into a larger deep neural network, the output of which is a reflectivity and transmissivity value.

The DNN method is effective at being both quick to predict and in making accurate predictions, even when extrapolating. The DNN surrogate neural network has a mean absolute error (MAE) and mean-squared error (MSE) between the simulation data and predictions of 0.0033 and 1.35e-4 respectively for the "test" dataset – data that is held back from the training/validation process. As the network's design is not limited by constraints in material input, a fundamental evaluation of the surrogate's performance is in the prediction of the optical properties of microstructures made of materials that are outside of the scope of training. Thus, we evaluate the network on two large (1500 simulation) "unseen" datasets Al2O3/Ti, and on 100 simulations of 25 other materials in a "library". When the simulations from these datasets are completely unseen by the training/validation process, the DNN yields an MAE between prediction and simulation of 0.0175, 0.0131, and 0.0279 for the Ti, Al2O3, and Material library datasets respectively. As the optical properties are already on a scale of 0 to 1, these errors indicate an exceptional degree of prediction

accuracy when extrapolating for new materials. To improve the prediction accuracy when extrapolating, the model benefits from small "calibration" datasets. By including 5 – 10 simulations from the "unseen" datasets (< 1%) to the training/validation process of the surrogate, we reduce the prediction MAE to 0.0073, 0.0049, and 0.0118 for the Ti, Al2O3, and material library datasets respectively. The included simulations represent an almost insignificant number of simulations when compared to the original training and validation dataset (< 0.05%). Despite this, the inclusion has a dramatic impact on the remainder of the extrapolated data, indicating the model has strong physical understanding and only several simulations are needed to "calibrate" the model to new material behavior. In addition to the observed accuracy, the model can make predictions exceedingly fast– with over 1 million individual input sets per minute.

Surrogate Neural Network: Convolutional Deep Neural Network (CDNN)

The architecture of a second proposed surrogate method based on image processing is shown in Figure 4-1. Here, we enhance our neural network design philosophy of mimicking the FDTD optical solver by making a network that analyzes a pseudo-mesh. In FDTD, the optical solution for a given combination of material and geometry is derived from solving Maxwell's equations across a discretized mesh[147]. The only way the model can differentiate between two distinct materials (e.g., air and the pyramid) is by assigning the λ-dependent material properties to each cell. Here, we approximate that process by generating an image that utilizes the spectrally dependent material and geometric information. More details for this network configuration and design are discussed in Chapter 4.

This surrogate method is more effective at accurately extrapolating optical properties for new materials when compared to the DNN only surrogate method. When only 20% of the

available simulation data is used in the training/validation/testing process, we can match or exceed the performance of the DNN. The precise performance is dependent upon the selection of the material properties used in the three available pixel matrix dimensions. While the selection of the first two-pixel dimensions (the complex refractive index) is straightforward, the third quantity was a point of study. In table 4-1, we show the performance of the CDNN architecture in predicting the Ti, Al2O3, and material library datasets when different quantities are used in the third matrix dimension. As seen in Chapter 4, despite being more accurate than the DNN, due to the relative increase in parameters and memory scale, the training time and prediction time for the CDNN is significantly longer than the DNN.

5.3.2 Inverse Neural Network

We harness the rapid prediction capabilities of the surrogate network to iteratively train a neural network that solves the inverse design problem. That is, we invert the forward problem to predict what material and microstructure geometry will best match a desired system optical response. The input of this network is the spectrally dependent reflectivity, transmissivity, and emissivity corresponding to a desired wavelength range.

The architecture of the inverse neural network, as depicted in Fig. 1, solves the inverse problem by considering the entire spectral distribution. The network input (400 x 1) is a vertically stacked combination of the predicted reflectivity, transmissivity, derived emissivity ($\varepsilon = 1 - R - T$), and the wavelength vector the optical properties are sequenced to. Correspondingly, the inverse network output is a vertically stacked combination of the geometric input and wavelength dependent material properties (n, k, ε_{real}, ε_{im}, 403 x 1) as visualized in Fig. 1. Unlike the surrogate network, we cannot separate the inputs of an

inverse network into single input vectors. An "inverted" solution for a single set of wavelength dependent optical properties has an unbounded number of potential solutions, so to design an effective inverted network the input must be the entire sequence. In our first design iterations of the deep neural network surrogate, we considered using the entire sequence of wavelengths/material data as an input and reflectivity/transmissivity as the output. While this method was effective, because Maxwell's field equations are not sequentially dependent, the surrogate solver was much more effective when the sequences were broken up and individual vectors based on a single wavelength point were used as an input. This method also dramatically expands the scope of the training set from 35,500 simulations to 3.55 million input sets, making a limited number of simulations more effective in developing a surrogate with physical insight that can solve the forward problem more accurately. Once the surrogate is trained and can produce accurate results, however, the number of simulations becomes trivial, as we can effectively estimate the solutions to 10,000 FDTD simulations (with 100 wavelength points each) in approximately 60 seconds using the surrogate network.

To generate training data for the reverse neural network, we pass in large grids of data to the surrogate network for prediction and collate the output into discrete input and output sets. For each material in a library, we generate a grid of 200 x 200 geometric combinations. These combinations are formed by meshing linearly spaced vectors for the X_{span} and Z_{span}. The minimum and maximum values for these vectors are based on the minimum and maximum observed value of X_{span} and Z_{span} in the surrogate's training dataset. In total, the grid has 40,000 geometric combinations (or 40,000 simulations) for a single material. For each geometric combination we attach a wavelength vector of length 100, leading to a sum

of 4 million inputs per material that are passed to the surrogate. While the wavelength vector attached to each geometric combination was originally a linearly spaced vector that ranged from $\lambda = 0.3$ um to $\lambda = 16$ um, we found that using a linearly spaced wavelength vector with randomized min/max values for each geometric combination increased the versatility of the training dataset and thereby increased the robustness of the inverse neural network. All generated grid data is normalized before being passed into the surrogate network for prediction. The final non-material parameter – the substrate thickness – is also randomized via a uniform random generation process. Details on the random generation process for the substrate thickness and wavelength vector can be found in the methods section. This grid generation process is repeated across all materials in a material library. The material library contains 50 materials: a list of the materials and their references are provided in the Appendix A. The number of materials in the library is easily scalable and are a non-exhaustive representation of material properties available for a microstructure. In total, we use the surrogate network to estimate 2 million simulations, or 200 million sets of inputs. We then sequence the predicted optical properties using the wavelength vector (of length 100) for each simulation.

The inverse network contains three distinct neural network components that are designed to work in tandem to extrapolate a geometry and material that best fit the desired optical response. The first of the components is a deep neural network consisting of multiple hidden layers that directly take in the (400 x 1) input vector. On a rudimentary level, simply inverting the surrogate's DNN structure – but with the progression of wavelengths instead of an individual wavelength point – could be effective. Through our development process, however, we discovered that this more simplistic approach lacked physical insight and

would often result in a non-physically viable output. Although the solutions to Maxwell's equations for a given wavelength, material, and geometry – the problem the forward network addresses – are not sequentially dependent, abrupt changes or singularities in material properties across a spectrum are seldom. Thus, developing insight on the relationship between a sequence of optical inputs and material properties is crucial in building a physically grounded model. To address this, we remap the linear sequence of optical properties into a "time"-dependent matrix and use it as an input to a recurrent neural network (RNN). That is, we map the 400 x 1 vector of (λ, ε, R, T) into a 1 x 100 x 4 matrix (λ, ε(λ), R(λ), T(λ)). We select bi-directional long-short term memory (LSTM) layers as the constituent component to the RNN. LSTM networks are more effective than other RNN methods for long-range dependencies in data[167], and the bi-directional attributes enables the network to learn both dependencies in the forward and reverse direction. Additionally, we utilize dropout layers between LSTM layers in conjunction with L2 regularization to reduce overfitting. The outputs of the RNN and DNN components are then combined using a matrix multiplication and fed into a third component, another DNN. As opposed to directly linking the network output to the final DNN/RNN layers, a DNN between these two networks and the final network output facilitates an additional layer of non-linear abstraction and learning from the outputs of the two preceding neural network components.

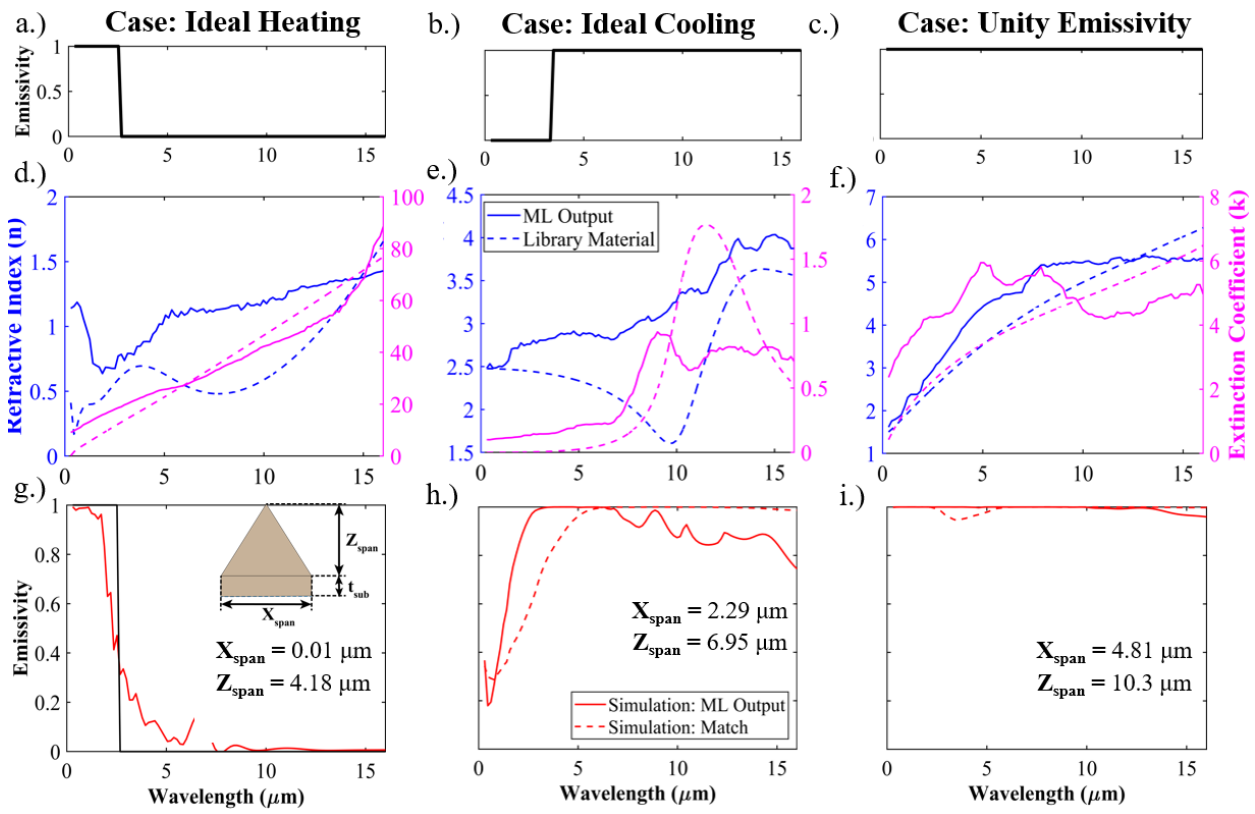

Figure 5-2 (a-c) Emissivity spectrums of three test cases (Ideal heating, ideal cooling, and unity emissivity) input into the inverse spectrum. The reflectivity is computed as R = 1 – E, and transmissivity is set to 0. (d-f) ML generated refractive index (n) and extinction coefficient (k) for each of the test cases compared to the material properties of a material in the library that most closely matches it. (g-i) FDTD simulation results for both the ML generated material and the closest matching library material

Figure 3 shows the output of the inverse neural network for several broadband test inputs and results once the network outputs are simulated in FDTD. We utilize three thermally relevant test spectrums as a baseline evaluator of the inverse network – unity emissivity, an ideal heating emission spectrum, and an ideal cooling spectrum. These emission spectrums are shown in Fig. 3(g-i). For these test cases, we set the spectral transmission to be 0 and R

= 1 – ε. In Fig. 3(a-c) we compare the material properties predicted by the neural network to the material properties of a material in the library that best matches it. The predicted geometric conditions are given in Table 2. For all cases, the projected material properties have a close match in the library. In Figure 3(d – e) we compare the results of FDTD simulations using the network generated material and the closest match material for the same predicted optimal geometry. For both the heating and unity case, we observe that the neural network generated material outperforms the library material. Additionally, we note that both the generated material and the library material produce a result that matches the desired input to a high degree of accuracy. This is despite the input having a non-physical step-function behavior. The observed error is attributed to the physical limitation of material properties and the imposition of zero spectral transmission. This assumption is outside of usual physical intuition for the ideal cooling case, where due to the physical material limitations, most emissive materials (e.g., TiO_2, Al_2O_3, PDMS, etc.) in the infrared are transmissive in the ultraviolet (UV) to NIR wavelengths. Thus, this represents a design challenge for a single material to perform both functions, and the inverse neural network attempts to abstract a physically bounded material that fits zero spectral transmission. The identified properties match well across the broader spectrum but do not capture the intended performance in the visible to near infrared regions (λ = 0 – 4 um). If we allow transmission in this region, we receive an expected output of PDMS, as is shown in Figure 5-3.

Case	Closest Material Match	Xspan (um)	Zspan (um)
Unity Emissivity	C (Graphite)	4.81	10.3
Ideal Heating	Li	0.01	4.18
Ideal Cooling	Si_3N_4	2.29	6.95

Table 5-1 Library material that most closely matches the ML generated material output n and k in addition to the predicted geometric parameters

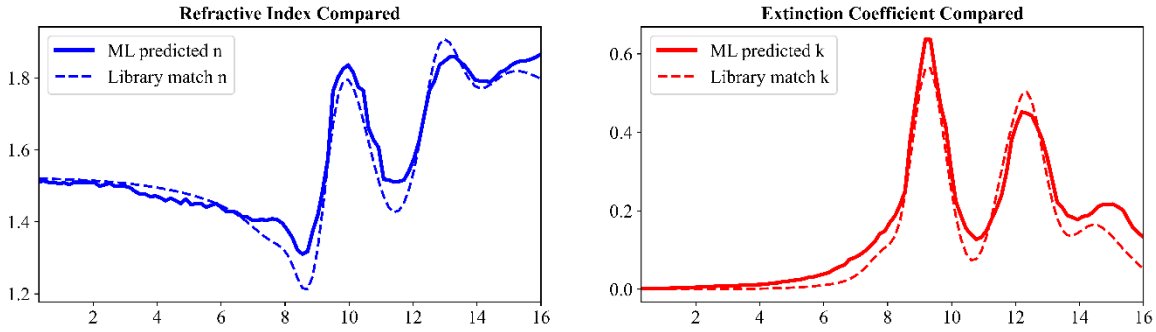

Figure 5-3 (a) Refractive Index and (b) Extinction coefficient output by the inverse neural network when the ideal cooling case has a transmission of T = 1 – E and R = 0. The material outputs nearly identically match those of PDMS, plotted with the dashed line.

The inverse neural network is not limited to broadband design. In Figure 4, we show how the inverse neural network can be applied to narrowband microstructure design. In this case, we define narrowband as 2 emissivity points with a unity value around the intended wavelength peak. The inverse neural network results for 6 different wavelength points (1, 2, 3, 4, 5, and 15 um) are shown in Figure 4(a-f). The design outcome highlights both the strengths and weaknesses of the presented inverse neural network methodology. The geometric design space is limited to the relatively simple micropyramid geometry and can

only utilize one material. Thus, with the implemented neural network architecture, our model stays within constrained and physical material behavior, attempting to find valid solutions without creating a completely arbitrary material. This leads to valid narrowband solutions in the low wavelength regions where geometry can be attenuated to generate plasmonic resonance and resonant behavior. This behavior is particularly evident in the solutions visualized in Figure 4(c) and 4(d), with peaks at or near the desired location, albeit with either reduced performance or peaks beyond the desired location. The neural network can readily identify solutions that are physically feasible, but is challenged to find resonant behavior that results in narrowband solutions for the mid-infrared wavelengths. These plots result from the both the physical limitations imposed by the input, the training data available to the network, and the fundamental physics of the micropyramid system. Despite these challenges, the inverse network still can be shown to identify physical behavior outside of the scope of its training data. In Figure 4(d), the surrogate model's predictions do not indicate resonant narrowband behavior at 4 um, but when simulated the inverse neural network output shows a significant degree of narrowband performance. This indicates that the reverse neural network can abstract solutions beyond the training data and identify behavior that the surrogate cannot, but the network is still constrained by the fundamental physics.

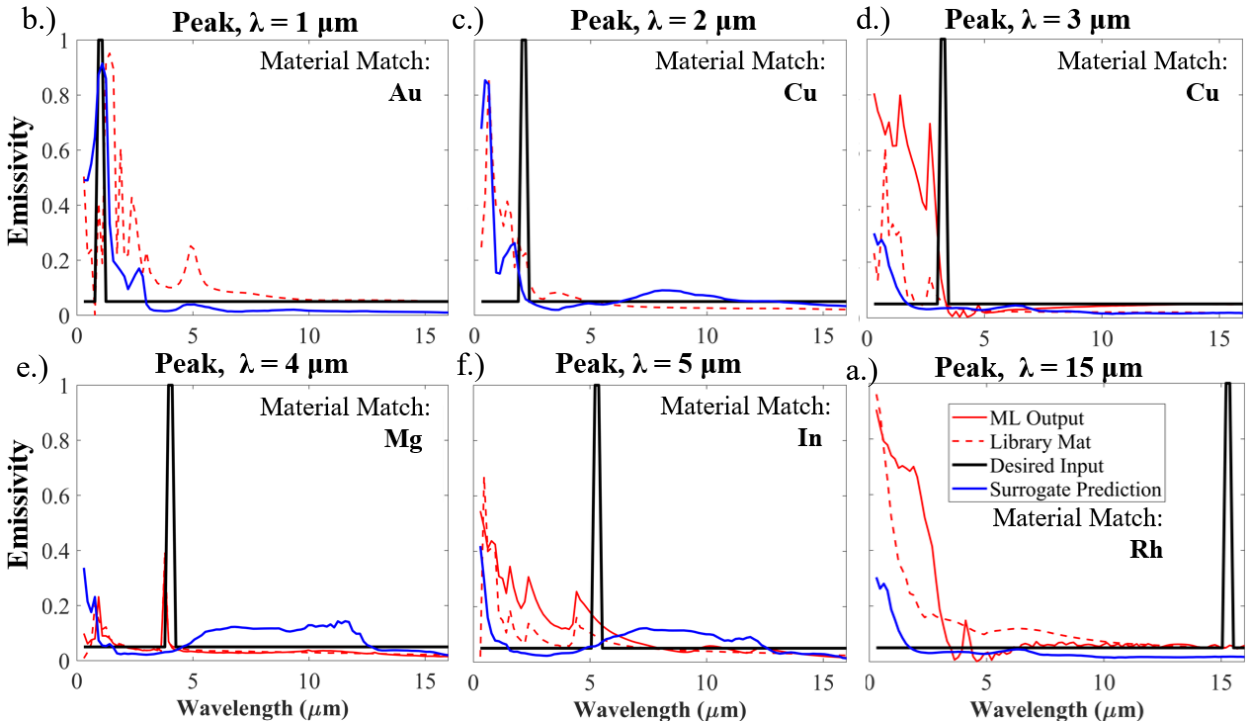

Figure 5-4 (a-f) Narrowband simulation results using the inverse neural network. The input spectrum has an emissivity of 0.05 throughout the λ = 0.3 to 16 um, except for two points that define the "peak" location which have an emissivity of 1. The reflectivity is defined by E = 1 – R and the transmission is set to 0. The results are compared to the desired input as well as the surrogate predictions for the same material

Peak	Material Match	X span [μm]	Z span [μm]
1 μm	Au	2.911	6.902
2 μm	Cu	3.108	1.429
3 μm	Cu	2.57	6.959
4 μm	Mg	3.791	4.614
5 μm	In	4.426	1.578
15 μm	Rh	5.041	2.814

Table 5-2 Library material that most closely matches the ML generated material output n and k in addition to the predicted geometric parameters for select narrowband peak

Post-Processing: Constraints and Solution Viability

While the inverse neural network output can accurately predict material and geometric properties that result in the desired optical spectrum, a key limitation of our open-ended neural network architecture is that it cannot directly accommodate design constraints. This presents a significant challenge in making the inverse design process functional. Ideally, our aggregated network will output a solution that is translatable to a fabricated surface morphology. This challenge is evident from the geometric results for the ideal heating case in Table 2; the aspect ratio of the ML predicted structure is ~ 400 (Zspan/Xspan), which is clearly an impractical microstructure. To address this, we take the output of the neural network and use a post-processing methodology to provide new solutions that fit within user set constraints. Though it is possible to constrain the neural network itself via methods such as custom activation functions on the output neurons, limiting the input dataset, or introducing limits in the input, we choose to post-process the neural network output to maintain a robust inverse solver. For this work, we focus on constraining the aspect ratio as it plays a key role in determining if a microstructure is manufacturable. Other constraints, such as a material's maximum temperature, thickness limitations, etc., are important and can be easily incorporated for more advanced design optimization.

The post-processing methodology has several stages: inverse prediction, material matching, geometric adjustment, surrogate prediction, simulation, and finally output comparison. Precise details for all the stages of the post-processing method are provided in the methods section. The first stage is to take an optical spectrum, pass it through the inverse network, and output a set of geometric properties and spectral material information. From there, the

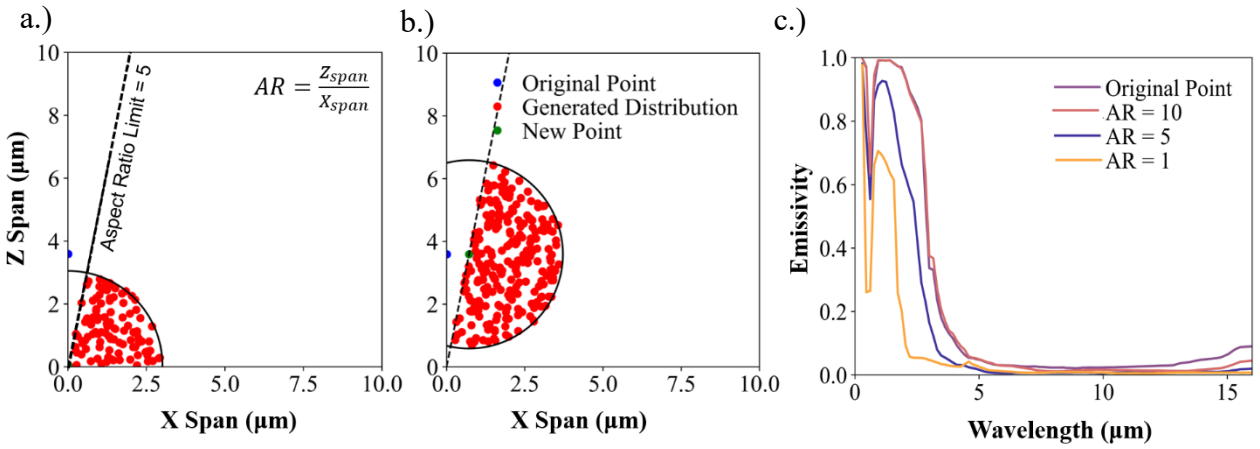

Figure 5-5 (a) Example of vertical and (b) horizontal reorientation of inverse ML output and subsequent generation of randomly distributed solution points about the adjusted geometric solution. Example shown is using an aspect ratio limitation of 5. These solutions are evaluated using both FDTD and the surrogate, the most optimal new solution is using a process described in the methods section. (c) The identified optimal point at each aspect ratio is shown for each aspect ratio. While the solution is not as optimal as the original ML generated geometry, the we can still identify geometric designs with exceptional performance.

ML generated material data is compared to existing materials in the material library. We then adjust the ML generated geometry to align with the set maximum aspect ratio. Using the adjusted geometry, we randomly select new constrained/viable geometries and simulate them using the surrogate; the most optimal solutions are passed to FDTD. The post-processing method then compares the "ground-truth" FDTD to both the surrogate output and the desired input. This process is performed for both the ML-generated material and "best-fit" library material and identifies a constrained geometry that is optimal for both the ML-generated material and selected library material.

Figure 5(a-b) shows the post-processing method's application to select a new viable solution for the ideal heating case discussed above. For this demonstration, we show solutions when the aspect ratio (Z/X) is limited to 10, 5, and 1. The new geometric solutions

are simulated using the surrogate, and the results are compared to the predictions for the unconstrained ML generated geometry. Compared to the desired input spectrum, the constrained cases have an LSE value of 1.229, 1.396, and 1.567 for AR = 10, 5, and 1 respectively. It is evident that while the results decrease in adherence to the desired spectrum as the aspect ratio is limited, it is also evident from Figure 5(c) that the adjustments to the geometry to accommodate the limited aspect ratio constraint still yield highly optimal results. It is evident that these solutions deviate from the global maximum but are still highly effective when constrained. If the constrained solution is deemed to not be viable enough, additional materials can be included in the search, forming a more advanced material search algorithm than previously utilized[116], [146].

5.3.5 Aggregated Neural Network

By combining the individual components, we form the aggregated system loop visualized in Figure 1. The aggregated system is designed in a way that it can learn from previous mistakes and enhance its capabilities and accuracy over subsequent generations. Despite the accuracy of the image-based surrogate, especially for unseen materials, the time required to train and retrain the image-based convolutional network compared to the simpler deep neural network surrogate eliminates it as an option for the aggregate system. The geometric/wavelength simulation grid data generated for each material is passed into the DNN surrogate and the ensuing predictions are the basis of the inverse network training data. If changes are made to the surrogate or more materials are included in the library, the grid data will be regenerated. We then employ the broadband and narrowband test cases in Figures 3 and 4 to test the performance of the inverse network in making predictions. If either significant deviations between the desired result and actual result are encountered or

the surrogate prediction deviates significantly from the FDTD results, we perform additional simulations via our post-processing solution generation method. These results are incorporated in the training data for the surrogate, and the surrogate/inverse network are retrained. Post-processing, then, serves an additional function as a pseudo-adversarial checkpoint where the generated results are compared to true results and if there is an undesired outcome the network is retrained with new simulation information.

5.4 Discussion

A core challenge facing the design of microstructures is the time required to simulate and optimize a design. For the first component, in stark contrast to an FDTD solver, a neural network can make predictions comparatively instantaneously. The generation of the ~ 40,000 FDTD simulations used to train, test, and evaluate our surrogate network required months of computational time, whereas the surrogate network can predict a 40,000-simulation grid (4 million sets) in approximately 4 – 5 minutes. The DNN surrogate network can predict a 100-wavelength point simulation in approximately 6 ms, representing a 4 to 6 order of magnitude speed increase compared to using the FDTD solver for the same task. Considering the demonstrated accuracy of the network across a library of materials, this method is highly effective in substantially reducing the need for complex optical solvers to estimate spectral optical properties across a large material library. As previously demonstrated, once the model has a connection to the physics of the problem, very few simulations are required to "calibrate" the model to new materials. Our DNN surrogate only requires an average of 5 – 20 FDTD simulations to be included in training per material to bring the prediction error for that material to near to the rest of the dataset.

The core advantage of the surrogate network compared to FDTD simulations – speed – is leveraged in this work to build a comprehensive dataset for training an inverse solver that aims to address key challenges in design optimization. In our previous publications, we addressed optimization using a thermal figure of merit and a "brute force" search optimization method. That is, we designed an objective function to describe a desired spectrum and use the FDTD or surrogate optical output to solve the thermal equations and then use the objective function to determine which spectrum most optimally matches the input. This method, clearly, is incredibly slow and cumbersome. Using a neural network to perform the inverse task – much like the forward solving network – is orders of magnitude faster than this approach. The speed difference relies on the fact that the inverse neural network can learn the pattern between the optical properties and material/geometric properties, and directly take in a spectrum and output a material/geometry that suits it. Rather than a roundabout methodology that relies on identifying the best spectrum using grids of surrogate generated data across multiple materials, the inverse network trains on those grids and provides a user with a nearly instantaneous output to a selected spectrum. This method also opens the door to non-intuitive solutions as we can potentially identify new materials that are not in the material library.

Determining the appropriate surrogate method to generate the training data for the inverse data is an important consideration in the design of the aggregate system. Ultimately, due to the large grids of data used to generate the training data and the training/retraining process, the inverse network necessitates a fast surrogate. The DNN methodology, as compared to the CNN, is significantly faster in making predictions and in training. When trained on the full dataset, the image-based approach can require hundreds of hours to train

using our computational resources. Comparatively, the DNN can train on the entire dataset in approximately 25 – 50 hours. Additionally, the prediction time is significantly longer for the CDNN, making the generation of simulation data to train the inverse network far less efficient. While the CDNN method is more accurate, the incremental accuracy increase we observe does not justify the time cost in this case. We could reduce the size of the images used by the CDNN to speed up the network training and prediction times, but then we would lose spatial resolution and have to eliminate a greater quantity of simulations from consideration. The efficacy of the CDNN will be more apparent in future work that relies on more complex structures. The images used as an input are not specifically bound to a single geometry, and a CDNN surrogate could be constructed that solves the optical properties of different geometries or even abstract shapes. This could also include multiple geometries, hierarchies, or even structures that include multiple materials such as coated structures or composite structures. In addition to these options, a CDNN could be also converted into a tandem inverse solver with a generative network. Ultimately, while the micropyramid geometry we show in the present work is relatively simple and does not necessitate the image-based surrogate to train the inverse network, potential future options for complex inverse neural networks based on an "image derived mesh" are boundless.

The primary strength of the inverse neural network design – its ability to generate a unique set of spectral material properties – leads to significant design and implementation challenges. A core concern in the design of the network is determining how to balance a desire to remain physically bounded while also enabling the model to find ways to extrapolate in new and unique ways. A simple approach would have been to simply one-hot encode material classifications, thereby eliminating non-physical material outputs. This

approach is undesirable as it not only eliminates the ability to extrapolate new materials, but it also significantly reduces the ability to explore different materials in post-processing. As demonstrated, the model generated material properties can outperform the materials in the library. As the scope of the surrogate and inverse network continue to expand, more materials are added, and more simulations are performed, we expect that the inverse network will not only increasingly outperform existing materials but could be used to identify "effective" refractive indices and reverse engineer material combinations that match it. These strengths are lost with rigid material classification, and to maintain a robust solver we designed the network to accommodate material outputs that are only bounded by the arbitrary list of materials used to generate the training data.

The design choice to allow the network to choose discrete material properties – as opposed to classification – does lead to significant challenges and necessitated design compromises. Early iterations of the inverse network design utilized a single DNN with a single vector (400 x 1) input, but we found that the output would often be non-physical or unrealistic. Thus, to ground the model from pure abstraction of material properties, we implemented a sequential method utilizing an RNN to ensure that the model could learn the forward and backward relationships of the material properties. This enables the model to have a certain level of physical insight into how materials usually look, so that when it generates the output the output should resemble, but hopefully surpass, the performance of microstructure made of the "best-match" material in the library. Additionally, our network's early construction only considered the emissivity as an input. Over subsequent model iterations, however, we found that the inclusion of the two parameters that determine the emissivity – the reflectivity and transmission – enabled not only more control for the user,

but also additional reinforcement in the model's ability to abstract physical relationships between the material properties and input spectrum.

An important consideration is the impact that geometry has on the optical properties and thereby the thermal performance compared to an untextured surface. The materials generated and identified through the neural network process conform to physical intuition for each of the test inputs. While this intuition may be sufficient for a material search algorithm, the application of optimized texture further enhances absorption and improves the thermal and optical outcome for a system. This is particularly true for the Ideal heating input shown in Figure 3(a), where optimal texturing leads to a surface that can absorb over 98% of incident solar radiation, compared to approximately 15% when the surface is untextured. While untextured (completely smooth) graphite of < 100 um thickness has an emission efficiency of ~ 33.5%, ML identified optimal texturing increases the emission efficiency to ~ 99.6%. Texture has a more minimal impact on Si_3N_4, raising the emission efficiency from ~ 75.6% to 99.9%.

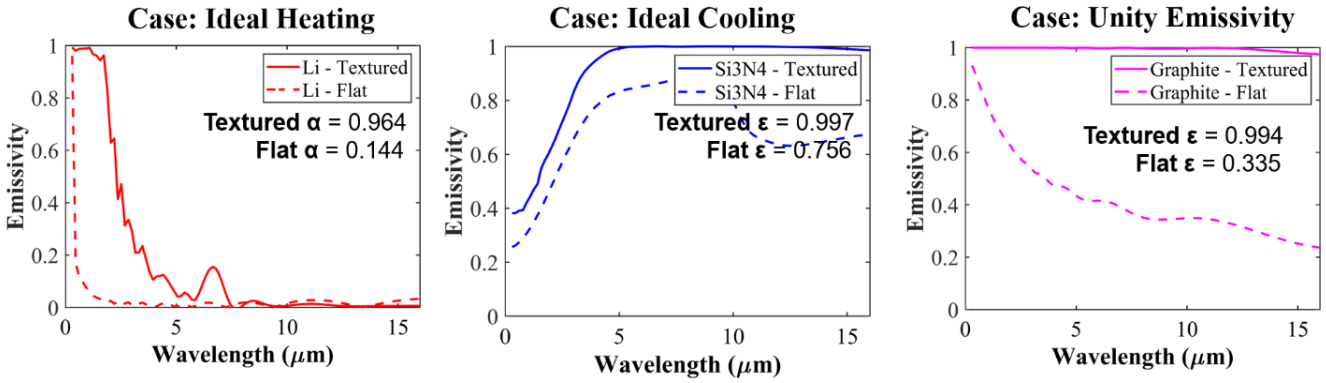

Figure 5-6 Comparing untextured materials to the optimized counterparts. The absorption value is computed as the amount of solar radiation absorbed compared to the maximum solar radiation available. For both the ideal cooling and unity case, the emissivity is computed as ratio of the surface emission vs the maximum emission.

	Absorption Efficiency	Emission Efficiency	Power Absorbed	Power Emitted	Emissivity Deviation from Input (MSE)
Flat					
Graphite	0.8176	0.3356	817	93.57	0.3658
Li	0.1438	0.0161	144	4.5	0.1256
Si3N4	0.3069	0.7557	307	210.7	0.092
Textured					
Graphite	0.9999	0.9943	1000	277.3	6.62E-05
Li	0.964	0.0225	964	6.26	0.0155
Si3N4	0.425	0.9969	425	277.98	0.0656

Table 5-3 Comparing untextured materials to the optimized texturing demonstrated in the main text. Texturing has a significant impact in some cases, but the transformation is most apparent in the case of the reflective metal turned into a solar absorbing material (Li). Power is presented in terms of W/m^2.

Several key issues arise from the selected network design. The first is in identifying and subsequently correcting any mistakes made by the inverse neural network. Due to the open-ended design of the material outputs and the large variability in the inputs, it is very easy for a user to specify a non-physical input that can result in the network making a valid approximation for much of the broadband spectrum but missing a key narrow portion of the spectrum. This is particularly apparent in the narrowband case shown in Figure 4 where a large broadband wavelength input is used in conjunction with a non-physically intuitive spectrum for a single material microsystem. This design challenge necessitated switching from only broadband wavelength inputs (0.3 – 16 um) in the training data to randomizing the wavelength/material vector passed into the surrogate. Still, results still demonstrate that the model will attempt to solve the problem but of course cannot correct a user's input. It

should be acknowledged that the network is trained using physically bounded and sequential results, so abstracting a solution for what could be a non-physical desired spectrum should not be expected to have a high degree of accuracy. A second related challenge comes from the material data pathways and generation methods. The FDTD method relies on curve-fit data based on experimentally sampled measurements. Our network builds a cubic-spline fit model based on FDTD generated material data. When we want to simulate the neural network generated material properties, we need to pass it into FDTD in the same way physical measurements would be. This can lead to some fundamental challenges in curve-fitting and automation, as the FDTD curve fit for ML generated data may be completely incorrect and require manual intervention. This process also limits our options to use ML generated data in the aggregated system training loop. If the actual properties deviate from the inputs, incorporating the data could lead to significant prediction inaccuracies. For future modelling efforts with more advanced systems and multi-material composites, very careful interpretation and interpolation of material properties will be required to properly represent and predict new materials.

Another challenge is to constrain the output based on user set limits. Potentially applicable constraints are plentiful, but for this work we focused on constraining the aspect ratio as it is a crucial element in determining the manufacturability and scalability of a microstructure. We presented a solution to both key issues by introducing a post-processing module. This module is not a neural network, and it operates outside of the "black box" of neural network design and can be more easily adjusted to account for real scenarios using the optimal output provided by the inverse network. An apparent shortcoming to neural network design is in understanding the ever-increasing complexity of non-linear abstraction

that occurs inside of the "black-box" of the hidden layers. While we could introduce limitations on the network, add new variables, etc., to account for the constraints, this may not only reduce the robustness of the architecture but also could make it difficult to supplement or adjust the solution with physical insight.

In effect, the post-processing module takes the role of a both an adversarial checkpoint as well as a local-minimum optimization method. If the imposed constraints are violated, the post-processing module infers new solutions and determines which of these are most optimal. Of course, this method could be used in the same "brute-force" manner that we utilized in previous publications[116], [146], [164] to determine a local minimum optimal solution from the surrogate, particularly if it was combined with a gradient-descent optimization method. However, this has the same issues as the previous approaches in that the result is not only likely to be a local minimum, but that we would be required to repeat the process for every material in the library. The aggregated system is designed to leverage all the modules to automatically learn and correct the networks if an incorrect prediction is made by either the surrogate or inverse network. By generating new solutions, simulating them, and then comparing and simulation results to the surrogate results and desired input, a decision can be automatically made to include the simulation data in a subsequent loop of data generation and model training. This process is directly transferable to any microsystem design, and for more advanced iterations that include additional limiting parameters such as temperature dependence and temperature dependent material properties. The unbounded nature of the entire loop also unlocks unique perspectives and solutions that would otherwise be infeasible.

5.5 Conclusion

We have demonstrated a platform that can output discrete and unique material and geometric properties that will lead to an input optical spectrum. The models are not rigidly constrained by material classification, and the network can be used to identify the material properties that would best solve the problem. The inverse solver enables the design of a material search algorithm that can identify what materials are best suited to match a desired optical response based on user set constraints. Furthermore, the inverse network input is not limited to a preset input wavelength vector, enabling the dynamic exploration of narrow band and limited wavelength solutions in addition to more traditional broadband inverse optimization. As a part of the platform, the exhibited post-processing method takes the output of the inverse neural network, removes it from the black box of neural network processing, and allows for adjustments to the neural network output based on set constraints. The post-processing section also serves as an adversarial node to the combined system, connecting to the FDTD simulation source and introducing targeted simulation data to improve the neural network in subsequent generations. While we only use the deep-neural network derived surrogate solver as a part of this process, the image-based method we developed could play a pivotal role in future iterations of inverse design networks for more complicated microstructures or multi-material systems that cannot be simply represented in a deep-neural network. Our methodology not only effectively replaces FDTD simulations for micropyramids, but it also enables near instantaneous inverse-design and optimization, allowing for near instantaneous complex and comprehensive design optimizations.

Chapter 6 – Nanometer-Thick Nickel Coatings for Increased Infrared Emission

The anti-reflective properties induced by texturing the semiconductor surfaces based on the well-known semiconductor processing have been extensively investigated and widely applied for solar cell applications[27], [168], [169], where the textured Si, or black Si[24], [25], has demonstrated excellent anti-reflective performance. Similar textures can be patterned[170] into metals[16], [37], or polymers[38] to engineer the optical and thermal response for different wavelength spectra. Combining anti-reflective textured surfaces with a coating material – forming a "core-shell" structure – has been exhibited to significantly enhance the absorption characteristics[47] by means of plasmonic resonance[171], [172] and the introduction of new optical modes[173] including Fabry-Perot resonance similar to that of a resonant chamber[174]. More recently, the combination of a metal coating with textured Si has been shown to significantly improve visible (VIS)/near-infrared (NIR) light absorption[165], [175].

The ability to engineer the absorption of light is fundamental to systems that depend on the absorption or emission of thermal radiation from the exposed surface. The optical properties of micro and nano-textured silicon, however, cannot be modified much by texture alone beyond the visible wavelength spectrum due to material properties of silicon in the infrared wavelengths. While some studies have shown that Si nanowire texturing can have an impact on infrared transmission[41], [45], the infrared transmission drop can be both small and difficult to precisely control. Silicon micropyramids with additional hierarchy[45]

and coatings[34], [165], [175]–[177] have also been shown to enhance anti-reflective behavior, but the enhancement is confined to the visible to near-infrared spectrums.

To design effective thermal management solutions for beyond-solar and high-temperature applications such as thermophotovoltaics (TPVs)[7] and high-temperature cooling systems, the engineered surface must be tunable across the mid-infrared (MIR) spectrum as well as the VIS-NIR specturms[116]. Nickel nanopyramids can be used to enhance the absorption profile in the VIS/NIR but the metallic texture has a negligible impact on the mid-infrared optical properties of the surface[16], wavelengths that are essential for applications such as radiative cooling[38], thermal management[116], TPVs[7], and microbolometers[178]. Au coated Si micropyramid textures have been shown to enhance the absorption of photons up to the near-infrared[165], but the optical properties of Au are not conducive to enhancing the MIR optical properties, and thus Au coatings cannot offer the tunability required for most thermal applications.

In this chapter, computational and experimental findings of wet-etched silicon wafers that have been coated with a nanoscale layer of nickel are shown. We first explore the optical tunability and rationale of nanometer thick nickel coated micropyramids using 3D Finite-Difference Time Domain (FDTD) simulations. We then subsequently show our fabrication process, relying on potassium hydroxide (KOH) etching and metal-assisted chemical etching (MACE) processes to fabricate our microtextured and nanotextured surfaces. Finally, we demonstrate the infrared enhancement and optical tunability that is possible by combining nanoscale thick layers of Ni on microtextured (M-Si) and nanotextured micropyramid (N-M-Si) silicon. Optical measurements establish that the combination of the nano-layer of nickel

with the silicon texture enables an absorptivity of 0.6 to 0.7 in the MIR for 20nm nickel coated on the nanotextured micropyramid silicon.

6.2 Effects of Nano and Microtexturing in Si combined with a metal coating

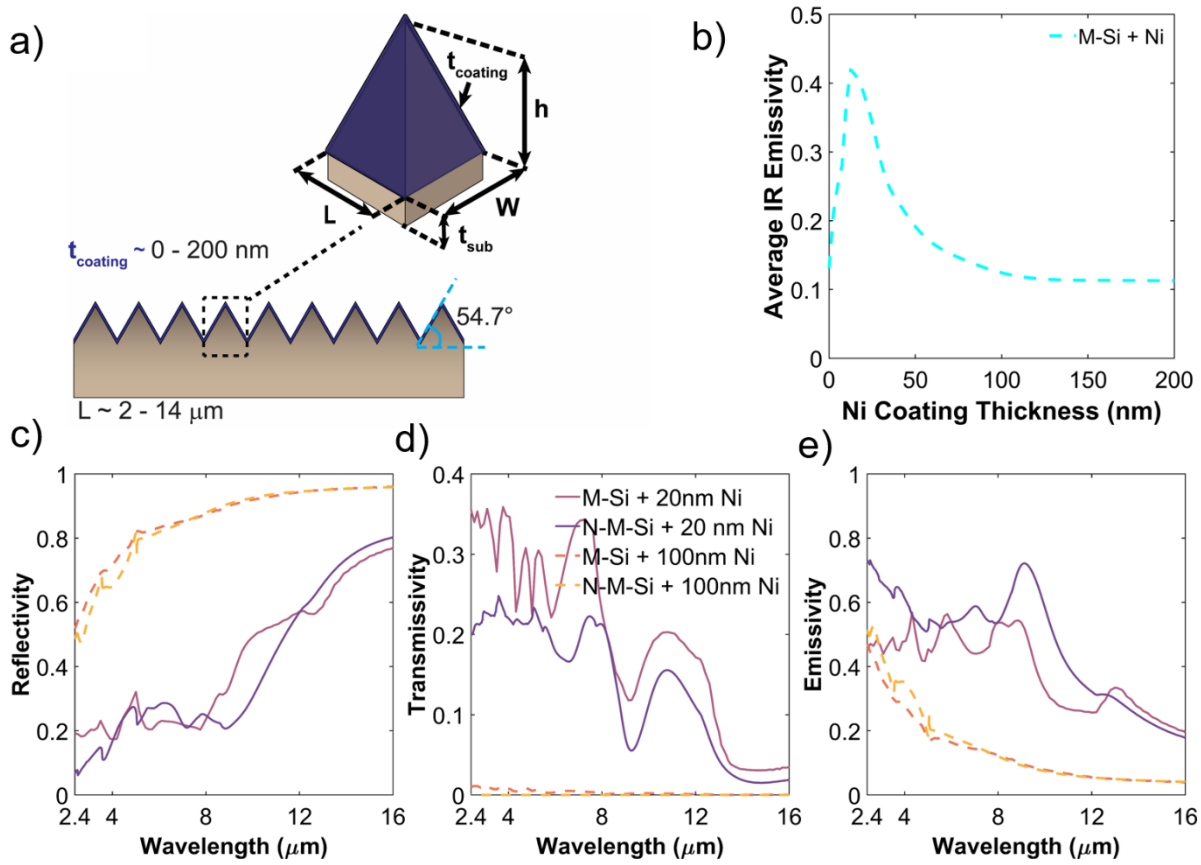

Figure 6-1 – (a) Schematic visualizing FDTD unit cell. We assume periodic boundary conditions to simplify the simulations. We use (L, W, h) = (6, 6, 4.8) um with a 50 um Silicon substrate for our simulated unit cell. (b) Simulated Average Emissivity vs the Ni coating thickness for Ni coated micropyramid textured Si, the value plotted is the average emissivity ($\frac{\int \epsilon(\lambda) d\lambda}{\Delta\lambda}$) from 2.4 – 16 um as computed by FDTD, where λ is the wavelength and ε is a function of the wavelength.(c-e) Comparison of FDTD Simulations for 20 nm (solid line) and 100 nm (dashed line) coated M-Si and N-M-Si.

The texture proposed is represented schematically in Figure 6-1(a). We perform simulations using the periodic unit cell visualized in Figure 6-1(a) in Lumerical's commercially available FDTD. Details on the simulation domain and process are found in previous chapters. A key assumption made in the simulations is that the random and aperiodic topography generated by the chemical etching process(es) can be simplified to a singular periodic unit cell in simulation. This simplification is justified by comparing large domain periodic simulations to a single pyramid unit cell as described previously. Additionally, a limitation is that our simulations are in 3D, so we can only simulate a limited thickness of the silicon substrate. This will lead to a deviation in the transmission of the sample from the measured transmissivity[45]. While the assumptions will lead to deviations in the magnitude of the simulated optical properties when compared to the measured properties, the trends observed with respect to the nickel thickness are consistent with experimental results.

Based on our simulations, we exhibit in Figure 6-1(b) that there is a convex relationship between the thickness of the nanoscale nickel coating and the average infrared emissivity. The average emissivity is computed from simulations over the wavelength of λ = 2.4 - 16 μm assuming Kirchhoff's law is valid; that is, that the emissivity and absorptivity are interchangeable and $\alpha = \varepsilon = 1 - R - T$. Due to the near zero extinction coefficient of Si in the infrared[69], transmission dominates the optical response of uncoated M-Si, resulting in an average IR emissivity of 0.11. By introducing a nickel coating transmission through the texture's surface is significantly reduced, leading to an increase in the predicted absorption. The increase in the average IR emissivity continues until an inflection point near a nickel thickness of 15 nm. Beyond a thickness of 15 nm, the average emissivity is predicted to

decrease with the nickel thickness. This behavior is the result of an interplay between the thickness of the metallic layer and the semi-conductor substrate. For nickel coatings less than ~ 100 nm, there is a significant degree of partial electromagnetic penetration through the coating. The partial penetration of the radiation is combined with the geometrically induced anti-reflective properties of micropyramids, and results in additional optical modes beyond antireflective behavior. This simultaneously reduces both reflection and transmission and leads to an increase in absorption.

Detailed electromagnetic field visualizations comparing microtextured silicon with 20 nm and 100 nm nickel coatings are shown Figure 6-2. Primarily, from Figure 6-2(a,c) it is evident that the 20 nm of Ni allows for a significant amount of the incident radiation to enter the micropryamid texture. This is opposed to the results from Figure 6-2(b,d) which show that 100 nm of Ni are effectively enough to deny most of the electromagnetic transmission through the texture. Comparing Figure 6-2(c) and 6-2(d), the intensity of the electromagnetic field is 2 – 3 orders less for the 100 nm Ni coated Si micropyramid when compared to the 20 nm Ni coated Si micropyramid. The effect of the partial transmission is to enable internal refraction and reflection of the electromagnetic field which leads to the demonstrated increase in the infrared absorption. The transmission into the 20nm M-Si continues throughout the infrared and matches the predicted increased absorption in this spectrum.

Additionally, we observe that for a coating thickness greater than 100 nm, the optical properties resemble the optical properties of pure nickel micropyramids, indicating that fabricating completely metal micropyramids might not be necessary to achieve the same

optical properties. We can also conclude that coating additional material beyond 100 nm will not have a significant impact on the optical properties.

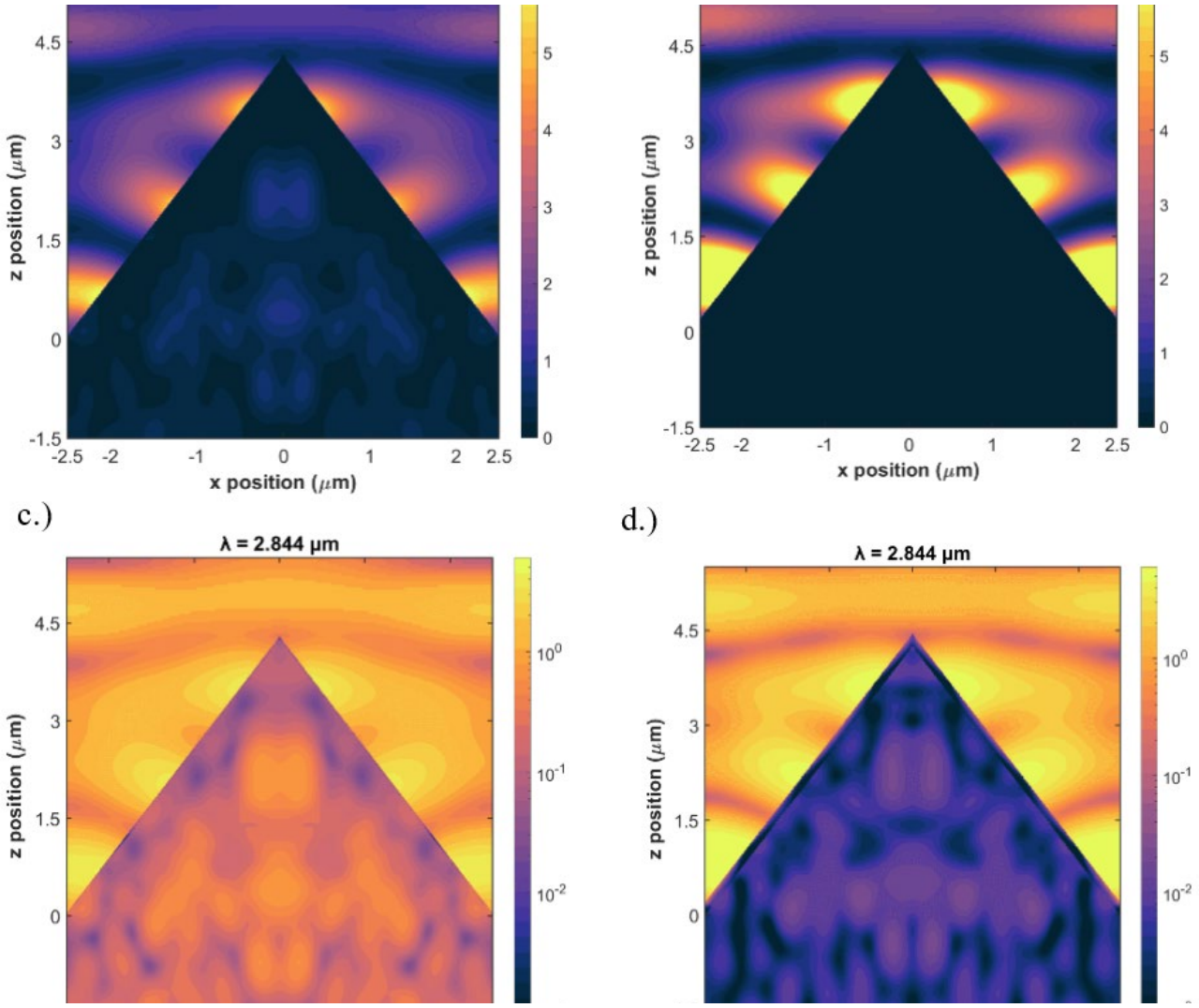

Figure 6-2 (a) Cross-sectional view of Micropyramid Si (M-Si) with 20 nm of Ni and (b) M-Si with 100 nm of Ni with a linear scale for the electric field (V/m). (c) M-Si + 20 nm Ni and (d) M-Si + 100 nm Ni are plotted with a log-scale (V/m). The animation depicts the electric field from λ = 1 – 10 um. The electric field permeates the M-Si with 20 nm of nickel due to partial transmission through the Ni coating, and the electromagnetic interactions inside the pyramid lead to a significant increase in the absorption throughout the infrared spectrum.

To understand how additional nanotexture might influence the optical properties of the coated micropyramids, we compare simulations of the M-Si and N-M-Si in Figure 6-1(c-e) for nickel coatings of 20 nm and 100 nm. The results indicate that additional nanoscale texturing can result in further emissivity enhancements in the infrared and significant tunability of the infrared optical properties. We model the nanotexture as periodic conformally coated cylindrical nanowires, so it is expected that the highly random and clustered nature of the textured hierarchy leads to significantly higher anti-reflective behavior than the model's prediction.

6.3 Experimental Process

6.3.1 Sample Fabrication

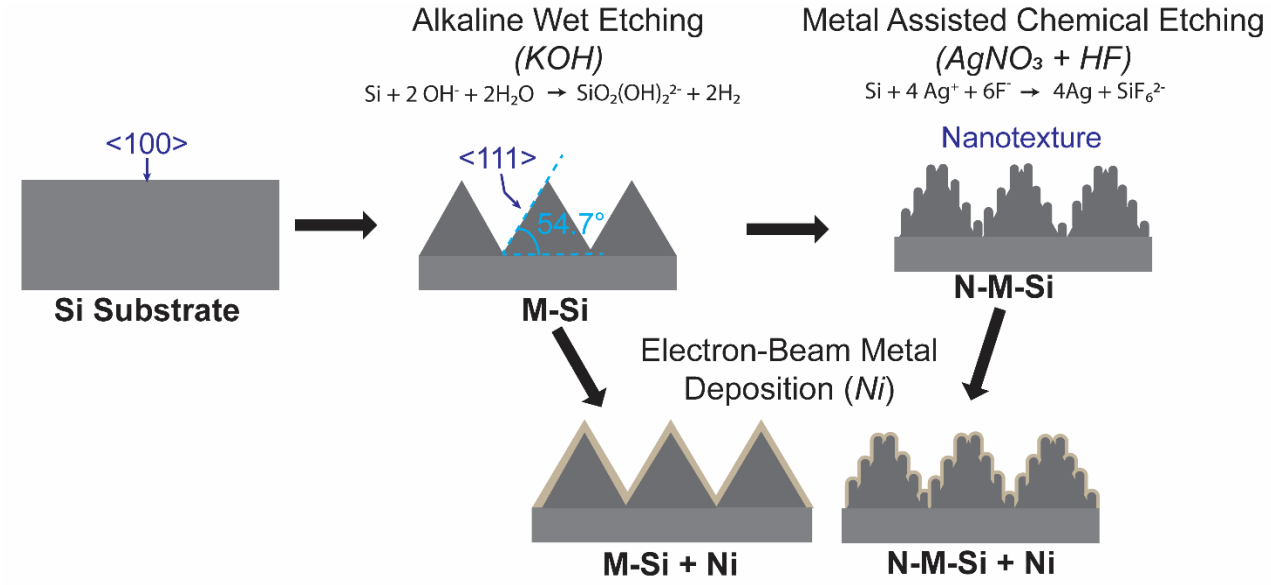

Figure 6-3 Schematic of major fabrication steps for micropyramids (M-Si) and nanotextured micropyramids (N-M-Si). A KOH wet etching process is used to develop the M-Si surfaces, and an additional Metal Assisted Chemical Etching process is used to generate the additional nanotexture on the M-Si. The nickel coating is applied to the surface with electron-beam deposition.

The micropyramid textured Si samples were prepared with an alkaline wet etching process and fabricate the nanotextured Si samples by subjecting the micropyramid textured

Si to an additional metal-assisted chemical etching process[52], [179], depicted in Figure 6-3. Electron beam deposition was used to coat the textured silicon surfaces with a nanoscale layer of Ni. The electron beam deposition was performed at low deposition rates to ensure the film quality. The deposition was performed at low deposition rates to ensure both the film quality and to minimize deposition temperature. The entire process is visualized in Figure 6-3. Specifically, the micro textures (i.e., randomly distributed micro pyramidal structures) were etched in an etchant composed of 3 wt% KOH, 10 vol% Isopropyl alcohol, and 500 ml deionized water at 70 °C for 60 minutes. As observed in Figure 6-4(a-d) the resulting aperiodic micropyramids have a base span that ranges from 2 to 14 um, with a height that is dependent upon the base length. The pyramids have a process determined fixed base angle of 54.7°. To pattern additional nanotexturing, the micropyramid textured Si was etched in hydrofluoric acid/$AgNO_3$/DI water solution for 6 minutes at room temperature. Subsequently, the nano-textured micropryamid sample was transferred to Nitric acid to remove the Ag particle residual. The micro- and nano-textured micropyramid Si samples were then coated with 20 nm and 100 nm Nickel via electron beam deposition. The nickel deposition was performed using a Temescal CV-8 E-beam evaporator using a previously developed recipe[180], [181]. We coated Ni at a deposition rate of 0.4-0.8 angstrom/s. For the first 10 nm, the deposition rate was kept at 0.4 angstrom/s, and beyond the first 10 nm it was kept at a rate of 0.8 angstrom/s. The low deposition rate ensures that the deposition power required is low and the resulting joule heating radiated from the source to the sample in the vacuum chamber is well controlled, the measured temperature during the deposition never exceeded 50 °C. A coating thickness of 20 nm is selected to approach the maximum predicted infrared enhancement while avoiding the sharp slope of

the curve to the left of the inflection point seen in Figure 6-1(b). Our simulation assumptions could also potentially influence the inflection point, so the thickness is selected close to but not at the simulation predicted inflection point. The SEM images in Figure 6-4a and Figure 6-4c show the micropyramid texture silicon and nanotextured micropyramid Si surface respectively. The random nature of the textured silicon fabrication process results in an aperiodic surface texture, with the base span (L) ranging from ~ 2 to 14 um in length. The KOH etching process etches preferentially, resulting in a pyramid with a base angle that is 54.7° from the substrate and 35.26° from the normal[182], leading to a fixed micropryamid aspect ratio (h/L) of ~ 0.8.

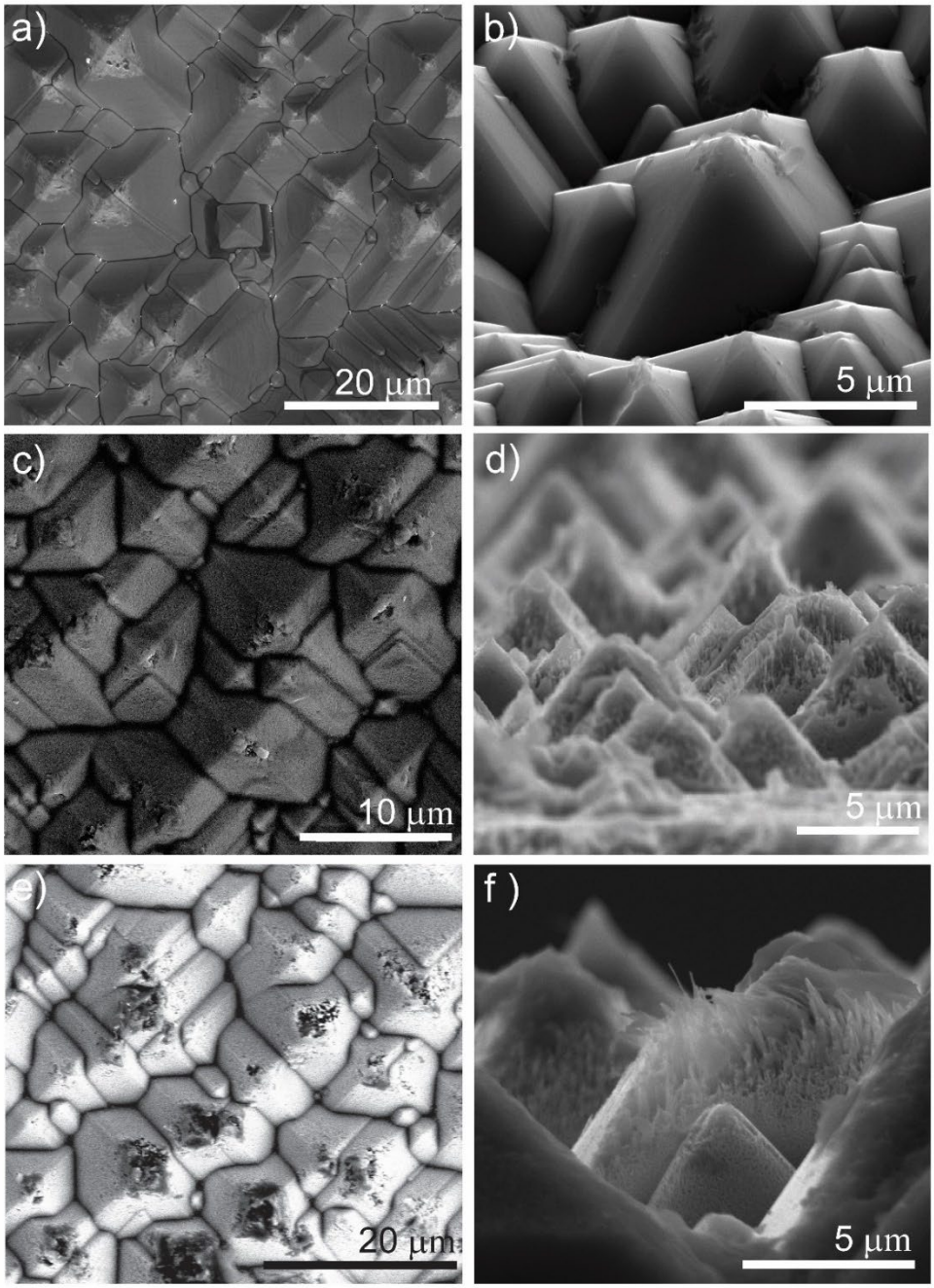

Figure 6-4 SEM Images of the fabricated (a) silicon micropyramids, (b) titled view of the micropyramids, (c) nano-textured silicon micropyramids, (d) cross-sectional view of the nanotextured micropyramids, (e) nickel coated nano-textured silicon micropyramids, and (f) cross-sectional view of the nickel coated nanotextured micropyramids. Our surfaces are over 99% covered with aperiodically arranged micropyramids, and the average base size of the pyramids ranges from 2 to 14 um. The base angle is process dependent at 54.7°, which results in fixed aspect ratio (height/base) and thereby a height that is dependent upon the base length

6.3.2 Sample Optical Characterization

The optical properties of textured and Ni-coated textured Si samples were characterized by measuring the diffuse reflectivity (R) and transmittivity (T) spectra, based on which we deduced the emissivity ($\varepsilon = 1 - R - T$), where we assume Kirchhoff's law holds and the emissivity and absorptivity are interchangeable[183]. This assumption holds given a thermal equilibrium with the environment and that $\alpha + R + T = 1$. Given our measurement conditions, the sample is in thermal equilibrium with the environment. While metallic gratings and micropyramids can be used to induce asymmetric scattering and nullify this assumption[184], our experimental and computational setup are not designed to induce or utilize non-reciprocal behavior. The reflectance spectra of the textured surfaces with and without Ni coating were measured in the visible (VIS, 0.4-2.4 μm) to near-infrared (IR, 2.4-16 μm) and mid-IR wavelengths using the Jasco V-670 UV-VIS spectrophotometer coupled with a 60 mm integrating sphere and Nicolet 6700 Fourier-transform infrared spectrometer respectively. The sample surface was oriented normal to the light source. For the UV-VIS measurement, the diffuse reflectivity and transmissivity measurements are calibrated with a standard white body. For the measurement of diffuse transmissivity, the samples were placed on the front port of the spectrometer allowing all transmitted light to reach the detector. The optical measurements have an inherent uncertainty of ±0.003 for the properties ranging from 0 to 1 and the wavelength uncertainty of the spectrometers is ±0.3 nm at a standard room temperature of 25 °C.

6.3.3 Simulation Approach – Single vs Multi-unit Cell Simulations

A key assumption that is made in the simulation work is that the randomly arranged non-periodic Si microstructures can be presented with a periodic unit cell. To validate this assumption, a much larger domain consisting of many overlapping pyramids is simulated and the results are compared to the unit cell approach. In Figure 6-5, we plot a comparison between micropyramid silicon (M-Si) with 20 nm of Ni as a conformal coating for the single pyramid and multiple pyramid unit cells. Whereas the simulation results shown in the manuscript are based on a singular pyramid with a base span (x_{span}) of 5 um and a height of 4 um (aspect ratio = 0.8, x_{span}^2 = 25 um^2), the "large-domain" simulations encapsulate a 20 x 20 um space (400 um^2), as visualized in Figure 6-5 (a). Each pyramid within the space is fixed

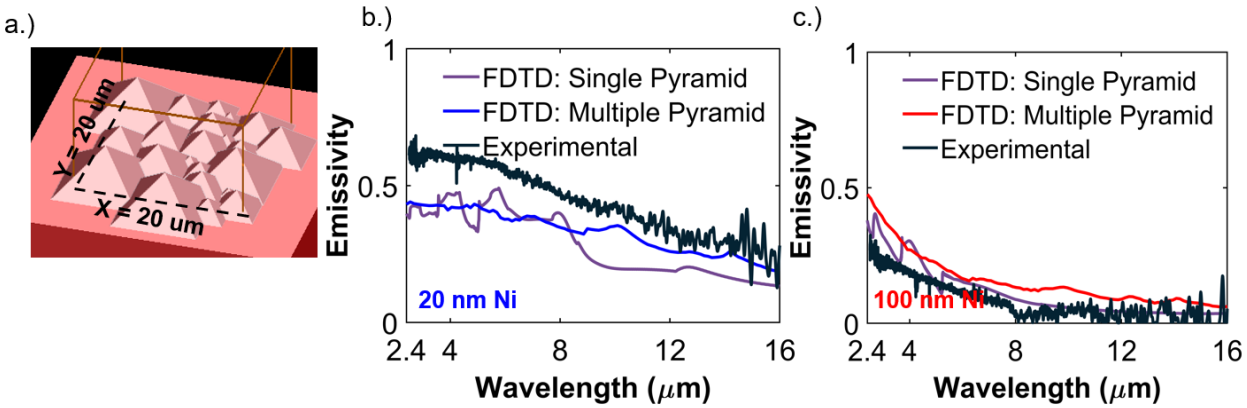

Figure 6-5 (a) Simulation domain of the multi-pyramid simulations. Pyramids are overlap and have a base span ranging from 2 – 10 μm. All pyramids are fixed to an aspect ratio of 0.8. (b) Comparison of periodic single and multiple pyramid simulations and experimental micropyramid silicon (M-Si) with 20 nm of nickel coating. (c) Comparison of single pyramid, multi-pyramid, and experimental M-Si with a 100 nm nickel coating. While there are observed differences between the spectrums, with the randomly distributed large scale micropyramid simulations aligning more closely with the experimental results, there is not a significant variation.

to an aspect ratio of 0.8, but the x_{span} is fluctuated. Additionally, the pyramids overlap to mimic experimental conditions. Identical to the single pyramid simulations, we assume that there is a conformal layer of nickel across each pyramid. In total, there are 23 pyramids in the multi-pyramid large-domain simulation. While the computational results do not match up perfectly in magnitude with the experimental results, we can say that there is not a significant variation between the multiple pyramid and single pyramid simulation results. While both processes still utilize a "unit cell" and are not completely random in the same way a fabricated sample would be, it is evident that the simulation results are not very different when the simulation domain is expanded to more properly reflect the experimental conditions. Thus, while neither simulation perfectly represents the experimental conditions, the extra computational time demanded by the much larger simulation is not necessary as the single pyramid unit cell is a sufficient approximation of the optical properties.

In Figure 6-6, the effect of the micropyramid base dimension on the optical properties for the single pyramid unit cell approach is shown. While there are variations in the predicted emissivity, the infrared spectrum averaged value is approximately equivalent. We note that the larger pyramids have a more noticeable impact on optical properties in the 8 – 16 um wavelengths. The results shown align with those seen in the single pyramid vs. multi-pyramid results shown in Figure 6-5(b).

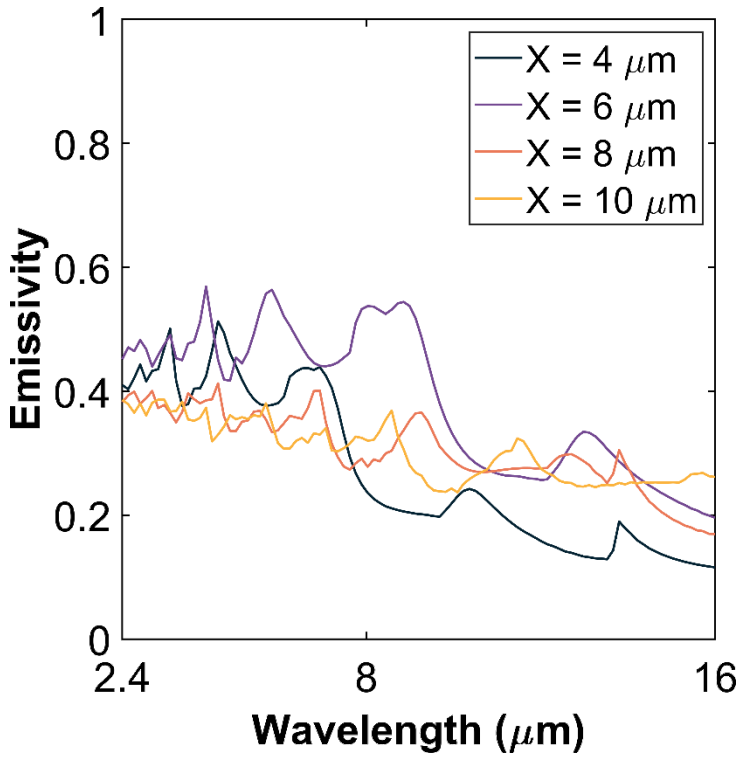

Figure 6-6 FDTD Simulations comparing the role of pyramid base size (X) on the optical properties. While there are variations, particularly in the 8 – 16 um region, the results are generally equivalent. For the highest degree of accuracy, large multi-pyramid simulations like those shown in Figure 7-4 (a) should be used. This approach, however, is effective in predicting both the trend and does not differ substantially in magnitude from the multi-pyramid approach.

6.3.4 Nickel Interface and Material Characterization

Given the relative size of our conformal coating layer (20 – 100 nm) to the pyramidal texturing, the interface can play a substantial role in determining the optical properties. The precise role of the interface is unknown in the current study. More study is required to understand the interactions between the interface and the matter light interactions at the surface of the additional nanotexturing. An additional potential complication would be the formation of a nickel silicide at the interface between the metallic coating and the silicon texture. While we cannot be guaranteed that nickel silicide(s) are not present at the interface without more study, we are confident based on our process conditions and X-ray diffraction (XRD) characterization that there are no silicides at the interface. Our deposition process occurs at a low temperature (< 50 °C) due to the process conditions used in deposition. This is which is substantially lower than previously studied formation temperatures of silicide, which are known to be induced by high temperature fabrication (350 °C or higher) processes[185]. To provide further evidence that silicide formation has not occurred at the interface, we perform parallel-beam XRD to study the measured peaks and compare them to known nickel and nickel silicide patterns. We perform these measurements on the untextured silicon sample with a 20 nm layer of nickel. Based on the findings shown in Figure 6-7, we are highly confident that our deposition process has not resulted in the formation of silicide at the interface.

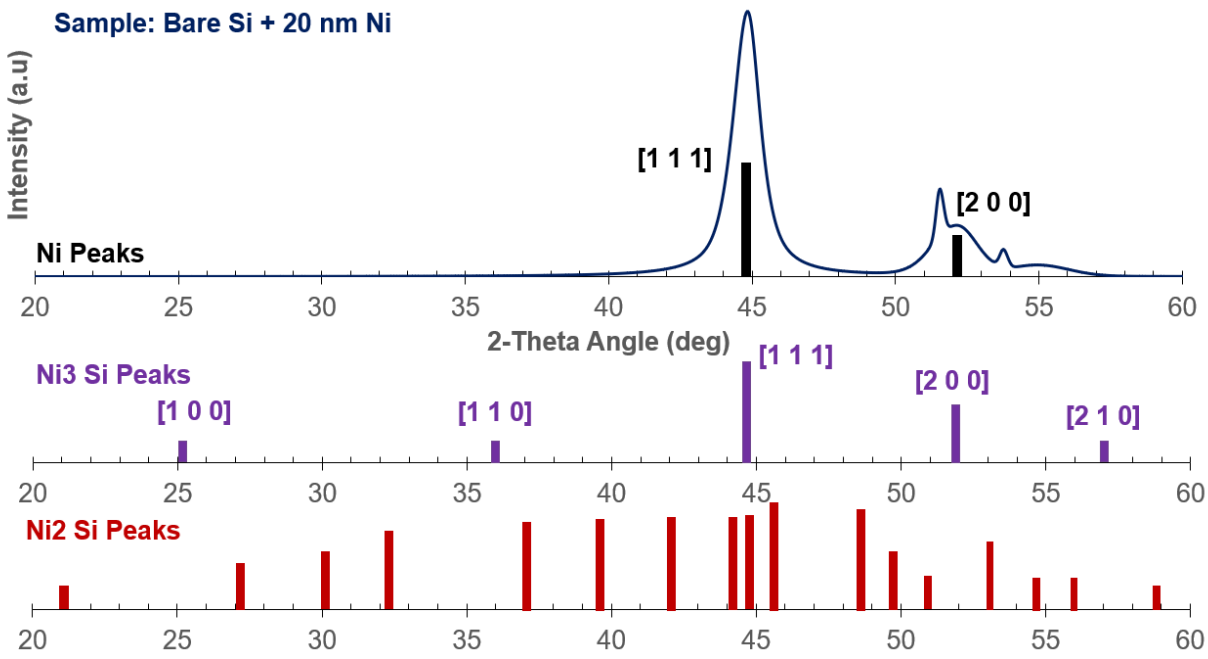

Figure 6-7 Parallel beam XRD measurements for the untextured (bare) Si with a 20nm of Ni coating. The peaks for Ni (PDF: 01-071-4655), Ni3Si (PDF: 01-072-2549), and Ni2Si (PDF: 00-050-0779) are shown for reference. Based on the location and intensity of the observed peaks, and the absence of notable peaks expected from silicides in other locations, we are confident that a nickel silicide has not formed in the sample. More study, however, will be required to definitively understand the role of the interface in determining the measured optical properties.

6.4 Experimental Measurements and Results

The optical properties of textured and Ni-coated textured Si samples are characterized by measuring the diffuse reflectivity (R) and transmittivity (T) spectra using UV-Vis and FTIR spectroscopy. We deduce the emissivity ($\varepsilon = 1 - R - T$) from these measurements assuming Kirchhoff's law holds and the emissivity and absorptivity are interchangeable[183]. This equation assumes that the surface is in thermal equilibrium with the environment, which is valid for the spectroscopic measurement conditions. Figure 6-8 shows the reflectivity, transmissivity, and the calculated emissivity for untextured Si and Si textured with micropyramids and nanotextured micropyramids. In Figure 6-8(a-c) uncoated and untextured Si are plotted for reference. In the VIS to near-IR wavelength, compared to bare Si, strong anti-reflective behavior can be observed for micropyramid textured Si (Figure 6-8 (d)), nanotextured micropyramid textured Si (Figure 6-8 (g)) which has been well understood and documented in the literature[41], [173]. The optical properties from 400 nm to 1100nm are plotted in more detail in Figure 6-9. In the mid-IR range, the reflectivity of M-Si and N-M-Si is lower than the bare Si towards longer wavelength, and the difference between the two spectra gradually vanishes because the nanowires are overlooked by longer-wavelength light. We observe slight antireflective behavior in the M-Si and N-M-Si uncoated samples near $\lambda = 8$ μm, potentially corresponding to the average measured base span of the micropyramid texture. Measured spectral properties of fabricated Si NWs in the same wavelength ranges and are shown in Figure 6-10.

The nanotextured micropyramid silicon achieves higher emissivity and lower transmission between 0.4 to 6 μm, which, as has been previously explained in the literature, is due to enhanced coupling of light into the Si substrate by broadening the k-vector that light

is scattered[41], [45]. Due to the missing nanostructures in M-Si and dominant in-plane light scattering, M-Si achieves a slightly lower transmissivity than bare Si. Interestingly, for N-M-Si, the transmissivity is slightly higher than that of M-Si up to 6 μm and then drops significantly possibly due to the presence of nanowires beyond 6 μm, which is consistent with the trend observed for Si NWs[41]. As a result, the mid-IR emissivity of N-M-Si is the highest, reaching 0.6 between 8 to 16 μm, whereas those of M-Si, Si NWs, and bare Si decrease across the same wavelengths.

As discussed, Si micropyramid texturing has a small impact on the MIR and NIR optical properties due to mid-IR transmission of Si. We improve this aspect by adding a thin metallic coating on the top surface of the textured silicon. Using a previously developed deep-neural network, we search a catalog of materials to identify metals that are best suited for enhancing the light absorption of the surface. Predicted thermal and optical performance for a catalog of materials generated by a neural network and details on the process discussed in previous chapters. Balancing practicality of deposition and application with material performance, we select nickel as the coating material. In Figure 6-8(d-f), we present the reflectivity, transmissivity, and the deduced emissivity of 20 and 100 nm Ni-coated M-Si compared to the uncoated M-Si.

While many metals could be suitable for enhancing the infrared absorption properties, nickel has a relatively shallow increase in the refractive index with increasing wavelength[69]. Metals with high extinction coefficients in the infrared, such as Au, Ag, Pt, etc., are predicted to be not as effective with a significantly reduced tunability. Based on our findings, we expect that other metals can be used to induce similar or unique absorption

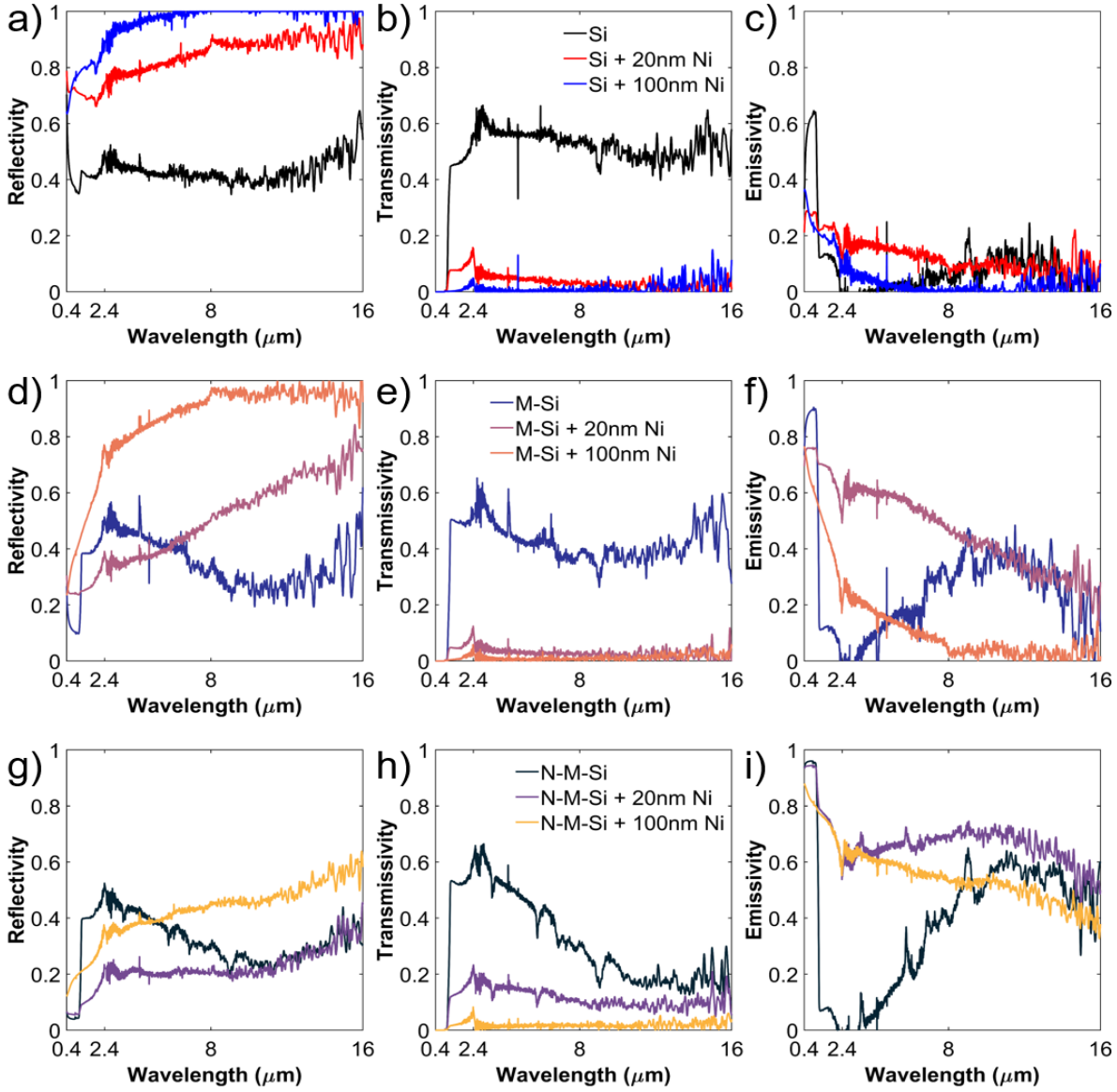

Figure 6-8 Measured optical properties over the VIS-NIR (0.4 – 2.4 μm) and Infrared (2.4-16 μm) regions measured by UV-VIS and FTIR spectroscopy respectively. (a – c) Measured optical properties of untextured Si with no Ni coating, 20 nm Ni, and 100 nm Ni. (d – f) Measured optical properties of micropyramid (M-Si) textures with no Ni coating, 20 nm Ni and 100 nm Ni. (g – i) Optical properties of nanotextured micropyramid (N-M-Si) with no Ni, 20 nm Ni, and 100 nm Ni.

characteristics in the MIR. For this work, we demonstrate the effectiveness of nickel coatings, but future work will reveal unique optical properties obtainable from combining nano and microtextured silicon with different metal coatings.

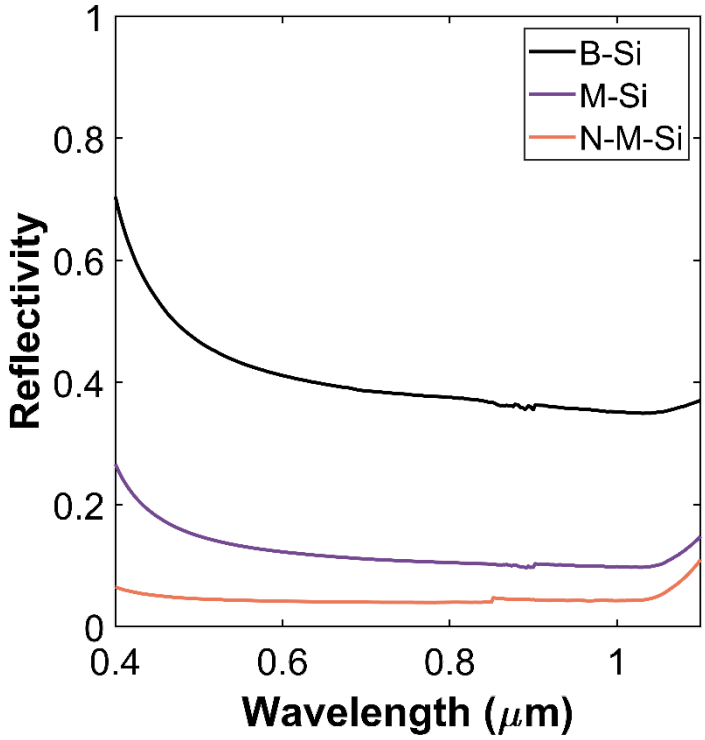

Figure 6-10 Measured Optical properties of untextured, M-Si, and N-M-Si surfaces in the Vis-NIR region, measured from λ = 400 to 1100 nm. The results are in line with previous micropyramid Si references[24], [45], [52], and shows a substantial reduction in the reflectivity with the variation in texture.

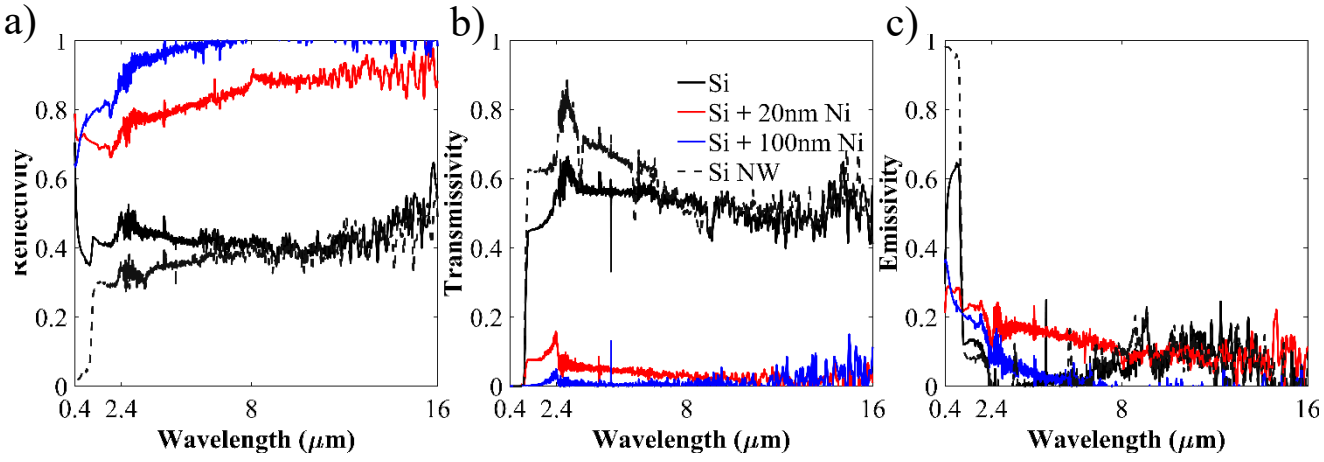

Figure 6-9 Measured UV-VIS and IR properties of untextured Si with no nickel coating, 20 nm of Ni, 100 nm of Ni, and Si with Si nanowires over the UV-Vis-NIR (0.4 – 2.4 μm) and Infrared (2.4-16 μm).

Based on transmissivities shown in Figure 6-5(e), the most notable immediate effect of the Ni coating is a reduction of the infrared transmission. Such a notable change is more obvious by comparing with the N-M-Si plotted in Figure 6-5(h). Spectral transmissivity is reduced to near zero in both cases. Next, for the reflectivity, we observe that Ni coated untextured Si and Ni coated M-Si yield higher reflectivity due to the high refractive index of Ni in mid-IR wavelengths. Interestingly, from 0.4 to 12 μm, 20 nm Ni-coated N-M-Si achieves a lower reflectivity than N-M-Si, indicating a combined effect of anti-reflective properties induced by nanowires and the high extinction coefficient of Ni in the wavelength range. Increasing the amount of Ni within the texture leads to an increase in the effective permittivity of the surface, resulting in reduced absorption at coating thicknesses beyond the inflection point, as seen in the 100 nm N-M-Si coated sample. The

Substrate	Nickel Coating	Visible* Reflectivity	Solar** Reflectivity	Infrared** Reflectivity	Infrared** Transmissivity	Infrared** Absorptivity
Bare Si	None	0.46	0.42	0.43	0.53	0.04
Bare Si	20 nm	0.72	0.70	0.86	0.05	0.11
Bare Si	100 nm	0.68	0.79	0.98	0.01	0.01
M-Si	None	0.15	0.30	0.35	0.44	0.21
M-Si	20 nm	0.25	0.27	0.52	0.02	0.46
M-Si	100 nm	0.29	0.50	0.91	0.02	0.07
N-M-Si	None	0.04	0.28	0.33	0.30	0.37
N-M-Si	20 nm	0.06	0.10	0.23	0.11	0.66
N-M-Si	100 nm	0.15	0.23	0.45	0.02	0.53

Table 6-1 Summary of experimental findings shown from Figure 2 for bare, micropyramid textured silicon (M-Si) and nanotextured micropyramid silicon (N-M-Si). All values are computed using the equation, $(\frac{\int X(\lambda)d\lambda}{\Delta\lambda})$, where X is the optical property (α, R, or T) and is a function of the wavelength.

*Visible Reflectivity is an integrated average over 0.4 – 0.7 um wavelengths
**Solar reflectivity is an integrated average over 0.4 – 2.4 um wavelengths.
***Infrared properties an integrated average over 2.4 – 16 um wavelengths.

precise inflection points for either M-Si or N-M-Si are not currently known. More study is required to further illuminate the inflection relationship for both textures. Beyond 12 μm, the longer-wavelength light increasingly ignores the nanotexture, leading to comparable reflectivity of 20 nm Ni-coated M-Si to N-M-Si.

The advantage of the thin Ni coating compared to the textured Si is further shown by the measured emissivity spectra, where 20 nm N-M-Si has a measured emissivity between 0.6 to 0.7 over the entire NIR to mid-IR wavelengths. As expected[41], [45], the uncoated nanotextured silicon achieves a much higher emissivity in the MIR compared to the uncoated micropyramid textured Si due to the introduction of new optical modes as a result of the disordered nanotexture. The nanotexture, however, has a negligible influence on the measured transmission from λ = 1-7 um, which leads to the average IR emissivity of the M-Si + 20 nm Ni to be much higher than the uncoated nanotextured silicon. To counteract the MIR transmission, coating 20 nm of Ni on the nanotextured micropyramid silicon negates the majority of the transmission and thus enhances the emission across the NIR to MIR spectrum. Due to the interplay between the reflection and transmission at the surface, N-M-Si + 20 nm Ni has an even higher emissivity in the MIR than the uncoated N-M-Si sample. Selected averaged optical values ($\frac{\int X(\lambda)d\lambda}{\Delta\lambda}$) are shown in Table 7-1, summarizing the measurements shown in Figure 6-1 and 7-5, where X represents an optical property (α, R, T) that is a function of wavelength λ.

6.5 Simulation Comparison to Experimental Results and Other Materials

Comparing our FDTD predictions to our experimental results, while the M-Si and N-M-Si + 20 nm Ni predictions are accurate, we have a significant deviation for the N-M-Si +

100 nm Ni. The predicted emissivity is substantially lower than the measured N-M-Si + 100 nm Ni results, as seen in Figure 6-5(i) and Figure 6-5(e). Comparing Figure 6-8(g) to Figure 6-1(c) our models do not predict the anti-reflective properties of the 100 nm coated N-M-Si accurately. The highly disordered and random nature of the fabricated nanotexture is expected to substantially reduce the reflectivity, and this texture is not captured in the nanotexture simulation. Additionally, the role of conformity of the nickel on the nickel optical properties is currently undetermined. More study will be required to understand the precise matter-light interactions at the surface of the metal coated nanotextured micropyramid. In Figure 6-11 and 6-12, we show the comparison of the predicted simulation values to those that are measured. The experimental values are shown in dashed lines and the predicted (FDTD) values are shown in the solid lines. The largest difference comes in Figure 6-11, for the N-M-Si 100 nm prediction, which varies dramatically from the prediction. As discussed in the text, this indicates that we have incorrect assumptions for our N-M-Si simulations, and more work is required to understand the precise mechanisms that lead to this enhancement.

The role of the conformal coating, interface, randomized texture, etc., need to be explored in more detail in future work.

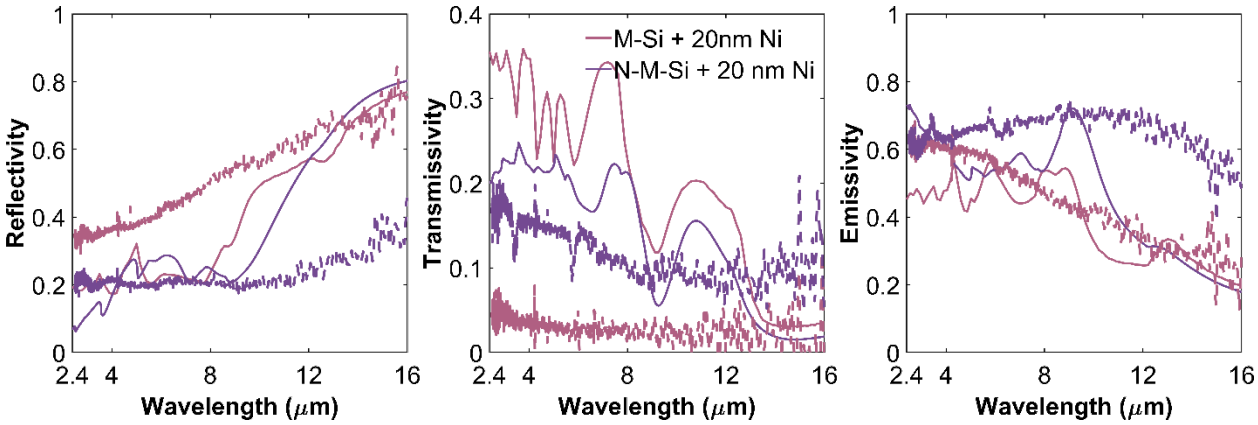

Figure 6-11 Comparison of measured and predicted optical properties for 20 nm of Ni on M-Si and N-M-Si over the infrared spectrum (2.4 to 16 um). Experimental results are shown as dashed lines, FDTD results as solid lines.

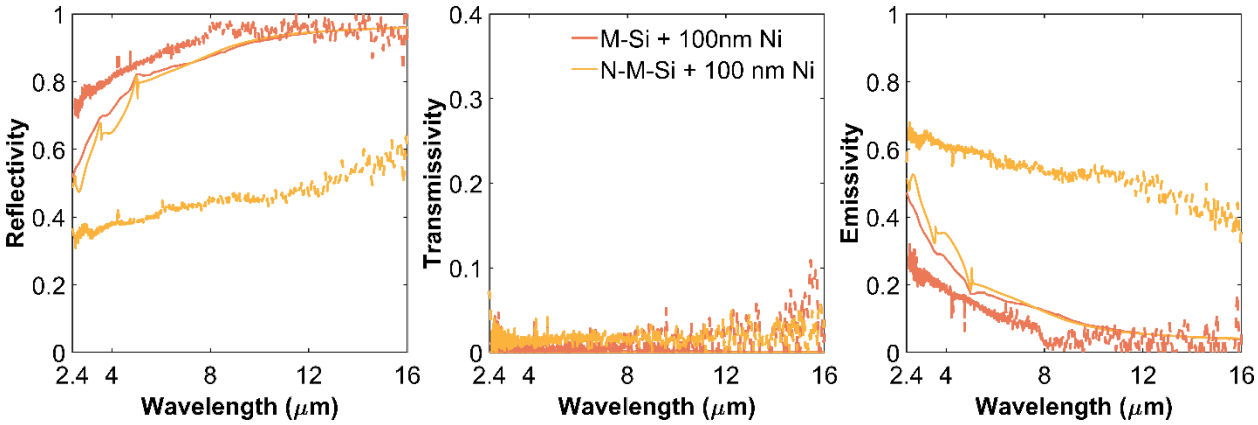

Figure 6-12 Comparison of measured and predicted optical properties for 100 nm of Ni on M-Si and N-M-Si over the infrared spectrum (2.4 to 16 um). Experimental results are shown as dashed lines, FDTD results as solid lines.

Control over the optical penetration of electromagnetic radiation through the coating is what leads to the absorption increases we observe. Coating different metals onto the Si surface will have similar effects to those shown for a nickel coating on textured Si. One material that has already been studied as a coating material for micropyramids is Au[165], [175], but a significant advantage that Ni micropyramids have compared to Au coated Si micropyramids is that the refractive index of Au rises much more quickly than Ni. As a result, the spectral range in which the partial transmission phenomenon that drives the infrared absorption enhancement is much more confined. From simulations shown in the Figure 7-7 and 7-8, we can expect that for equal thicknesses of Au and Ni, Ni coatings will have a much greater enhancement in the infrared regime. While both are effective in enhancing VIS-NIR absorption, Au coated micropyramids have significantly less control over the MIR properties. It should be possible to approximate the nickel coating's IR absorptivity increase by decreasing the Au thickness to have a comparable penetration depth as 15 – 30 nm Ni. However, such a thin layer of gold (< 5 nm) would be highly susceptible to fabrication uncertainty as small changes in the layer composition have a large influence on the optical properties, much more so than the Ni coating. It should be noted that while neither of these structures matches the UV-VIS absorption observed in materials such as nanotextured carbon[186] or plasmonic black gold[187], micropyramid based designs offer significant spectral manipulation over multiple wavelength spectrums as a function of easily modified fabrication parameters. The enhancement in the infrared is critical for thermal applications at high temperatures as well as for MIR emission. Beyond Au and Ni, the partial transmission into the Si combined with the anti-reflective behavior of the micropyramid texturing means

that combinations of varying geometry, metal, and metal thickness could lead to uniquely designed combinations for a broad range of thermal and optical applications.

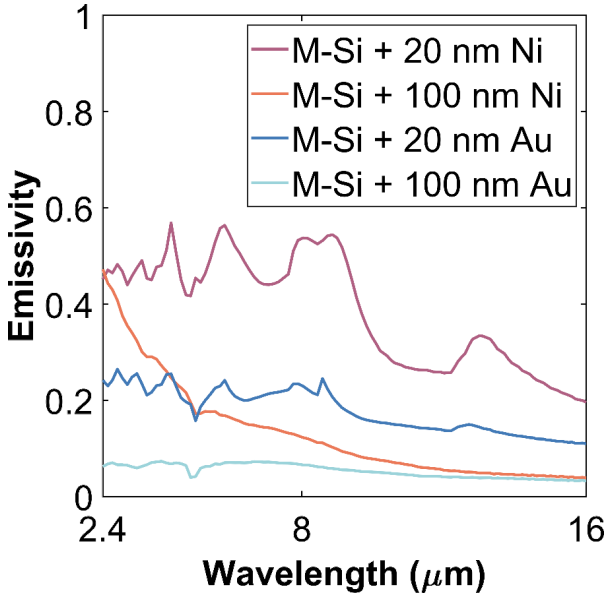

Figure 6-13 Comparison of 20 and 100 nm coated M-Si with Au and Ni. Due to the refractive index of Au, Au does not demonstrate comparable tunability for the same thickness(es). It is estimated that to approach the same optical penetration depth and the same optical properties that M-Si + Ni coatings bring, the thickness of Au would need to be decreased significantly

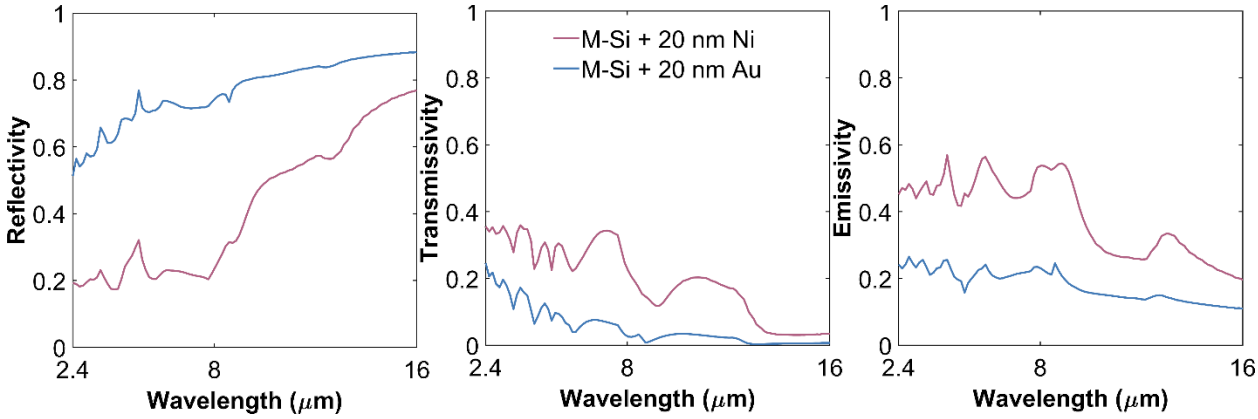

Figure 6-14 FDTD simulation comparison for 20 nm of Ni and 20 nm Au coated on a L = 5 um and h = 4 um micropyramid. Reflection plays a much larger role in the resulting optical properties, driving the effective emission down. This can be explained through the material properties of Au compared to Ni, as Au has a significantly higher extinction coefficient in the infrared region compared to Ni.

6.6 Conclusion

In conclusion, coating nano and microtextured silicon with a nanoscale thick layer of nickel has a significant impact on the infrared optical properties of the textured surface. The optical properties are a result of an interplay between the thin-metal coating and subwavelength features of the silicon nano and or microtexture. We show that control over the penetration depth by varying thickness of the coating leads to significant infrared absorption enhancement and a large degree of tunability in the optical properties. Coating Silicon micropyramids with a nanometer thick layer of nickel (20nm) enables new optical modes and the partial penetration of light results in a significant increase in average infrared absorption from 0.21 to 0.46. Thicker metal coatings deny nearly all transmission into the underlying texture, thereby reducing absorption. At 100 nm of Ni thickness, we establish that

the structure effectively denies transmission, and the optical properties emulate those of a comparably sized microstructure made entirely of Ni. We demonstrate that the infrared absorption can be further increased by introducing additional nanoscale texture on the micropyramids. Compared to the uncoated nano-textured silicon micropyramids, we increase the average infrared emissivity from 0.37 to 0.66 and to 0.57 with a 20 and 100 nm of coating of Ni respectively. Beyond the optical measurements shown, the findings of this work should motivate the use of metal coatings on textured silicon for spectral emission and absorption control and provide insight into the design of complex thermal and optical selective emitters based on metal coatings for thermal applications such as high temperature cooling systems and TPV emitters.

Chapter 7 – Conclusions and Suggestions

7.1 Dissertation Summary

This dissertation has described and demonstrated the analysis, design, optimization, and implementation of microstructures for thermal radiation control via selective emission. The role of geometric and material properties and the connection between the fundamentals of electromagnetics and thermal radiative transport are explored (Ch. 2). Depending upon the material spectral properties, anti-reflective behaviour can be selectively induced and optimized by controlling the aspect ratio, thickness, and base dimensions of micropyramid texturing. The traditional microstructural optimization methods demonstrated, however, are slow and lead to limited use case optimizations so deep-learning methods utilizing deep neural networks (DNNs, Ch.3) and convolutional deep neural networks (CDNNs, Ch.4) were developed to replace traditional optical simulations in the optimization process. The surrogate deep neural network methods were shown to accurately mimic complex microstructural optical simulations for a fraction of the cost and across a library of materials not included in the training data. The surrogate networks are used to generate massive amounts of data for training a reverse network (Ch. 5), enabling rapid and precise microtexture optimization for a desired optical spectrum. The inverse network and surrogate network are linked into a tandem configuration and combined with traditional simulations to form a self-learning loop that can identify better identify optimum geometric and material combinations with each learning loop. Finally, we use the deep neural network method(s) to identify materials that are best suited to enhancing thermal regulation and experimentally demonstrate how microtexturing and hierarchical texturing can be utilized

to enhance broadband emission.

7.2 Suggestions for Future Work

7.1.1 Advanced Machine Learning Micropyramid Optimization and Optical Simulation Emulation

The micropyramid optical analysis and subsequent deep-learning study have allowed us to thoroughly explore the thermal design space of micropyramids made of an array of materials. We have been able to examine the roles of fundamental physics and emulate optical simulations to provide synthetic simulation results that allow us to rapidly optimize micropyramids made of materials beyond the scope of those used in training our deep learning networks. A large limitation with our current methodology, however, is that the architecture of our network confines us to a strict definition of micropyramid geometries. This led to the development of the convolutional method, a method that potentially is not bound by rigid geometric constraints. While the CDNN was shown to be effective in replicating optical simulations as a surrogate (Ch. 4), it's design was still limited to a single periodic micropyramid. A potential – and highly intriguing study – is to take the developed convolutional neural network methods and broaden their scope to include additional geometries. This could also include different materials as coatings, materials inclusions, or embedded materials in widely varying geometries. The goal would be to develop a method that could potentially completely replace FDTD simulations in optimization as a broad-purpose multi-geometry simulation tool. Further, this tool could be developed into an inverse solving generative platform[144], [188], [189], potentially enabling a user to pass in a desired spectrum and the output could be material and geometric information encoded in a unit cell that would satisfy the desired response.

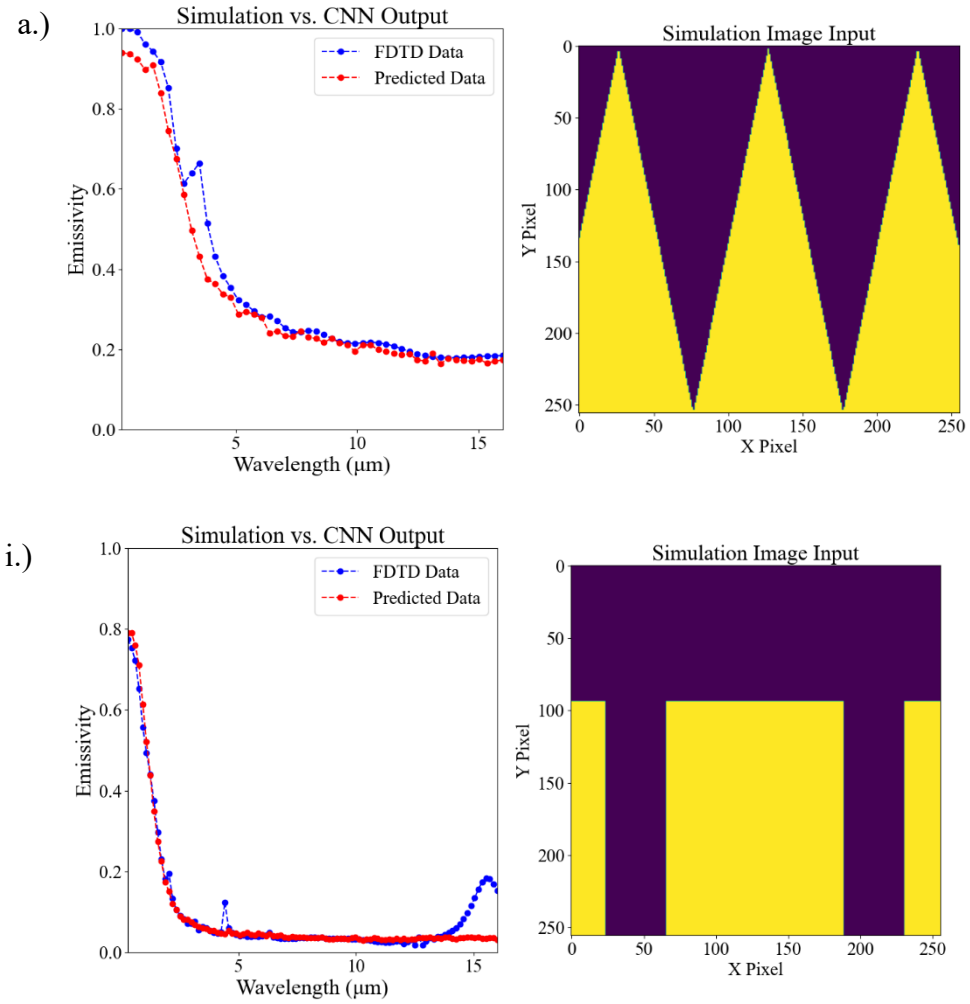

Figure 7-1 Demonstration of a machine vision network that can accurately predict the optical properties of multiple geometries. The same network is used to predict both a and b and the predictions have a mean-absolute error (MAE) of 0.025 when compared to the ground truth emissivity values.

Ultimately, a model like this could be used to predict thermal, optical, acoustic, etc., properties for an image of a simulation domain. Another beneficial inclusion would be adding high temperature optical property modelling to our simulations and model such that we can capture unique temperature dependent behavior. Our current architecture enables us to capture temperature dependent behavior by simply predicting the optical properties

for the adjusted optical properties. The changes in optical properties with temperature can be estimated using ballistic-phonon informed Drude formations. Some materials, such as Carbon, have strong variations in the refractive index as a function temperature, and modelling their high temperature behavior will enable our model to have an extra level of complexity and accuracy in predicting the optical properties for a wide range of thermal properties. Such formulations could add significant levels of complexity and possibilities to the neural network methods.

7.1.2 Multifunctional Materials and Hierarchical Structures

To demonstrate the computational results, we developed silicon wafer molds. While we coated these wafer molds in a nanometer thick metallic coating, the molds can also be used in a template stripping process. Previous studies have demonstrated the use of template stripping for the fabrication of micropyramids made of metals, polymers, dielectrics, etc. and we will use the wafers we fabricate as the foundation of fabricating advanced multifunctional materials patterned with micropyramids. As a basis for the template stripping process **(Figure 7.2)**, we have fabricated and characterized several template silicon wafers. To fabricate these wafers, we use a potassium hydroxide (KOH) based etching method. This method etches the silicon along the (111) plane, etching along a ~ 54-degree angle. We are currently fabricating wafers without using a mask, leading to "random" pyramid surface texturing. This would enable extensive studies of complex materials that may not be compatible with deposition, or in creating microtextures from dynamic and reconfigurable materials such as NiTi (Nitinol)[190]. Potential future studies could focus on patterning and controlling geometric properties of a surface in conjunction

with reconfigurable mechanical properties for passive thermal-mechanical regulation.

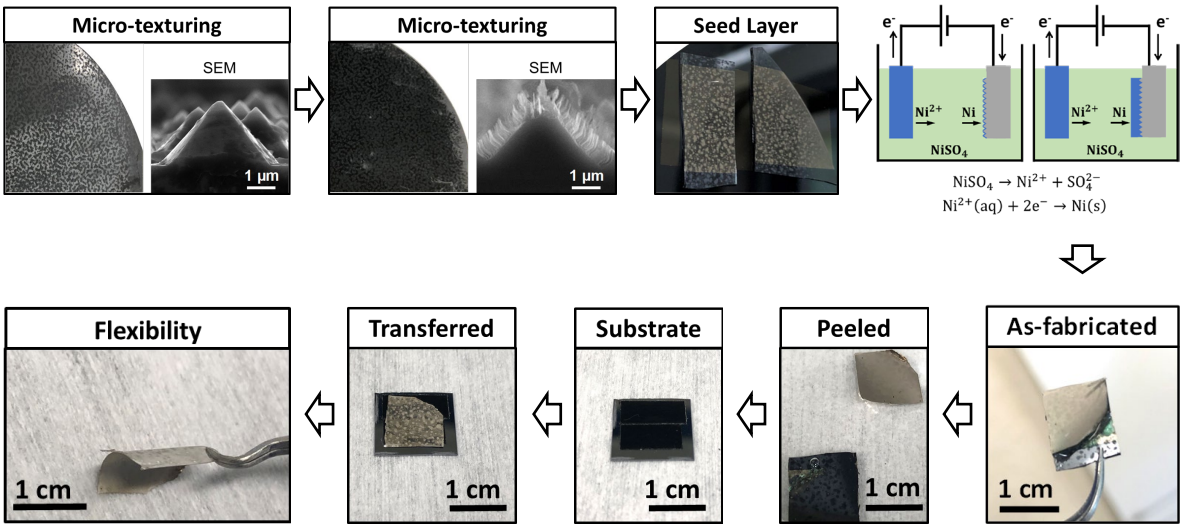

Figure 7-2 Flow-chart demonstrate of the fabrication of the silicon wafer mold(s) and the subsequent template stripping process to fabricate layers inverse-textured with the pattern.

7.1.3 Vanadium Dioxide and Textured Micropyramids

Vanadium dioxide – a phase change material with a transition temperature near 68 °C – holds tremendous promise for use in thermal control systems[191]–[195]. Methods such as doping or strain control [196]–[199] can be used to reduce the transition temperature, opening more possibilities for passive thermal management systems enabled by the phase-change material. Optically speaking, in the pre-transition insulation state, the material is optically transparent thereby resembling a lossy material[200]. After transition, in the metallic phase, the material closely resembles a conductive material. By combining this behavior with the anti-reflective properties of micropyramids we can design a system

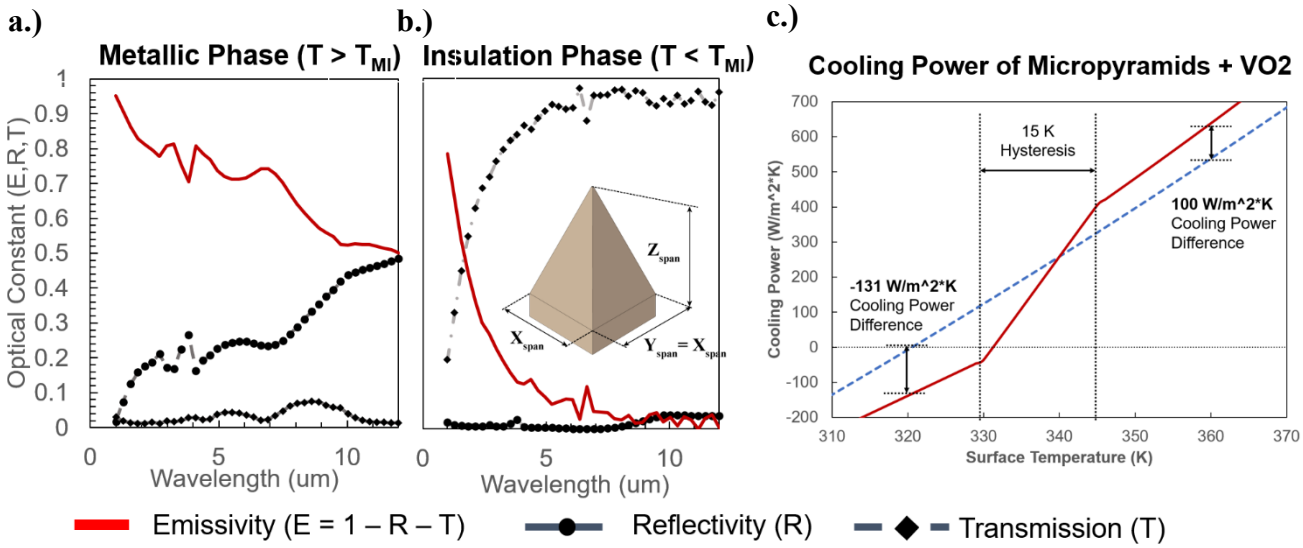

Figure 7-3 FDTD predictions for the metallic phase of 200 nm of Vanadium Dioxide on a 4 x 4 um micropyramid. (b) FDTD predictions for the same geometric configuration for the insulation phase. (c) The high emissivity shown in (b) for the UV-Vis regions of the micropyramids with vanadium dioxide leads to large heating from incident solar radiation. When the phase change occurs, the increase in thermal emission results from the increase in the emissivity in the IR.

that is strongly absorbing in the optical wavelengths below the transition temperature – thus absorbing thermal radiation and heating – and strongly emitting in the IR wavelengths above the temperature, cooling the surface.

The predictions in Figure 7-3 show that vanadium dioxide can be used to fabricate dynamic and multifunctional cooling surfaces that could partially self-regulate temperature completely passively. We have studied the influence of the thickness of the vanadium dioxide layer on the silicon wafer and are exploring incorporating hierarchical texture as a means of controlling both the optical response and the transition temperature. Optical measurements from preliminary results have shown that we can reduce the reflectivity and increase the absorption significantly as a function of the micropyramids and that we have a slight change in the emissivity as a function of temperature. the simulations and analytical understanding of optical transmission indicate that the combination of a at least 200 nm of vanadium dioxide in conjunction with a high uniformity/periodic micropyramid silicon base template is highly effective at passively regulating temperature. With additional updates to fabrication methods and precision control over geometry and fabricated vanadium coatings, highly tunable and self-regulating surfaces could be achieved.

7.1.4 Surrogate Neural Networks for Microspheres

While micropyramids have been demonstrated as effective candidates for thermal management, there are physical limits to how much a single material can be engineered to manipulate light via micropyramid geometry. As previously seen, the refractive index of a material creates windows for manipulation but precise control over an optical response can sometimes necessitate the use of additional materials or hierarchical structures. As

discussed in Chapter 2, materials such as polymers benefit from the inclusion of micropyramids in the infrared by decreasing the already small quantity of reflected light to a near zero value. It was evident, however, that due to the refractive index of a material such as PDMS in the UV-VIS wavelengths no degree of geometry will lead to a decrease in the UV-VIS transmission.

The core design of a radiative cooling structure[18], [20] is the reflection of light in the UV-VIS-NIR (0.2 – 2.4 um), and near perfect emission of light in the infrared. Radiative cooling materials could lead to significant energy savings for buildings [201], [202] and improve spacecraft thermal regulation methods[203], [204]. There have been multiple demonstrations of perfect reflection in the UV-VIS-NIR via dielectric materials[57], [205]–[207], metallic reflectors[208], or Bragg-reflectors[10], [209]. These structures, however, are often limited by expensive and sophisticated fabrication methods or suffer from gaps in spectral performance. An inexpensive and easily scalable solution for achieving broadband near-perfect solar reflectors is to use dielectric particle-polymer composite structures[20], [110], [166] with either a porous polymer[51] or hollow microsphere[20], [166], [210]. Previous studies using Mie theory and 2D FDTD have indicated that hollow microspheres with a thin shell induce strong scattering, leading to near-perfect solar reflection[110], [166]. These composite structures combine the near perfect solar reflection with the polymer's natively high infrared emissivity, resulting in a polymer composite material that is scalable, easy to manufacture, and highly efficient at radiative cooling.

A DNN architecture for a preliminary microsphere composite surrogate network is visualized in Figure 7-4. Unlike the micropyramid deep-learning derived architectures, the microsphere composite system is far more geometrically complex. The micropyramid

domain has 3 geometric parameters, whereas the microspheres can be represented with no less than 5 (y_{span}, t_{ratio}, r_{min}, r_{max}, AF). Furthermore, while both microsystems are simulated as periodic unit cells, the random particle generation process will lead to variations in the predicted optical properties. Output variations will occur even for a fixed set of input parameters due to the random distribution of the scattering media in the composite. Thus, in addition to the geometric parameters, a neural network needs a way to interpret the role of the random particle distribution. To accommodate this issue, the network could be designed along two approaches. The first approach is to introduce two additional input parameters: an "effective" mean-free path and number of neighboring particles within a set radius. The second approach is to use an image-based convolutional neural network. The two approaches are not mutually exclusive, as the image-based approach can enhance the network's interpretation of the particle's distribution and the impact the distribution has on

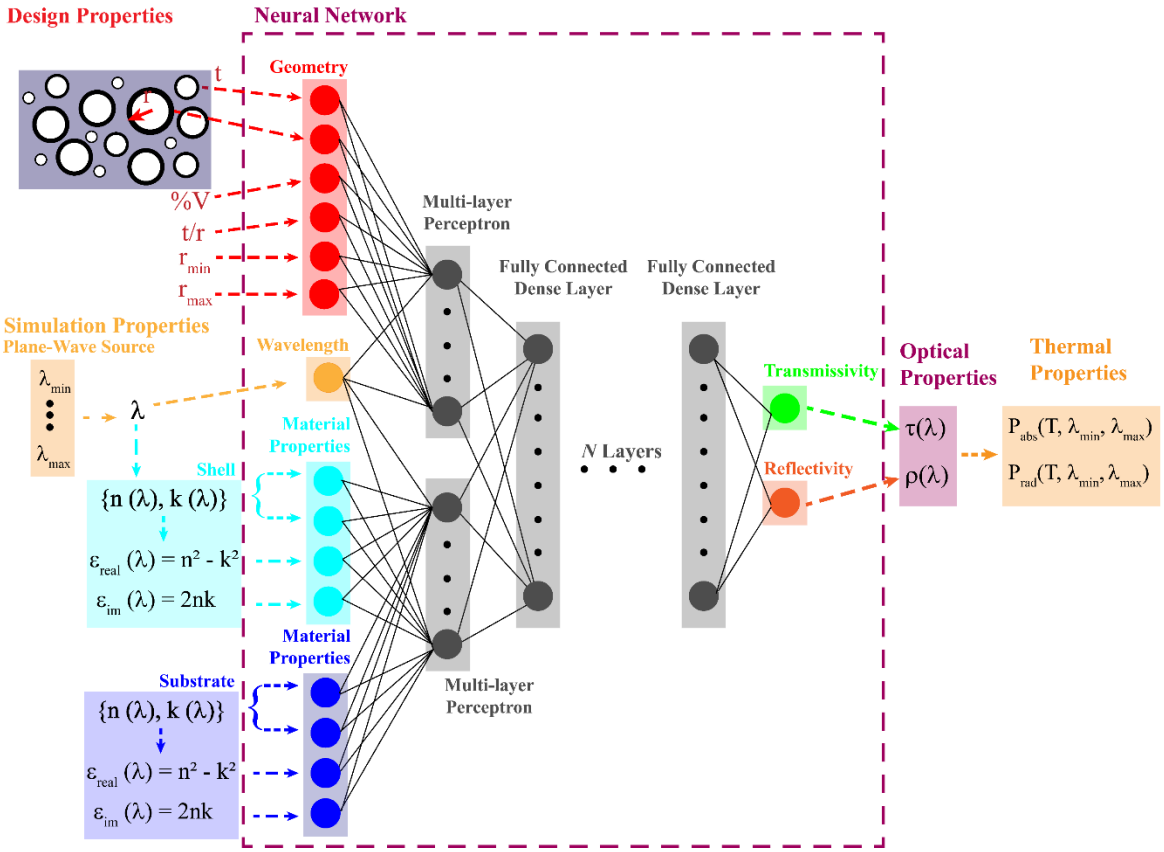

Figure 7-4 Visualization of Microsphere DNN methodology. The architecture takes in the geometric, material, and wavelength information and outputs a reflectivity and transmissivity that correspond to the input wavelength, mimicking a FDTD simulation.

the determination of the optical properties. Figure 7-5 plots the mean absolute error that results from the training process with and without calibration data for the Al2O3 (Figure 5-7(a)) and CaCO3 (Figure 5-7(b)) datasets for both the DNN and CDNN methodology. When no data from these datasets is included in training, the model has an MAE between the prediction and simulation of 0.066 and 0.053 for the alumina and calcium carbonate microsphere simulations respectively using the DNN method. This value drops to 0.061 and 0.046 for the CDNN method. As we begin to introduce simulation data into the neural networks to calibrate the model, this performance significantly improves, and the error continues to decrease. This result matches both our expectations as well as our previous

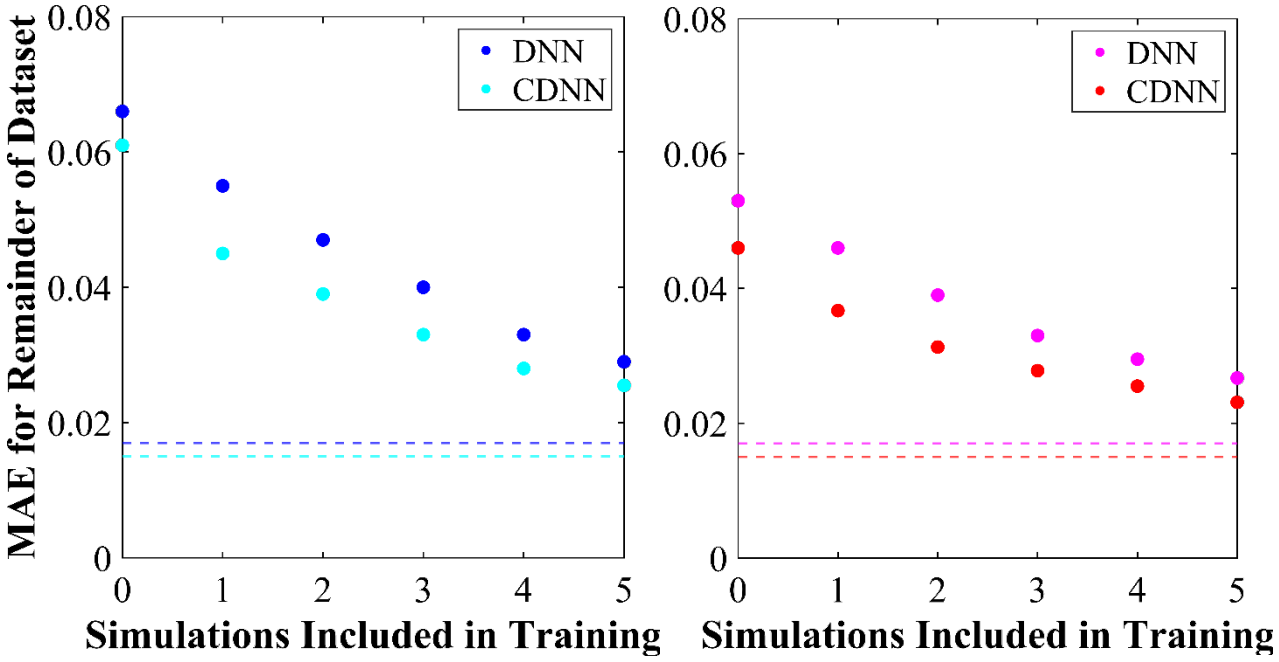

Figure 7-5 Mean absolute error between simulation results and neural network predicted results for Alumina (a) and CaCO3 (b) when 0 to 5 simulations are included in training the CDNN and DNN architectures. The test dataset performance is shown in the dashed line to provide a comparison between predictions for the "unseen" materials and materials that are in the training/validation process

results for the micropyramid neural networks. Thus, additional exploration of this method has several potential routes of study. The first and most immediate is to mimic the micropyramid surrogate-reverse methodology for the design of micro-composite systems. A second potential – and subsequent –route would be to explore an image-based neural network that incorporates multiple geometries, tying the previous micropyramid work into the microsphere composite work.

Appendix A – Materials Included in the Neural Network Surrogate

Original Surrogate Materials*	Library Materials**
Alumina (Al2O3)[125]	Aluminum Nitride (AlN)[125]
Aluminum (Al)[120]	Boron Carbide (B4C)[127]
Chromium (Cr)[69]	Barium Fluoride (BaF2)[128]
Copper (Cu)[69]	Beryllium (Be)[129]
Diamond[124]	Carbon (Graphite)[130]
Iron (Fe)[69]	Carbon (Graphene)[211]
Nickel (Ni)[120]	Copper (Cu)[69]
PDMS[62]	Calcium Magnesium Carbonate (CaMg(CO3)2)[128]
Silver (Ag)[119]	Cesium Bromide (CsBr)[212]
Silicon Carbide (SiC)[123]	Gallium Arsenide (GaAs)[69]
Silicon Dioxide (SiO2)[69]	Germanium (Ge) [69]
Tin (Sn)[69]	Gold (Au)[126]
Tantalum (Ta)[121]	Indium (In)[131]
Titanium (Ti)[69]	Indium Arsenide (InAs)[132]
Vanadium Dioxide (M)[122]	Indium Phosphate (InP)[132]
Vanadium Dioxide (I)[122]	Lithium (Li)[133]
Tungsten (W)[69]	Lead (Pb)[128]
	Magnesium (Mg)[134]
	Molybdenum (Mo)[121]
	Niobium (Nb)[135]
	Osmium (Os)[136]
	Potassium Chloride (KCl)[128]
	Palladium (Pd)[69]
	Platinum (Pt)[69]
	Rhodium (Rh)[69]
	Silicon (Si)[69]
	Silicon Nitride (Si3N4)[125]
	Titanium Dioxide (TiO2)[213]
	Vanadium (V)[120]
	Zinc (Zn)[128]
	Zinc Oxide (ZnO)[128]
	Zinc Sulfide (ZnS)[128]
	Zinc Selenide (ZnSe) [128]
	Zirconium (Zr)[128]

* Each material in this category has at least 1000 simulations

* Each material in this category has exactly 100 simulations included as baseline

Appendix B – GitHub Repositories

GitHub Repository for Surrogate Neural Network

https://github.com/jmsulliv/Optical-Prediction-Neural-Network.git

GitHub Repository for Inverse Neural Network Architecture

https://github.com/jmsulliv/Optical_Prediction_Reverse_Network

References

[1] Purcell and Morin, *Electricity and Magnetism*, 3rd ed. New York: Cambridge University Press, 2013.

[2] M. Planck, *The Theory of Heat Radiation*. Philidelphia, PA: P. Blakinston's Son & Co., 1914.

[3] H. Eugene, *Optics*. Addison-Wesley, 2002.

[4] A. L. Fahrenbruch and R. . Bube, *Fundamentals of Solar Cells: Photovoltaic Solar Energy Conversion*. New York: Academic, 1983.

[5] J. . Duffie and W. . Beckman, *Solar Thermal Engineering Processes*. New York: Wiley, 1980.

[6] W. Stein and K. Lovegrove, Eds., *Concentrating Solar Power Technology: Principles, Developments and Applications*. Philidelphia, PA: Woodhead Publishing Limited, 2012.

[7] T. J. Coutts, "Review of progress in thermophotovoltaic generation of electricity," *Renew. Sustain. energy Rev.*, vol. 3, no. 2, pp. 77–184, 1999, doi: 10.1016/S1364-0321(98)00021-5.

[8] A. Lenert *et al.*, "A nanophotonic solar thermophotovoltaic device," *Nat. Nanotechnol.*, vol. 9, no. 2, pp. 126–130, 2014, doi: 10.1038/nnano.2013.286.

[9] S. D. Lord, "A New Software Tool for Computing Earth's Atmospheric Transmission of Near- and Far-Infrared Radiation," *NASA Tech. Memo. 103957*, no. December 1992, 1992.

[10] M. M. Hossain and M. Gu, "Radiative cooling: Principles, progress, and potentials," *Adv. Sci.*, vol. 3, no. 7, pp. 1–10, 2016, doi: 10.1002/advs.201500360.

[11] W. Li and S. Fan, "Nanophotonic control of thermal radiation for energy applications [Invited]," *Opt. Express*, vol. 26, no. 12, p. 15995, 2018, doi: 10.1364/oe.26.015995.

[12] A. Erika, "The Persian Ice House, or How to Make Ice in the Desert," 2016. https://www.fieldstudyoftheworld.com/persian-ice-house-how-make-ice-desert/.

[13] R. Kumar and M. A. Rosen, "Thermal performance of integrated collector storage solar water heater with corrugated absorber surface," *Appl. Therm. Eng.*, vol. 30, no. 13, pp. 1764–1768, 2010, doi: 10.1016/j.applthermaleng.2010.04.007.

[14] N. Selvakumar, N. T. Manikandanath, A. Biswas, and H. C. Barshilia, "Design and fabrication of highly thermally stable HfMoN/HfON/Al 2O 3 tandem absorber for solar thermal power generation applications," *Sol. Energy Mater. Sol. Cells*, vol. 102, pp. 86–92, 2012, doi: 10.1016/j.solmat.2012.03.021.

[15] J. Zhu, C. M. Hsu, Z. Yu, S. Fan, and Y. Cui, "Nanodome solar cells with efficient light management and self-cleaning," *Nano Lett.*, vol. 10, no. 6, pp. 1979–1984, 2010, doi:

10.1021/nl9034237.

[16] P. Li *et al.*, "Large-Scale Nanophotonic Solar Selective Absorbers for High-Efficiency Solar Thermal Energy Conversion," *Adv. Mater.*, vol. 27, no. 31, pp. 4585–4591, 2015, doi: 10.1002/adma.201501686.

[17] B. J. Lee, Y. Bin Chen, S. Han, F. C. Chiu, and H. J. Lee, "Wavelength-selective solar thermal absorber with two-dimensional nickel gratings," *J. Heat Transfer*, vol. 136, no. 7, pp. 1–7, 2014, doi: 10.1115/1.4026954.

[18] A. P. Raman, M. A. Anoma, L. Zhu, E. Rephaeli, and S. Fan, "Passive radiative cooling below ambient air temperature under direct sunlight," *Nature*, vol. 515, no. 7528, pp. 540–544, 2014, doi: 10.1038/nature13883.

[19] Y. Zhai *et al.*, "Scalable-manufactured randomized glass-polymer hybrid metamaterial for daytime radiative cooling," *Science (80-.).*, vol. 355, no. 6329, pp. 1062–1066, 2017, doi: 10.1126/science.aai7899.

[20] X. Nie, Y. Yoo, H. Hewakuruppu, J. Sullivan, A. Krishna, and J. Lee, "Cool White Polymer Coatings based on Glass Bubbles for Buildings," *Sci. Rep.*, vol. 10, no. 1, pp. 1–10, 2020, doi: 10.1038/s41598-020-63027-2.

[21] A. Krishna and J. Lee, "Morphology-Driven Emissivity of Microscale Tree-like Structures for Radiative Thermal Management," *Nanoscale Microscale Thermophys. Eng.*, vol. 22, no. 2, pp. 124–136, 2018, doi: 10.1080/15567265.2018.1446065.

[22] W. H. Southwell, "Antireflection Index Matching on Optical Surfaces," *J. Opt. Soc. Am. A*, vol. 8, no. 3, pp. 549–553, 1991.

[23] A. Deinega, I. Valuev, B. Potapkin, and Y. Lozovik, "Minimizing light reflection from dielectric textured surfaces," *J. Opt. Soc. Am. A*, vol. 28, no. 5, p. 770, 2011, doi: 10.1364/josaa.28.000770.

[24] T. Zhang, P. Zhang, S. Li, W. Li, Z. Wu, and Y. Jiang, "Black silicon with self-cleaning surface prepared by wetting processes," *Nanoscale Res. Lett.*, vol. 8, no. 1, pp. 1–5, 2013, doi: 10.1186/1556-276X-8-351.

[25] Y. Liu, A. Das, Z. Lin, I. B. Cooper, A. Rohatgi, and C. P. Wong, "Hierarchical robust textured structures for large scale self-cleaning black silicon solar cells," *Nano Energy*, vol. 3, pp. 127–133, 2014, doi: 10.1016/j.nanoen.2013.11.002.

[26] Y. J. Peng, H. X. Huang, and H. Xie, "Rapid fabrication of antireflective pyramid structure on polystyrene film used as protective layer of solar cell," *Sol. Energy Mater. Sol. Cells*, vol. 171, no. May, pp. 98–105, 2017, doi: 10.1016/j.solmat.2017.06.013.

[27] P. Campbell and M. A. Green, "Light trapping properties of pyramidally textured surfaces," *J. Appl. Phys.*, vol. 62, no. 1, pp. 243–249, 1987, doi: 10.1063/1.339189.

[28] D. Z. Dimitrov and C. H. Du, "Crystalline silicon solar cells with micro/nano texture," *Appl. Surf. Sci.*, vol. 266, pp. 1–4, 2013, doi: 10.1016/j.apsusc.2012.10.081.

[29] A. Peter Amalathas and M. M. Alkaisi, "Efficient light trapping nanopyramid

structures for solar cells patterned using UV nanoimprint lithography," *Mater. Sci. Semicond. Process.*, vol. 57, no. October 2016, pp. 54–58, 2017, doi: 10.1016/j.mssp.2016.09.032.

[30] A. Mavrokefalos, S. E. Han, S. Yerci, M. S. Branham, and G. Chen, "Efficient light trapping in inverted nanopyramid thin crystalline silicon membranes for solar cell applications," *Nano Lett.*, vol. 12, no. 6, pp. 2792–2796, 2012, doi: 10.1021/nl2045777.

[31] J. Zhu *et al.*, "Optical absorption enhancement in amorphous silicon nanowire and nanocone arrays," *Nano Lett.*, vol. 9, no. 1, pp. 279–282, 2009, doi: 10.1021/nl802886y.

[32] P. Singh *et al.*, "Fabrication of vertical silicon nanowire arrays on three-dimensional micro-pyramid-based silicon substrate," *J. Mater. Sci.*, vol. 50, no. 20, pp. 6631–6641, 2015, doi: 10.1007/s10853-015-9210-y.

[33] T. Rahman, M. Navarro-Cía, and K. Fobelets, "High density micro-pyramids with silicon nanowire array for photovoltaic applications," *Nanotechnology*, vol. 25, no. 48, 2014, doi: 10.1088/0957-4484/25/48/485202.

[34] Y. Liu *et al.*, "Hybridizing ZnO nanowires with micropyramid silicon wafers as superhydrophobic high-efficiency solar cells," *Adv. Energy Mater.*, vol. 2, no. 1, pp. 47–51, 2012, doi: 10.1002/aenm.201100287.

[35] B. D. Choudhury, A. Abedin, A. Dev, R. Sanatinia, and S. Anand, "Silicon micro-structure and ZnO nanowire hierarchical assortments for light management," *Opt. Mater. Express*, vol. 3, no. 8, p. 1039, 2013, doi: 10.1364/ome.3.001039.

[36] W. R. Wei *et al.*, "Above-11%-efficiency organic-inorganic hybrid solar cells with omnidirectional harvesting characteristics by employing hierarchical photon-trapping structures," *Nano Lett.*, vol. 13, no. 8, pp. 3658–3663, 2013, doi: 10.1021/nl401540h.

[37] H. Sai, H. Yugami, Y. Kanamori, and K. Hane, "Solar selective absorbers based on two-dimensional W surface gratings with submicron periods for high-temperature photothermal conversion," *Sol. Energy Mater. Sol. Cells*, vol. 79, no. 1, pp. 35–49, 2003, doi: 10.1016/S0927-0248(02)00364-1.

[38] H. Zhang *et al.*, "Biologically inspired flexible photonic films for efficient passive radiative cooling," *Proc. Natl. Acad. Sci.*, vol. 117, no. 26, p. 202001802, 2020, doi: 10.1073/pnas.2001802117.

[39] P. Nagpal, N. C. Lindquist, S. H. Oh, and D. J. Norris, "Ultrasmooth patterned metals for plasmonics and metamaterials," *Science (80-.).*, vol. 325, no. 5940, pp. 594–597, 2009, doi: 10.1126/science.1174655.

[40] J. H. Park, P. Nagpal, K. M. McPeak, N. C. Lindquist, S. H. Oh, and D. J. Norris, "Fabrication of smooth patterned structures of refractory metals, semiconductors, and oxides via template stripping," *ACS Appl. Mater. Interfaces*, vol. 5, no. 19, pp.

9701–9708, 2013, doi: 10.1021/am402756d.

[41] H. Lu and C. Gang, “Analysis of optical absorption in silicon nanowire arrays for photovoltaic applications,” *Nano Lett.*, vol. 7, no. 11, pp. 3249–3252, 2007, doi: 10.1021/nl071018b.

[42] A. R. Zanatta, “Revisiting the optical bandgap of semiconductors and the proposal of a unified methodology to its determination,” *Sci. Rep.*, vol. 9, no. 1, p. 11225, 2019, doi: 10.1038/s41598-019-47670-y.

[43] S. Ge *et al.*, “Design and preparation of a micro-pyramid structured thin film for broadband infrared antireflection,” *Coatings*, vol. 8, no. 5, 2018, doi: 10.3390/coatings8050192.

[44] H. Sai, H. Yugami, Y. Akiyama, Y. Kanamori, and K. Hane, “Spectral control of thermal emission by periodic microstructured surfaces in the near-infrared region,” *J. Opt. Soc. Am. A*, vol. 18, no. 7, p. 1471, 2001, doi: 10.1364/josaa.18.001471.

[45] Y. Nishijima, R. Komatsu, S. Ota, G. Seniutinas, A. Balčytis, and S. Juodkazis, “Anti-reflective surfaces: Cascading nano/microstructuring,” *APL Photonics*, vol. 1, no. 7, 2016, doi: 10.1063/1.4964851.

[46] D. Wu *et al.*, “The design of ultra-broadband selective near-perfect absorber based on photonic structures to achieve near-ideal daytime radiative cooling,” *Mater. Des.*, vol. 139, pp. 104–111, 2018, doi: 10.1016/j.matdes.2017.10.077.

[47] L. Zhou, X. Yu, and J. Zhu, “Metal-core/semiconductor-shell nanocones for broadband solar absorption enhancement,” *Nano Lett.*, vol. 14, no. 2, pp. 1093–1098, 2014, doi: 10.1021/nl500008y.

[48] X. Yin, R. Yang, G. Tan, and S. Fan, “Terrestrial radiative cooling: Using the cold universe as a renewable and sustainable energy source,” *Science (80-.).*, vol. 370, no. 6518, pp. 786–791, 2020, doi: 10.1126/science.abb0971.

[49] A. Krishna, J. M. Kim, J. Leem, M. C. Wang, S. Nam, and J. Lee, “Ultraviolet to Mid-Infrared Emissivity Control by Mechanically Reconfigurable Graphene,” *Nano Lett.*, vol. 19, no. 8, pp. 5086–5092, 2019, doi: 10.1021/acs.nanolett.9b01358.

[50] M. Sala-Casanovas, A. Krishna, Z. Yu, and J. Lee, “Bio-Inspired Stretchable Selective Emitters Based on Corrugated Nickel for Personal Thermal Management,” *Nanoscale Microscale Thermophys. Eng.*, vol. 23, no. 3, pp. 173–187, 2019, doi: 10.1080/15567265.2019.1586017.

[51] J. Mandal *et al.*, “Hierarchically porous polymer coatings for highly efficient passive daytime radiative cooling,” *Science (80-.).*, vol. 362, no. 6412, pp. 315–319, 2018, doi: 10.1126/science.aat9513.

[52] J. J. D. Leon, A. M. Hiszpanski, T. C. Bond, and J. D. Kuntz, “Design Rules for Tailoring Antireflection Properties of Hierarchical Optical Structures,” *Adv. Opt. Mater.*, vol. 5, no. 13, pp. 1–8, 2017, doi: 10.1002/adom.201700080.

[53] J. Seo *et al.*, "Design of a Broadband Solar Thermal Absorber Using a Deep Neural Network and Experimental Demonstration of Its Performance," *Sci. Rep.*, vol. 9, no. 1, pp. 1–9, 2019, doi: 10.1038/s41598-019-51407-2.

[54] S. Haghanifar, M. McCourt, B. Cheng, J. Wuenschell, P. Ohodnicki, and P. W. Leu, "Discovering high-performance broadband and broad angle antireflection surfaces by machine learning," *Optica*, vol. 7, no. 7, 2020.

[55] M. Elzouka, C. Yang, A. Albert, R. S. Prasher, and S. D. Lubner, "Interpretable Forward and Inverse Design of Particle Spectral Emissivity Using Common Machine-Learning Models," *Cell Reports Phys. Sci.*, vol. 1, no. 12, p. 100259, 2020, doi: 10.1016/j.xcrp.2020.100259.

[56] "Finite Difference Time Domain (FDTD) solver introduction – Lumerical Support." https://support.lumerical.com/hc/en-us/articles/360034914633-Finite-Difference-Time-Domain-FDTD-solver-introduction (accessed Jun. 03, 2020).

[57] H. Wang and L. Wang, "Perfect selective metamaterial solar absorbers," *Opt. Express*, vol. 21, no. S6, p. A1078, 2013, doi: 10.1364/oe.21.0a1078.

[58] D. L. C. Chan, M. Soljačić, and J. D. Joannopoulos, "Thermal emission and design in one-dimensional periodic metallic photonic crystal slabs," *Phys. Rev. E - Stat. Nonlinear, Soft Matter Phys.*, vol. 74, no. 1, pp. 206–214, 2006, doi: 10.1103/PhysRevE.74.016609.

[59] R. H. Byrd, J. C. Gilbert, and J. Nocedal, "A trust region method based on interior point techniques for nonlinear programming," *Math. Program. Ser. B*, vol. 89, no. 1, pp. 149–185, 2000, doi: 10.1007/PL00011391.

[60] R. Poli, J. Kennedy, and T. Blackwell, "Particle swarm optimization An overview," pp. 33–57, 2007, doi: 10.1007/s11721-007-0002-0.

[61] D. Whitley, "A genetic algorithm tutorial," 1994.

[62] A. Srinivasan, B. Czapla, J. Mayo, and A. Narayanaswamy, "Infrared dielectric function of polydimethylsiloxane and selective emission behavior," *Appl. Phys. Lett.*, vol. 109, no. 6, 2016, doi: 10.1063/1.4961051.

[63] S. Chattopadhyay, Y. F. Huang, Y. J. Jen, A. Ganguly, K. H. Chen, and L. C. Chen, "Anti-reflecting and photonic nanostructures," *Materials Science and Engineering R: Reports*, vol. 69, no. 1–3. Elsevier Ltd, pp. 1–35, Jun. 20, 2010, doi: 10.1016/j.mser.2010.04.001.

[64] J. C. . Garnett, "Colours in Metal Glasses and Films," *Philos. Trans. R. Soc. A Math. Phys. Eng. Sci.*, vol. 203, p. 385, 1904.

[65] J. C. M. Garnett, "Colours in Metal Glasses, in Metallic Films, and in Metallic Solutions - II.," *Philos. Trans. R. Soc. A Math. Phys. Eng. Sci.*, vol. 205, p. 237, 1906.

[66] Von D. A. G. Bruggeman, "Berechnzcrrg verschCedcner physikalducher Eonstanten von heterogenew Yuhstan.xen 1.," *Ann. Phys.*, 1935.

[67] R. T. Kivaisi and L. Stensland, “Spectral selectivity of nickel and chromium rough surfaces,” *Appl. Phys. A Solids Surfaces*, vol. 27, no. 4, pp. 233–238, 1982, doi: 10.1007/BF00619084.

[68] H. G. Craighead, R. E. Howard, and D. M. Tennant, “Selectively emissive refractory metal surfaces,” *Appl. Phys. Lett.*, vol. 38, no. 2, pp. 74–76, 1981, doi: 10.1063/1.92253.

[69] E. D. Palik, *Handbook of Optical Constants of Solids*. Orlando: Academic Press, 1985.

[70] H. A. Macleod, *Thin-Film Optical Filters*. 1986.

[71] M. G. Moharam and T. K. Gaylord, “Rigorous coupled-wave analysis of planar-grating diffraction,” vol. 71, no. 7, 1981.

[72] M. G. Moharam and T. K. Gaylord, “Diffraction Analysis of Dielectric Surface-Relief Gratings.,” *J. Opt. Soc. Am.*, vol. 72, no. 10, pp. 1385–1392, 1982, doi: 10.1364/JOSA.72.001385.

[73] K. E. Torrance and E. M. Sparrow, “Theory for Off-Specular Reflection From Roughened Surfaces*,” *J. Opt. Soc. Am.*, vol. 57, no. 9, p. 1105, 1967, doi: 10.1364/josa.57.001105.

[74] K. Han and C. Chang, “Numerical Modeling of Sub-Wavelength Anti-Reflective Structures for Solar Module Applications,” pp. 87–128, 2014, doi: 10.3390/nano4010087.

[75] K. A. Shore, *Numerical methods in photonics, by Andrei V. Lavrinenko, Jesper Laegsgaard, Niles Gregersen, Frank Schmidt, and Thomas Sondergaard*, vol. 57, no. 2. 2016.

[76] I. Malkiel, M. Mrejen, A. Nagler, U. Arieli, L. Wolf, and H. Suchowski, “Plasmonic nanostructure design and characterization via Deep Learning,” *Light Sci. Appl.*, vol. 7, no. 1, 2018, doi: 10.1038/s41377-018-0060-7.

[77] M. Bojarski *et al.*, “End to End Learning for Self-Driving Cars,” pp. 1–9, 2016, [Online]. Available: http://arxiv.org/abs/1604.07316.

[78] G. Hinton *et al.*, “Deep neural networks for acoustic modeling in speech recognition: The shared views of four research groups,” *IEEE Signal Process. Mag.*, vol. 29, no. 6, pp. 16–17, 2012, doi: 10.1109/MSP.2012.2209906.

[79] S. T. Spantideas, A. E. Giannopoulos, N. C. Kapsalis, and C. N. Capsalis, “A Deep Learning Method for Modeling the Magnetic Signature of Spacecraft Equipment Using Multiple Magnetic Dipoles,” *IEEE Magn. Lett.*, vol. 12, 2021, doi: 10.1109/LMAG.2021.3069374.

[80] Y. Xiong, L. Guo, D. Tian, Y. Zhang, and C. Liu, “Intelligent optimization strategy based on statistical machine learning for spacecraft thermal design,” *IEEE Access*, vol. 8, pp. 204268–204282, 2020, doi: 10.1109/ACCESS.2020.3036548.

[81] C. Zhang, “A statistical machine learning based modeling and exploration framework

for run-time cross-stack energy optimization," University of North Carolina at Charlotte, 2013.

[82] W. Zhu, M. Gan, B. Ye, X. Xiong, J. Feng, and X. Chong, "Optimization of the thermophysical properties of the thermal barrier coating materials based on GA-SVR machine learning method: Illustrated with ZrO2doped DyTaO4system," *Mater. Res. Express*, vol. 8, no. 12, 2021, doi: 10.1088/2053-1591/ac3d5b.

[83] T. Zhang *et al.*, "Machine learning and evolutionary algorithm studies of graphene metamaterials for optimized plasmon-induced transparency," *Opt. Express*, vol. 28, no. 13, p. 18899, 2020, doi: 10.1364/oe.389231.

[84] X. Li, J. Shu, W. Gu, and L. Gao, "Deep neural network for plasmonic sensor modeling," *Opt. Mater. Express*, vol. 9, no. 9, p. 3857, 2019, doi: 10.1364/ome.9.003857.

[85] J. Baxter, A. Calà Lesina, J. M. Guay, A. Weck, P. Berini, and L. Ramunno, "Plasmonic colours predicted by deep learning," *Sci. Rep.*, vol. 9, no. 1, pp. 1–19, 2019, doi: 10.1038/s41598-019-44522-7.

[86] J. He, C. He, C. Zheng, Q. Wang, and J. Ye, "Plasmonic nanoparticle simulations and inverse design using machine learning," *Nanoscale*, vol. 11, no. 37, pp. 17444–17459, 2019, doi: 10.1039/c9nr03450a.

[87] I. Sajedian, J. Kim, and J. Rho, "Finding the optical properties of plasmonic structures by image processing using a combination of convolutional neural networks and recurrent neural networks," *Microsystems Nanoeng.*, vol. 5, no. 1, 2019, doi: 10.1038/s41378-019-0069-y.

[88] S. Han, J. H. Shin, P. H. Jung, H. Lee, and B. J. Lee, "Broadband Solar Thermal Absorber Based on Optical Metamaterials for High-Temperature Applications," *Adv. Opt. Mater.*, vol. 4, no. 8, pp. 1265–1273, 2016, doi: 10.1002/adom.201600236.

[89] C. C. Nadell, B. Huang, J. M. Malof, and W. J. Padilla, "Deep learning for accelerated all-dielectric metasurface design," *Opt. Express*, vol. 27, no. 20, p. 27523, 2019, doi: 10.1364/oe.27.027523.

[90] T. Deppe and J. Munday, "Nighttime Photovoltaic Cells: Electrical Power Generation by Optically Coupling with Deep Space," *ACS Photonics*, 2019, doi: 10.1021/acsphotonics.9b00679.

[91] W. Ma, F. Cheng, and Y. Liu, "Deep-Learning-Enabled On-Demand Design of Chiral Metamaterials," *ACS Nano*, vol. 12, no. 6, pp. 6326–6334, 2018, doi: 10.1021/acsnano.8b03569.

[92] Y. Li *et al.*, "Self-Learning Perfect Optical Chirality via a Deep Neural Network," *Phys. Rev. Lett.*, vol. 123, no. 21, pp. 1–6, 2019, doi: 10.1103/PhysRevLett.123.213902.

[93] I. Balin, V. Garmider, Y. Long, and I. Abdulhalim, " Training artificial neural network for optimization of nanostructured VO 2 -based smart window performance ," *Opt. Express*, vol. 27, no. 16, p. A1030, 2019, doi: 10.1364/oe.27.0a1030.

[94] J. Peurifoy *et al.*, "Nanophotonic particle simulation and inverse design using artificial neural networks," *arXiv*, no. June, pp. 1–8, 2017, doi: 10.1117/12.2289195.

[95] S. An *et al.*, "A Deep Learning Approach for Objective-Driven All-Dielectric Metasurface Design," *ACS Photonics*, vol. 6, no. 12, pp. 3196–3207, 2019, doi: 10.1021/acsphotonics.9b00966.

[96] L. Gao, X. Li, D. Liu, L. Wang, and Z. Yu, "A Bidirectional Deep Neural Network for Accurate Silicon Color Design," *Adv. Mater.*, vol. 31, no. 51, pp. 1–7, 2019, doi: 10.1002/adma.201905467.

[97] P. R. Wiecha, A. Arbouet, C. Girard, and O. L. Muskens, "Deep learning in nano-photonics: Inverse design and beyond," *arXiv*, vol. 9, no. 5, pp. 182–200, 2020, doi: 10.1364/prj.415960.

[98] S. Wu *et al.*, "Machine-learning-assisted discovery of polymers with high thermal conductivity using a molecular design algorithm," *npj Comput. Mater.*, vol. 5, no. 1, 2019, doi: 10.1038/s41524-019-0203-2.

[99] H. Wei, S. Zhao, Q. Rong, and H. Bao, "Predicting the effective thermal conductivities of composite materials and porous media by machine learning methods," *Int. J. Heat Mass Transf.*, vol. 127, pp. 908–916, 2018, doi: 10.1016/j.ijheatmasstransfer.2018.08.082.

[100] T. Zhan, L. Fang, and Y. Xu, "Prediction of thermal boundary resistance by the machine learning method," *Sci. Rep.*, vol. 7, no. 1, pp. 1–2, 2017, doi: 10.1038/s41598-017-07150-7.

[101] A. B. Farimani, J. Gomes, and V. S. Pande, "Deep Learning the Physics of Transport Phenomena," vol. 94305, 2017, [Online]. Available: http://arxiv.org/abs/1709.02432.

[102] S. J. Park, B. Bae, J. Kim, and M. Swaminathan, "Application of machine learning for optimization of 3-D integrated circuits and systems," *IEEE Trans. Very Large Scale Integr. Syst.*, vol. 25, no. 6, pp. 1856–1865, 2017, doi: 10.1109/TVLSI.2017.2656843.

[103] Y. Liu, N. Dinh, Y. Sato, and B. Niceno, "Data-driven modeling for boiling heat transfer: Using deep neural networks and high-fidelity simulation results," *Appl. Therm. Eng.*, vol. 144, pp. 305–320, 2018, doi: 10.1016/j.applthermaleng.2018.08.041.

[104] Z. A. Kudyshev, A. V. Kildishev, V. M. Shalaev, and A. Boltasseva, "Machine-learning-assisted metasurface design for high-efficiency thermal emitter optimization," *Appl. Phys. Rev.*, vol. 7, no. 2, 2020, doi: 10.1063/1.5134792.

[105] W. Zhang, B. Wang, and C. Zhao, "Selective Thermophotovoltaic Emitter with Aperiodic Multilayer Structures Designed by Machine Learning," *ACS Appl. Energy Mater.*, vol. 4, no. 2, pp. 2004–2013, 2021, doi: 10.1021/acsaem.0c03201.

[106] T. Karras, S. Laine, M. Aittala, J. Hellsten, J. Lehtinen, and T. Aila, "Analyzing and improving the image quality of StyleGAN," *arXiv*, pp. 8110–8119, 2019.

[107] J. J. García-Esteban, J. Bravo-Abad, and J. C. Cuevas, "Deep Learning for the Modeling and Inverse Design of Radiative Heat Transfer," *Phys. Rev. Appl.*, vol. 16, no. 6, p. 1, 2021, doi: 10.1103/PhysRevApplied.16.064006.

[108] J. Tausendschön and S. Radl, "Deep neural network-based heat radiation modelling between particles and between walls and particles," *Int. J. Heat Mass Transf.*, vol. 177, 2021, doi: 10.1016/j.ijheatmasstransfer.2021.121557.

[109] H. H. Kang, M. Kaya, and S. Hajimirza, "A data driven artificial neural network model for predicting radiative properties of metallic packed beds," *J. Quant. Spectrosc. Radiat. Transf.*, vol. 226, pp. 66–72, 2019, doi: 10.1016/j.jqsrt.2019.01.013.

[110] Z. Yu, X. Nie, A. Yuksel, and J. Lee, "Reflectivity of solid and hollow microsphere composites and the effects of uniform and varying diameters," *J. Appl. Phys.*, vol. 128, no. 5, 2020, doi: 10.1063/5.0015650.

[111] Y. Lecun, Y. Bengio, and G. Hinton, "Deep learning," *Nature*, vol. 521, no. 7553, pp. 436–444, 2015, doi: 10.1038/nature14539.

[112] C. Zuo *et al.*, *Deep learning in optical metrology: a review*, vol. 11, no. 1. Springer US, 2022.

[113] T. Ma, Z. Guo, M. Lin, and Q. Wang, "Recent trends on nanofluid heat transfer machine learning research applied to renewable energy," *Renew. Sustain. Energy Rev.*, vol. 138, no. October 2020, p. 110494, 2021, doi: 10.1016/j.rser.2020.110494.

[114] Y. Song, J. Liang, J. Lu, and X. Zhao, "An efficient instance selection algorithm for k nearest neighbor regression," *Neurocomputing*, vol. 251, pp. 26–34, 2017, doi: 10.1016/j.neucom.2017.04.018.

[115] R. M. Balabin and E. I. Lomakina, "Support vector machine regression (LS-SVM)an alternative to artificial neural networks (ANNs) for the analysis of quantum chemistry data," *Phys. Chem. Chem. Phys.*, vol. 13, no. 24, pp. 11710–11718, 2011, doi: 10.1039/c1cp00051a.

[116] J. Sullivan, Z. Yu, and J. Lee, "Optical Analysis and Optimization of Micropyramid Texture for Thermal Radiation Control," *Nanoscale Microscale Thermophys. Eng.*, 2021, doi: 10.1080/15567265.2021.1958960.

[117] F. Chollet, "Keras," 2015. https://github.com/fchollet/keras.

[118] L. Li, K. Jamieson, G. DeSalvo, A. Rostamizadeh, and A. Talwalkar, "Hyperband: A novel bandit-based approach to hyperparameter optimization," *J. Mach. Learn. Res.*, vol. 18, pp. 1–52, 2018.

[119] H. U. Yang, J. D'Archangel, M. L. Sundheimer, E. Tucker, G. D. Boreman, and M. B. Raschke, "Optical dielectric function of silver," *Phys. Rev. B - Condens. Matter Mater. Phys.*, vol. 91, no. 23, pp. 1–11, 2015, doi: 10.1103/PhysRevB.91.235137.

[120] M. J. Weber, *Handbook of Optical Materials*, vol. 3. 2003.

[121] M. A. Ordal, R. J. Bell, R. W. Alexander, L. A. Newquist, and M. R. Querry, "Optical

properties of Al, Fe, Ti, Ta, W, and Mo at submillimeter wavelengths," *Appl. Opt.*, vol. 27, no. 6, p. 1203, 1988, doi: 10.1364/ao.27.001203.

[122] C. Wan *et al.*, "On the Optical Properties of Thin-Film Vanadium Dioxide from the Visible to the Far Infrared," *Ann. Phys.*, vol. 1900188, p. 1900188, 2019, doi: 10.1002/andp.201900188.

[123] J. I. Larruquert, A. P. Pérez-Marín, S. García-Cortés, L. Rodríguez-de Marcos, J. A. Aznárez, and J. A. Méndez, "Self-consistent optical constants of SiC thin films," *J. Opt. Soc. Am. A*, vol. 28, no. 11, p. 2340, 2011, doi: 10.1364/josaa.28.002340.

[124] H. R. Phillip and E. A. Taft, "Kramers-Kronig Analysis of Reflectance Data for Diamond," *Phys. Rev.*, vol. 136, no. 5A, 1964, doi: 10.1103/PhysRev.136.A1445.

[125] J. Kischkat *et al.*, "Mid-infrared optical properties of thin films of aluminum oxide, titanium dioxide, silicon dioxide, aluminum nitride, and silicon nitride," *Appl. Opt.*, vol. 51, no. 28, pp. 6789–6798, 2012, doi: 10.1364/AO.51.006789.

[126] S. Babar and J. H. Weaver, "Optical constants of Cu, Ag, and Au revisited," *Appl. Opt.*, vol. 54, no. 3, p. 477, 2015, doi: 10.1364/ao.54.000477.

[127] J. I. Larruquert, A. P. Pérez-marín, S. García-cortés, L. R. Marcos, J. A. Aznárez, and J. A. Méndez, "Self-consistent optical constants of sputter-deposited B 4 C thin films," vol. 29, no. 1, pp. 117–123, 2012.

[128] M. R. Querry, "From the Millimeter To the Ultraviolet," 1987.

[129] A. D. Rakić, A. B. Djurišić, J. M. Elazar, and M. L. Majewski, "Optical properties of metallic films for vertical-cavity optoelectronic devices," *Appl. Opt.*, vol. 37, no. 22, p. 5271, 1998, doi: 10.1364/ao.37.005271.

[130] M. R. Querry, "Optical Constants, Report No. AD-A158 623," *Crdc*, vol. CR-85034, pp. 1–413, 1985, [Online]. Available: https://apps.dtic.mil/dtic/tr/fulltext/u2/a158623.pdf.

[131] R. Y. Koyama, N. V. Smith, and W. E. Spicer, "Optical properties of indium," *Phys. Rev. B*, vol. 8, no. 6, pp. 2426–2432, 1973, doi: 10.1103/PhysRevB.8.2426.

[132] A. You, M. A. Y. Be, and I. In, "Optical dispersion relations for GaP, GaAs, GaSb, InP, InAs, InSb, Al," vol. 6030, no. August 1989, 1998.

[133] M. Rasigni and G. Rasigni, "Optical constants of lithium deposits as determined from the Kramers-Kronig analysis," *J. Opt. Soc. Am.*, vol. 67, no. 1, p. 54, 1977, doi: 10.1364/josa.67.000054.

[134] H. J. Hagemann, W. Gudat, and C. Kunz, "OPTICAL CONSTANTS FROM THE FAR INFRARED TO THE X-RAY REGION: Mg, Al, Cu, Ag, Au, Bi, C, and Al2O3.," *J Opt Soc Am*, vol. 65, no. 6, pp. 742–744, 1975, doi: 10.1364/JOSA.65.000742.

[135] A. I. Golovashkin, I. E. Leksina, G. P. Motulevhich, and A. A. Shubin, "The optical properties of Niobium," *Sov. Phys. JetP*, vol. 29, no. 1, pp. 27–34, 1969.

[136] V. V Nemoshkalenko, V. N. Antonov, M. M. Kirillova, A. E. Krasovskii, and L. V. Nomerovannaya, "The Structure and Energy Bands and Optical Absoprtion in Osmium," *Sov. JetP*, vol. 63, no. 1, p. 115, 1986.

[137] Q. Li, W. Cai, X. Wang, Y. Zhou, D. D. Feng, and M. Chen, "Medical image classification with convolutional neural network," *2014 13th Int. Conf. Control Autom. Robot. Vision, ICARCV 2014*, vol. 2014, no. December, pp. 844–848, 2014, doi: 10.1109/ICARCV.2014.7064414.

[138] A. G. Howard, "Some improvements on deep convolutional neural network based image classification," *2nd Int. Conf. Learn. Represent. ICLR 2014 - Conf. Track Proc.*, 2014.

[139] W. Ma *et al.*, "Image-driven discriminative and generative machine learning algorithms for establishing microstructure-processing relationships," *J. Appl. Phys.*, vol. 128, no. 13, 2020, doi: 10.1063/5.0013720.

[140] A. Baskaran, E. J. Kautz, A. Chowdhary, W. Ma, B. Yener, and D. J. Lewis, "Adoption of Image-Driven Machine Learning for Microstructure Characterization and Materials Design: A Perspective," *Jom*, vol. 73, no. 11, pp. 3639–3657, 2021, doi: 10.1007/s11837-021-04805-9.

[141] H. S. Stein, D. Guevarra, P. F. Newhouse, E. Soedarmadji, and J. M. Gregoire, "Machine learning of optical properties of materials-predicting spectra from images and images from spectra," *Chem. Sci.*, vol. 10, no. 1, pp. 47–55, 2019, doi: 10.1039/C8SC03077D.

[142] S. So and J. Rho, "Designing nanophotonic structures using conditional deep convolutional generative adversarial networks," *Nanophotonics*, vol. 8, no. 7, pp. 1255–1261, 2019, doi: 10.1515/nanoph-2019-0117.

[143] W. Ma, Z. Liu, Z. A. Kudyshev, A. Boltasseva, W. Cai, and Y. Liu, "Deep learning for the design of photonic structures," *Nat. Photonics*, vol. 15, no. 2, pp. 77–90, 2021, doi: 10.1038/s41566-020-0685-y.

[144] Z. Yang, X. Li, L. C. Brinson, A. N. Choudhary, W. Chen, and A. Agrawal, "Microstructural materials design via deep adversarial learning methodology," *J. Mech. Des. Trans. ASME*, vol. 140, no. 11, pp. 1–10, 2018, doi: 10.1115/1.4041371.

[145] S. An *et al.*, "Multifunctional Metasurface Design with a Generative Adversarial Network," *Adv. Opt. Mater.*, vol. 9, no. 5, pp. 1–10, 2021, doi: 10.1002/adom.202001433.

[146] J. Sullivan, A. Mirhashemi, and J. Lee, "Deep learning based analysis of microstructured materials for thermal radiation control," *Sci. Rep.*, vol. 12, no. 1, pp. 1–14, 2022, doi: 10.1038/s41598-022-13832-8.

[147] Kane Yee, "Numerical solution of initial boundary value problems involving maxwell's equations in isotropic media," *IEEE Trans. Antennas Propag.*, vol. 14, no. 3, pp. 302–307, May 1966, doi: 10.1109/TAP.1966.1138693.

[148] T. N. Sainath, O. Vinyals, A. Senior, and H. Sak, "Convolutional, Long Short-Term Memory, fully connected Deep Neural Networks," *ICASSP, IEEE Int. Conf. Acoust. Speech Signal Process. - Proc.*, vol. 2015-Augus, pp. 4580–4584, 2015, doi: 10.1109/ICASSP.2015.7178838.

[149] K. Bock and S. M. Garnsey, "Language Processing," in *A Companion to Cognitive Science*, vol. 349, no. 6245, Oxford, UK: Blackwell Publishing Ltd, 2017, pp. 226–234.

[150] Y. Suh, R. Bostanabad, and Y. Won, "Deep learning predicts boiling heat transfer," *Sci. Rep.*, vol. 11, no. 1, pp. 1–10, 2021, doi: 10.1038/s41598-021-85150-4.

[151] D. Lee, S. Jiang, O. Balogun, and W. Chen, "Dynamic Control of Plasmonic Localization by Inverse Optimization of Spatial Phase Modulation," *ACS Photonics*, vol. 9, no. 2, pp. 351–359, 2022, doi: 10.1021/acsphotonics.1c01043.

[152] W. Ma, F. Cheng, Y. Xu, Q. Wen, and Y. Liu, "Probabilistic Representation and Inverse Design of Metamaterials Based on a Deep Generative Model with Semi-Supervised Learning Strategy," *Adv. Mater.*, vol. 31, no. 35, pp. 1–9, 2019, doi: 10.1002/adma.201901111.

[153] S. Molesky, Z. Lin, A. Y. Piggott, W. Jin, J. Vucković, and A. W. Rodriguez, "Inverse design in nanophotonics," *Nat. Photonics*, vol. 12, no. 11, pp. 659–670, 2018, doi: 10.1038/s41566-018-0246-9.

[154] Z. A. Kudyshev, A. V. Kildishev, V. M. Shalaev, and A. Boltasseva, "Machine learning-assisted global optimization of photonic devices," *Front. Opt. Photonics*, vol. 10, no. 1, pp. 381–393, 2021, doi: 10.1515/9783110710687-028.

[155] V. Kalt, A. K. González-Alcalde, S. Es-Saidi, R. Salas-Montiel, S. Blaize, and D. Macías, "Metamodeling of high-contrast-index gratings for color reproduction," *J. Opt. Soc. Am. A*, vol. 36, no. 1, p. 79, 2019, doi: 10.1364/josaa.36.000079.

[156] D. Liu, Y. Tan, E. Khoram, and Z. Yu, "Training Deep Neural Networks for the Inverse Design of Nanophotonic Structures," *ACS Photonics*, vol. 5, no. 4, pp. 1365–1369, 2018, doi: 10.1021/acsphotonics.7b01377.

[157] Z. Liu, D. Zhu, S. P. Rodrigues, K. T. Lee, and W. Cai, "Generative Model for the Inverse Design of Metasurfaces," *Nano Lett.*, vol. 18, no. 10, pp. 6570–6576, 2018, doi: 10.1021/acs.nanolett.8b03171.

[158] X. Shi, T. Qiu, J. Wang, X. Zhao, and S. Qu, "Metasurface inverse design using machine learning approaches," *J. Phys. D. Appl. Phys.*, vol. 53, no. 27, 2020, doi: 10.1088/1361-6463/ab8036.

[159] L. Deng, Y. Xu, and Y. Liu, "Hybrid inverse design of photonic structures by combining optimization methods with neural networks," *Photonics Nanostructures - Fundam. Appl.*, vol. 52, no. August, p. 101073, 2022, doi: 10.1016/j.photonics.2022.101073.

[160] X. Jiang, H. Ma, J. Huang, D. Chen, Z. Zhang, and J. Yang, "Implementation of radiative cooling with an inverse-designed selective emitter," *Opt. Commun.*, vol. 497, no. March, p. 127209, 2021, doi: 10.1016/j.optcom.2021.127209.

[161] R. Dong, Y. Dan, X. Li, and J. Hu, "Inverse design of composite metal oxide optical materials based on deep transfer learning and global optimization," *Comput. Mater. Sci.*, vol. 188, no. November 2020, p. 110166, 2021, doi: 10.1016/j.commatsci.2020.110166.

[162] X. Jiang *et al.*, "Tunable mid-infrared selective emitter based on inverse design metasurface for infrared stealth with thermal management," *Opt. Express*, vol. 30, no. 11, p. 18250, 2022, doi: 10.1364/oe.456791.

[163] X. Jiang *et al.*, "Metasurface Based on Inverse Design for Maximizing Solar Spectral Absorption," *Adv. Opt. Mater.*, vol. 9, no. 19, pp. 1–11, 2021, doi: 10.1002/adom.202100575.

[164] J. Sullivan, Z. Yu, and J. Lee, "Nanometer-Thick Nickel Coatings on Silicon Micropyramids for Infrared Absorption," *ACS Appl. Nano Mater.*, vol. 5, no. 4, pp. 4615–4622, 2022, doi: 10.1021/acsanm.2c00541.

[165] Y. Zhai, Y. Li, J. Ji, Z. Wu, and Q. Wang, "Hot Electron Generation in Silicon Micropyramids Covered with Nanometer-Thick Gold Films for Near-Infrared Photodetectors," *ACS Appl. Nano Mater.*, vol. 3, no. 1, pp. 149–155, 2020, doi: 10.1021/acsanm.9b01840.

[166] X. Nie, Z. Yu, E. Jackson, and J. Lee, "Refractive index and extinction coefficient of hollow microspheres for solar reflection," *Appl. Phys. Lett.*, vol. 118, no. 21, 2021, doi: 10.1063/5.0049018.

[167] D. Lee *et al.*, "Long short-term memory recurrent neural network-based acoustic model using connectionist temporal classification on a large-scale training corpus," *China Commun.*, vol. 14, no. 9, pp. 23–31, 2017, doi: 10.1109/CC.2017.8068761.

[168] Y. Xiu, L. Zhu, D. W. Hess, and C. P. Wong, "Hierarchical silicon etched structures for controlled hydrophobicity/ superhydrophobicity," *Nano Lett.*, vol. 7, no. 11, pp. 3388–3393, Nov. 2007, doi: 10.1021/nl0717457.

[169] K. C. Park, H. J. Choi, C. H. Chang, R. E. Cohen, G. H. McKinley, and G. Barbastathis, "Nanotextured silica surfaces with robust superhydrophobicity and omnidirectional broadband supertransmissivity," *ACS Nano*, vol. 6, no. 5, pp. 3789–3799, 2012, doi: 10.1021/nn301112t.

[170] P. Nagpal, N. C. Lindquist, S. Oh, and D. J. Norris, "for Plasmonics and Metamaterials," no. July, pp. 594–598, 2009.

[171] V. E. Ferry, J. N. Munday, and H. A. Atwater, "Design considerations for plasmonic photovoltaics," *Adv. Mater.*, vol. 22, no. 43, pp. 4794–4808, 2010, doi: 10.1002/adma.201000488.

[172] R. A. Pala, J. White, E. Barnard, J. Liu, and M. L. Brongersma, "Design of plasmonic thin-film solar cells with broadband absorption enhancements," *Adv. Mater.*, vol. 21, no. 34, pp. 3504–3509, 2009, doi: 10.1002/adma.200900331.

[173] S. K. Kim *et al.*, "Tuning light absorption in core/shell silicon nanowire photovoltaic

devices through morphological design," *Nano Lett.*, vol. 12, no. 9, pp. 4971–4976, 2012, doi: 10.1021/nl302578z.

[174] S. Taylor, Y. Yang, and L. Wang, "Vanadium dioxide based Fabry-Perot emitter for dynamic radiative cooling applications," *J. Quant. Spectrosc. Radiat. Transf.*, vol. 197, pp. 76–83, 2017, doi: 10.1016/j.jqsrt.2017.01.014.

[175] Z. Qi *et al.*, "Au nanoparticle-decorated silicon pyramids for plasmon-enhanced hot electron near-infrared photodetection," *Nanotechnology*, vol. 28, no. 27, 2017, doi: 10.1088/1361-6528/aa74a3.

[176] C. P. Saini, A. Barman, M. Kumar, B. Satpati, T. Som, and A. Kanjilal, "Self-decorated Au nanoparticles on antireflective Si pyramids with improved hydrophobicity," *J. Appl. Phys.*, vol. 119, no. 13, 2016, doi: 10.1063/1.4945379.

[177] C. P. Saini, A. Barman, M. Kumar, P. K. Sahoo, T. Som, and A. Kanjilal, "Improved broadband antireflection in Schottky-like junction of conformal Al-doped ZnO layer on chemically textured Si surfaces," *Appl. Phys. Lett.*, vol. 105, no. 12, 2014, doi: 10.1063/1.4896340.

[178] J. Y. Jung *et al.*, "Infrared broadband metasurface absorber for reducing the thermal mass of a microbolometer," *Sci. Rep.*, vol. 7, no. 1, pp. 1–8, 2017, doi: 10.1038/s41598-017-00586-x.

[179] Z. Huang, N. Geyer, P. Werner, J. De Boor, and U. Gösele, "Metal-assisted chemical etching of silicon: A review," *Adv. Mater.*, vol. 23, no. 2, pp. 285–308, Jan. 2011, doi: 10.1002/ADMA.201001784.

[180] L. Ferrer-Argemi, Z. Yu, J. Kim, N. V. Myung, J. H. Lim, and J. Lee, "Silver content dependent thermal conductivity and thermoelectric properties of electrodeposited antimony telluride thin films," *Sci. Rep.*, vol. 9, no. 1, pp. 1–8, 2019, doi: 10.1038/s41598-019-45697-9.

[181] Z. Yu, L. Ferrer-Argemi, J. Kim, J. H. Lim, N. V. Myung, and J. Lee, "Phase-dependent thermal conductivity of electrodeposited antimony telluride films," *J. Mater. Chem. C*, vol. 6, no. 13, pp. 3410–3416, 2018, doi: 10.1039/c8tc00140e.

[182] K. E. Bean, "Anisotropic etching of silicon," *IEEE Trans. Electron Devices*, vol. 25, no. 10, pp. 1185–1193, Oct. 1978, doi: 10.1109/T-ED.1978.19250.

[183] J. R. Howell, M. P. Menguc, and R. Siegel, *Thermal Radiation Heat Transfer*. CRC Press, 2015.

[184] R. Y. M. Wong, C. Y. Tso, C. Y. H. Chao, B. Huang, and M. P. Wan, "Ultra-broadband asymmetric transmission metallic gratings for subtropical passive daytime radiative cooling," *Sol. Energy Mater. Sol. Cells*, vol. 186, no. February, pp. 330–339, 2018, doi: 10.1016/j.solmat.2018.07.002.

[185] N. Ikarashi and K. Masuzaki, "Silicide formation process in ultra-thin Ni-silicide film for advanced semiconductor devices: Mechanism of NiSi2 formation at low temperature," *J. Phys. Conf. Ser.*, vol. 326, no. 1, 2011, doi: 10.1088/1742-

6596/326/1/012051.

[186] Y. Jin *et al.*, “Broadband omnidirectional perfect absorber based on carbon nanotube films,” *Carbon N. Y.*, vol. 161, pp. 510–516, 2020, doi: 10.1016/j.carbon.2020.01.106.

[187] T. Søndergaard *et al.*, “Plasmonic black gold by adiabatic nanofocusing and absorption of light in ultra-sharp convex grooves,” *Nat. Commun.*, vol. 3, pp. 1–6, 2012, doi: 10.1038/ncomms1976.

[188] J. Jiang, M. Chen, and J. A. Fan, “Deep neural networks for the evaluation and design of photonic devices,” *Nat. Rev. Mater.*, vol. 6, no. 8, pp. 679–700, 2021, doi: 10.1038/s41578-020-00260-1.

[189] J. Jiang and J. A. Fan, “Simulator-based training of generative neural networks for the inverse design of metasurfaces,” *Nanophotonics*, vol. 9, no. 5, pp. 1059–1069, 2019, doi: 10.1515/nanoph-2019-0330.

[190] M. Mehrpouya and H. C. Bidsorkhi, “MEMS Applications of NiTi Based Shape Memory Alloys: A Review,” *Micro Nanosyst.*, vol. 8, no. 2, pp. 79–91, 2017, doi: 10.2174/1876402908666161102151453.

[191] J. Gu *et al.*, “ VO 2 -Based Infrared Radiation Regulator with Excellent Dynamic Thermal Management Performance ,” *ACS Appl. Mater. Interfaces*, 2022, doi: 10.1021/acsami.1c17914.

[192] A. Taylor, I. Parkin, N. Noor, C. Tummeltshammer, M. S. Brown, and I. Papakonstantinou, “A bioinspired solution for spectrally selective thermochromic VO_2 coated intelligent glazing,” *Opt. Express*, vol. 21, no. S5, p. A750, Sep. 2013, doi: 10.1364/OE.21.00A750.

[193] A. Krishnan, A. B. O’Gorman, and M. L. Povinelli, “Design of switchable, narrowband thermal absorption peaks in metal-vanadium-dioxide gratings,” *J. Opt. (United Kingdom)*, vol. 22, no. 9, 2020, doi: 10.1088/2040-8986/aba812.

[194] L. Peng *et al.*, “Smart Thermal Management Textiles with Anisotropic and Thermoresponsive Electrical Conductivity,” *Adv. Mater. Technol.*, vol. 5, no. 1, pp. 1–9, 2020, doi: 10.1002/admt.201900599.

[195] Y. Jia, X. Wang, H. Yin, H. Yao, J. Wang, and C. Fan, “Highly tunable thermal emitter with vanadium dioxide metamaterials for radiative cooling,” *Appl. Opt.*, vol. 60, no. 19, p. 5699, 2021, doi: 10.1364/ao.421977.

[196] M. E. Uslu, I. B. Misirlioglu, and K. Sendur, “ Selective IR response of highly textured phase change VO 2 nanostructures obtained via oxidation of electron beam deposited metallic V films ,” *Opt. Mater. Express*, vol. 8, no. 8, p. 2035, 2018, doi: 10.1364/ome.8.002035.

[197] T. H. Yang, R. Aggarwal, A. Gupta, H. Zhou, R. J. Narayan, and J. Narayan, “Semiconductor-metal transition characteristics of VO2 thin films grown on c-and r-sapphire substrates,” *J. Appl. Phys.*, vol. 107, no. 5, 2010, doi: 10.1063/1.3327241.

[198] Y. Muraoka, Y. Ueda, and Z. Hiroi, "Large modification of the metal-insulator transition temperature in strained VO2 films grown on TiO2 substrates," *J. Phys. Chem. Solids*, vol. 63, no. 6–8, pp. 965–967, 2002, doi: 10.1016/S0022-3697(02)00098-7.

[199] K. Nagashima, T. Yanagida, H. Tanaka, and T. Kawai, "Stress relaxation effect on transport properties of strained vanadium dioxide epitaxial thin films," *Phys. Rev. B - Condens. Matter Mater. Phys.*, vol. 74, no. 17, pp. 13–16, 2006, doi: 10.1103/PhysRevB.74.172106.

[200] M. Ono, K. Chen, W. Li, and S. Fan, "Self-adaptive radiative cooling based on phase change materials," *Opt. Express*, vol. 26, no. 18, p. A777, 2018, doi: 10.1364/oe.26.00a777.

[201] T. Li *et al.*, "A radiative cooling structural material," *Science*, vol. 364, no. 6442, pp. 760–763, 2019, doi: 10.1126/science.aau9101.

[202] X. Li *et al.*, "Integration of daytime radiative cooling and solar heating for year-round energy saving in buildings," *Nat. Commun.*, vol. 11, no. 1, pp. 1–9, 2020, doi: 10.1038/s41467-020-19790-x.

[203] R. C. Youngquist, M. A. Nurge, W. L. Johnson, T. L. Gibson, and J. M. Surma, "Cryogenic deep space thermal control coating," *J. Spacecr. Rockets*, vol. 55, no. 3, pp. 622–631, 2018, doi: 10.2514/1.A34019.

[204] K. N. Marshall and R. A. Breuch, "Optical solar reflector: A highly stable, low αs∈spacecraft thermal control surface," *J. Spacecr. Rockets*, vol. 5, no. 9, pp. 1051–1056, 1968, doi: 10.2514/3.29420.

[205] B. Slovick, Z. G. Yu, M. Berding, and S. Krishnamurthy, "Perfect dielectric-metamaterial reflector," *Phys. Rev. B - Condens. Matter Mater. Phys.*, vol. 88, no. 16, pp. 1–7, 2013, doi: 10.1103/PhysRevB.88.165116.

[206] P. Moitra *et al.*, "Large-Scale All-Dielectric Metamaterial Perfect Reflectors," *ACS Photonics*, vol. 2, no. 6, pp. 692–698, 2015, doi: 10.1021/acsphotonics.5b00148.

[207] P. Moitra, B. A. Slovick, Z. Gang Yu, S. Krishnamurthy, and J. Valentine, "Experimental demonstration of a broadband all-dielectric metamaterial perfect reflector," *Appl. Phys. Lett.*, vol. 104, no. 17, 2014, doi: 10.1063/1.4873521.

[208] J. long Kou, Z. Jurado, Z. Chen, S. Fan, and A. J. Minnich, "Daytime Radiative Cooling Using Near-Black Infrared Emitters," *ACS Photonics*, vol. 4, no. 3, pp. 626–630, 2017, doi: 10.1021/acsphotonics.6b00991.

[209] M. Santamouris and J. Feng, "Recent progress in daytime radiative cooling: Is it the air conditioner of the future?," *Buildings*, vol. 8, no. 12, 2018, doi: 10.3390/buildings8120168.

[210] J. D. Alden *et al.*, "Radiative cooling by silicone-based coating with randomly distributed microbubble inclusions," *J. Photonics Energy*, vol. 9, no. 03, p. 1, 2019, doi: 10.1117/1.jpe.9.032705.

[211] L. A. Falkovsky, “Optical properties of graphene,” *J. Phys. Conf. Ser.*, vol. 129, no. 3, pp. 2–6, 2008, doi: 10.1088/1742-6596/129/1/012004.

[212] H. H. Moore, “Refractive index of alkaline earth halides and its wavelength and temperature derivatives,” *J. Phys. Chem. Ref. Data*, vol. 9, no. 1, pp. 161–290, 1982, doi: 10.1063/1.555616.

[213] T. Siefke *et al.*, “Materials Pushing the Application Limits of Wire Grid Polarizers further into the Deep Ultraviolet Spectral Range,” *Adv. Opt. Mater.*, vol. 4, no. 11, pp. 1780–1786, 2016, doi: 10.1002/adom.201600250.

[214] C. A. Gueymard, D. Myers, and K. Emery, “Proposed reference irradiance spectra for solar energy systems testing,” *Sol. Energy*, vol. 73, no. 6, pp. 443–467, 2002, doi: 10.1016/S0038-092X(03)00005-7.